Operation of Holographic Elements with Broadband Light Sources

Thesis by

Hung-Te Hsieh

In Partial Fulfillment of the Requirements

for the Degree of

Doctor of Philosophy

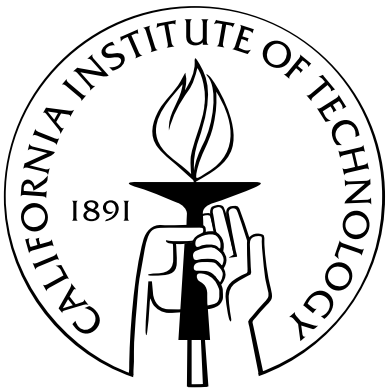

California Institute of Technology

Pasadena, California

2005

(Defended February 11, 2005)

Material in chaper 4 is reprinted with permission from H. T. Hsieh, G. Panotopoulos, M. Liger, Y. C. Tai and D. Psaltis, "Athermal holographic filters." IEEE publication: Photonics Technology Letters, **16**(1), January 2004, pp. 177-179 ©2004 IEEE.

Acknowledgements

I would like to start by expressing tremendous gratitude for Professor Demetri Psaltis, my academic advisor during the five years I spent at Caltech. His unwavering enthusiasm for science and the remarkable professionalism he demonstrated deeply inspired me. I am greatly indebted to the wonderful chance he granted me to come to Caltech and work on exciting projects with several extraordinarily brilliant students. I would also like to thank Professor Karsten Buse dearly. I enjoyed working productively in his marvelous laboratories. I was also impressed by his fruitful devotion not only to science but also to his group as a caring big brother. The eight months I spent in his group at the University of Bonn are very special in my life. Wonderful memories abound: hiking through the snowy Goethe's trail in Brocken, strolling around in the Christmas market in wide-eyed curiosity, cycling along the Rhein river... etc.

One precious privilege of studying at Caltech is the pleasure of getting to know some of the brightest souls in the world. I am glad I have the chance to show my appreciation here. Wenhai Liu, who took me to my first dinner in America. Greg Steckman, Chris Moser, Greg Bollock. Zhiwen Liu, my intellectual idol, who warmly shared his brilliant physical insights and made them feel like a breeze! George Panotopoulos, my best mentor, who taught me almost everything I know working in an optics lab and then a lot more about life. I had the best time working with him on the holographic filter project. José Mumbrú, my Star Wars hero, who is blessed with such a sense of humor you need to invent a new word for humorous. The tapas in Barcelona and paella in Alicante I had with him are among the most enjoyable meals I remember. Yunping Yang, who was always generous with his valuable advice. Irena Maravic, for some most enlightening conversations. Martín and his most lovely wife Lucía, who offer me the warmest friendship and the fantastic chance to experience first-hand the way Spaniards wed and party! Emmanouil-Panagiotis Fitrakis, thanks to whom my strenuous first year and the following intensive lab work did not turn my life anemic in fun. Todd Meyrath; Zhenyu Li, whose kind heart and sense of responsibility will definitely get him far. Hua Long, George Maltezos, Vijay Gupta and Dirk Walther. Dr. Ye Pu, for his help with my femtosecond experiments. Dr. David Erickson, who impressed me with his dedication to work. I also admire the tenacity and exceptional capability of the "new generation": James Adleman, Eric Ostby, Troy Rockwood and Mankei Tsang. And Baiyang Li, for the eye-opening and life-changing

conversations on cross-strait relationship.

I want to thank Yayun Liu for meeting some of my most uncanny needs in experiments and the gift of useful advice to a 24-year-old who was going through culture shock. Lucinda Acosta, for her competence in administrative affairs and most importantly, the passion we share for some of the most life-enriching music and of course, Julienne. Linda Dozsa, for hailing me as a great photographer and the best Champagne I ever drank! Teresita Legaspi, for her kind help in the Registrar's Office. My special thanks also go to Divina Bautista and Alice Sogomonian in the Health Center, who took the best care of me after my horrible car accident.

Across the Atlantic Ocean, I have to deliver my most sincere appreciation to all the members of Dr. Buse's group for their soothing friendship during my sojourn. Especially to Oliver Beyer, for the excellent collaboration we had in the femtosecond holography project and for welcoming me into his great family in Osnabrück. Dr. Konrad Peithmann, who remains my favorite office mate. Clemens von Korff Schmising and Dominik Maxein, for their indispensable help in the lab and some crash courses in German. Dr. Boris Sturman, for his mathematical genius and valuable suggestions. Ms. Raja Bernard, for preventing me from becoming an illegal immigrant in Germany. Mark Wengler, Ulrich Hartwig and Helge Eggert, who took me out to a live jazz bar for a most memorable adventure. Ingo Breunig, for the enjoyable barbecue party. Michael Kösters, for helping me with the apartment and the successful collaboration. Drs. Elisabeth Soergel and Akos Hoffmann, for the delicious Mexican-style dinner and a fun-filled night. Last but not least, I send my special thanks to Ms. Elli Luhmer, my landlord, whose motherly care kept me warm at heart even on those snowy days in Bonn.

My days as a graduate student would have been so lonely without my dearest friends, both in Taiwan and America. Special thanks go to William Chang and Bartz Huang, who have always been there for me through the years. Eric Cheng, with whom I enjoy exchanging banter. And of course all the TGSA members at Caltech. Todd, who rescued me from the wrecked car. I would also like to thank Russ for the incredible tolerance of my worst side and for being a constant in my life.

Finally, I would like to dedicate my thesis to my family, especially to my parents, whose immeasurable and unconditional love and support make me want to be a more generous and better person. Words cannot describe how much I love them.

Abstract

This thesis presents the theoretical and experimental investigation of volume holography operated with broadband/polychromatic light sources, i.e., in both continuous-wave (linear) and femtosecond-pulse (nonlinear) regimes.

The first chapter reviews the concept of volume holography and provides a tacit introduction to some basic properties of volume holograms and compares the operation of holograms in the spatial and temporal domains, preparing the readers for later chapters.

The second chapter introduces a powerful theoretical tool for the analysis of volume holograms in the reflection geometry: the matrix formulation, laying the foundation for the application of holographic gratings utilized as WDM filters.

The third chapter takes into consideration the effects of the practically inevitable finite beam-widths. By means of Fourier decomposition, the deviation of the filtering properties of volume holographic gratings from the ideal plane-wave case can be satisfactorily explained and predicted. Experiments and simulations are performed and compared to confirm the validity of the theory.

Volume holographic gratings in the reflection geometry serve as excellent WDM filters for telecommunication purposes thanks to their low cross-talk and readily engineered filtering properties. The theoretical design and experimental realization of athermal holographic filters are presented in the fourth chapter. By incorporating a passive, thermally actuated MEMS mirror, the temperature dependence of the Bragg wavelength of a holographic filter can be compensated.

The analysis of holographic gratings in the 90 degree geometry requires a two dimensional theory. The relevant boundary conditions give rise to some peculiar behaviors in this configuration. Theory, simulations and some experimental results of the 90-degree holography are presented in chapter five.

The sixth chapter delves into the subject of instantaneous Kerr index grating established by two intense, interfering femtosecond (pump) pulses at 388 nm owing to the omnipresent third-order nonlinearity. The coupled-mode equations describing the incident and diffracted (probe) pulses at 776 nm are written down; the solution is experimentally corroborated. It is further demonstrated that the temporal resolution in such a holographic pump-probe configuration does not degrade appreciably as the angular separation between pump pulses increases.

Chapter seven investigates the nonlinear absorption processes in lithium niobate crystals with

femtosecond pulses. The model of two-photon absorption well explains and anticipates the transmission coefficients of single pulses over a wide range of intensity. Collinear pump-probe transmission experiments are then carried out to look into the nonlinear absorption suffered by the probe pulse at 776 nm owing to the pump pulse at 388 nm; the dependence of the probe pulse transmission coefficient on the time delay between pump and probe pulses is characterized by a dip and a long-lasting plateau, which are attributed, respectively, to direct two-photon transitions involving pump and probe photons and the existence of free carriers.

Building on the experimental experience and theoretical understanding of the previous two chapters, the results of holographic pump-probe experiments in lithium niobate crystals are presented in the final chapter. The behavior is much more complicated because it encompasses all phenomena explored in the two preceding chapters, i.e., both the real and imaginary parts of the third-order susceptibility come into play in the instantaneous material response; furthermore, another mixed grating due to excited charge carriers exists long after the pump pulses pass through. Valuable information on the grating formation process is obtained thanks to the sub-picosecond temporal resolution of such configurations.

Contents

List of Figures

Chapter 1

Introduction

In this thesis we investigate the operation of holographic gratings with broadband light sources. We begin this chapter by introducing some of the important definitions and properties of volume holographic gratings (VHGs) and then review several interesting properties and applications of volume holograms in the context of spatial and temporal domains, which are the manifestations of the selectivity inherent in volume holograms.

For the rest of the thesis, we will devote our attention to the investigation of temporal and spectral properties of volume holograms by means of polychromatic operations.

1.1 Volume holographic gratings and their filtering properties

A volume holographic grating consists of a modulated refractive index pattern imprinted inside a bulk recording material (e.g., photorefractive crystals[1], photosensitive polymers[2]). Without loss of generality, such a grating can be represented as

$$n(\mathbf{r}) = n + \Delta n \cos \mathbf{K} \cdot \mathbf{r}, \tag{1.1}$$

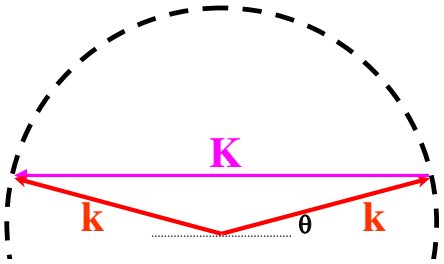

Figure 1.1: A schematic illustration of the Bragg condition: the wavevectors of the optical fields and the grating vector **K** constitute the sides of a triangle.

where n is the average refractive index of the material and $\mathbf{K}$ is the grating vector and is related to the grating period Λ by $|\mathbf{K}| = K = 2\pi/\Lambda$. Once recorded, the grating can act as an efficient coupler between plane waves. The coupling property is largely specified by two important parameters. The first is the grating period Λ, which determines the Bragg condition and therefore the appropriate interacting optical wavelength λ. As shown in Fig. 1.1, if the wavevectors of two optical fields and the grating vector K constitute the sides of a triangle, the optical fields can be coupled through the holographic grating when the conservation of momentum and energy is satisfied. The relevant Bragg condition in this case is

$$\lambda = 2n\Lambda \cos\theta, \tag{1.2}$$

where θ is the angle of incidence. Plane wave components that meet the Bragg condition will be diffracted by the grating and those that do not will be transmitted instead. Therefore the holographic grating can act as a filter, discriminating between various plane wave components based on the Bragg condition.

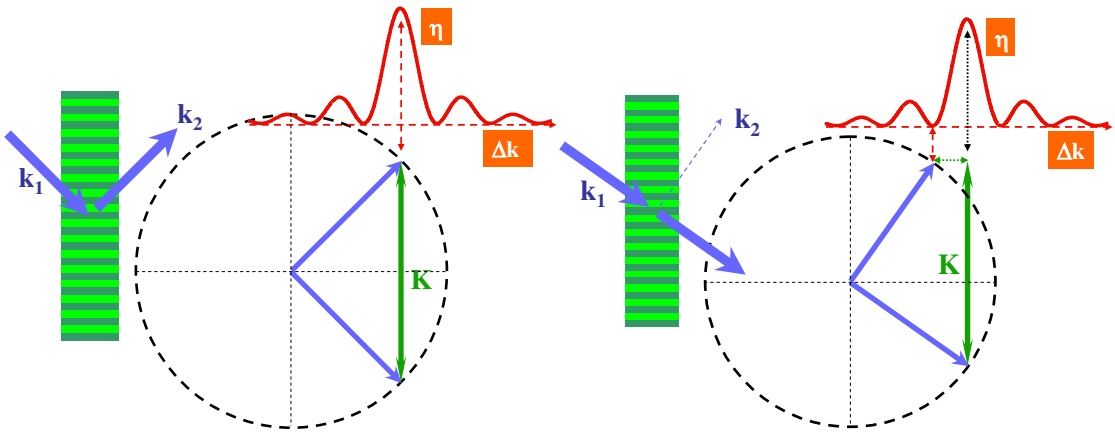

(a) Bragg-matched case. (b) Bragg-mismatch case

Figure 1.2: Angular selectivity of a volume hologram.

1.2 Spatial-domain perspective

The angular selectivity of volume holograms is responsible for their various applications in the spatial domain. The principle can be explained with the help of Fig. 1.2. In Fig. 1.2(a) we show the Bragg-matched case where the conservation of momentum is satisfied and most of the incident light (with wavevector $\mathbf{k_1}$) is coupled into the diffracted light (with wavevector $\mathbf{k_2}$). Also shown is the k-diagram of this particular configuration and the selectivity curve of the grating, which represents

the diffraction efficiency η of the VHG as a function of the phase mismatch $\mathbf{\Delta k}$ defined as

$$\mathbf{\Delta k} = \mathbf{k_2} - \mathbf{k_1} - \mathbf{K}. \tag{1.3}$$

In the Bragg-matched case, $\mathbf{\Delta k} = 0$ and we achieve maximum, in this case 100%, energy coupling.

If now we change the incident angle, as shown in Fig. 1.2(b), a corresponding change (tilting) of $\mathbf{k_2}$ comes about as a result, giving rise to a nonzero phase mismatch denoted by the horizontal double-headed arrow. The diffraction efficiency will therefore decrease; in this case η happens to be 0, and no beam coupling will be observed. In general, the longer the interaction length between the grating and the light field is, the more selective the VHG will be.

Various spatial-domain properties and applications of holograms are attributed to their angular selectivity; for instance, angle multiplexing[3], shift multiplexing[4], holographic storage[5], image processing[6] and pattern recognition, to name just a few.

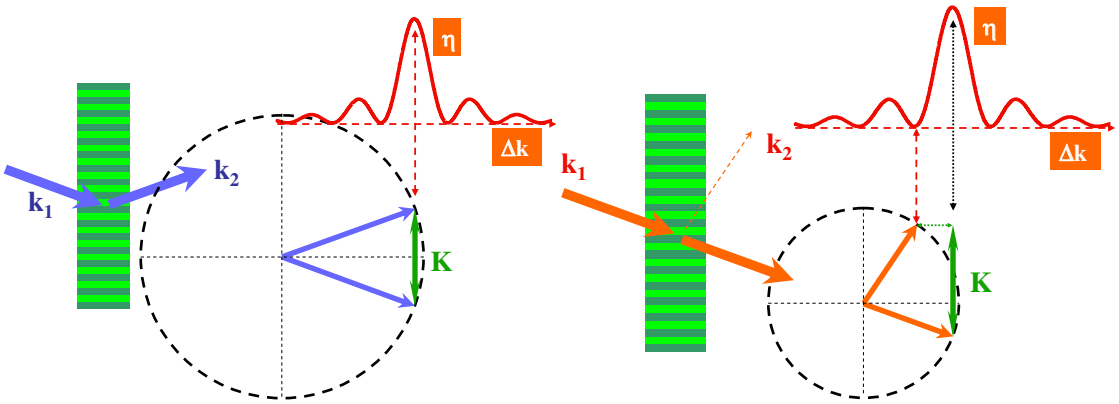

(a) Bragg-matched case. (b) Bragg-mismatch case

Figure 1.3: Wavelength selectivity of a volume hologram.

1.3 Temporal-domain perspective

On the other hand, the volume holograms' wavelength selectivity is responsible for their temporal/spectral properties. Refer to Fig. 1.3(a) for the Bragg-matched case where 100% of the incident light (with wavevector $\mathbf{k_1}$) is coupled into the diffracted light (with wavevector $\mathbf{k_2}$). The k-diagram in this case is similar to the one in Fig. 1.2(a).

If instead of changing the incident angle, we change the wavelength of the incident field, as shown in Fig. 1.3(b), another corresponding phase mismatch transpires, and we end up with diminished diffraction efficiency again as implied by the k-diagram. Here the k-diagram is constructed with a smaller value of $|\mathbf{k_1}|$, signifying a bigger incident wavelength.

In turn, the temporal-domain properties and applications of holograms are direct results of

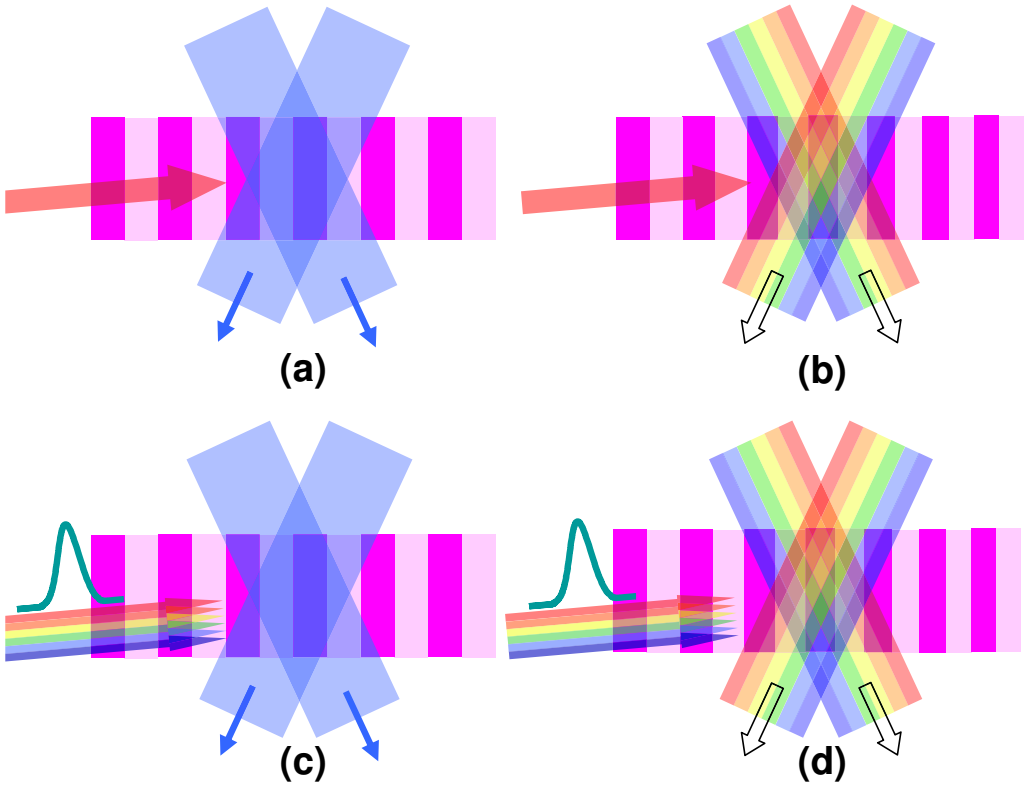

Figure 1.4: Schematic illustrations of the recording and readout of holograms with monochromatic and polychromatic light sources.

the wavelength selectivity; examples include wavelength multiplexing[7], nondestructive readout, 1D photonic bandgap[8], WDM filtering[9], dispersion management[10] and VHGs' applications in spectroscopy.

Comparison between Fig. 1.2 and Fig. 1.3 reveals that the two perspectives of the operation of holograms are closely related through the parameter $\mathbf{\Delta k}$, which is a function of both incident angles and light wavelengths.

1.4 Recording and readout of holographic gratings with polychromatic light sources

Fig. 1.4 encompasses four possible recording and readout configurations of holography with monochromatic and polychromatic light sources. In our context, monochromatic light sources are usually continuous-wave (cw) lasers and polychromatic light sources can be either tunable cw lasers or pulse lasers.

In this thesis, we investigate the more general cases (c) and (d) in Fig. 1.4. The second chapter

introduces the matrix formulation for the analysis of VHGs in the reflection geometry, which will be used in the next three chapters. Chapters 3, 4 and 5 are then devoted to the case (c) where a uniform holographic grating is recorded by two interfering monochromatic fields and then read out with a continuously tunable laser source. Photosensitive glass and lithium niobate ($LiNbO_3$) will be our materials of choice.

In the last three chapters we will concern ourselves with case (d), where gratings are recorded and read out by femtosecond pulse sources; we will discuss several observed nonlinear phenomena in the regime of femtosecond holography. Experiments are conducted in calcium fluoride (CaF_2) and lithium niobate samples.

Bibliography

[1] G. C. Valley, M. B. Klein, R. A. Mullen, D. Rytz, and B. Wechsler. Photorefractive materials. *Annual Review of Materials Science*, 18:165–188, 1988.

[2] J. E. Ludman, J. R. Riccobono, N. O. Reinhand, I. V. Semenova, Y. L. Korzinin, S. M. Shahriar, H. J. Caulfield, J. M. Fournier, and P. Hemmer. Very thick holographic nonspatial filtering of laser beams. *Optical Engineering*, 36(6):1700–1705, June 1997.

[3] F. H. Mok. Angle-multiplexed storage of 5000 holograms in lithium niobate. *Optics Letters*, 18(11):915–917, June 1993.

[4] D. Psaltis, M. Levene, A. Pu, and G. Barbastathis. Holographic storage using shift multiplexing. *Optics Letters*, 20(7):782–784, April 1995.

[5] D. Psaltis and F. Mok. Holographic memories. *Scientific America*, 273:70–76, November 1995.

[6] W. Liu, G. Barbastathis, and D. Psaltis. Volume holographic hyperspectral imaging. *Applied Optics*, 43(18):3581–3599, June 2004.

[7] G. A. Rakuljic, V. Leyva, and A. Yariv. Optical data storage by using orthogonal wavelength-multiplexed volume holograms. *Optics Letters*, 17(20):1471–1473, October 1992.

[8] J. D. Joannopoulos, P. R. Villenueve, and S. Fan. Photonic crystals: putting a new twist on light. *Nature*, 386:143–149, March 1997.

[9] G. A. Rakuljic and V. Leyva. Volume holographic narrow-band optical filter. *Optics Letters*, 18:459–461, March 1993.

[10] K. O. Hill and G. Meltz. Fiber bragg grating technology fundamentals and overview. *Journal of Lightwave Technology*, 15(8):1263–1276, August 1997.

Chapter 2

Matrix formulation for holographic filters in the reflection geometry

In this chapter, we will introduce a powerful analytical tool, matrix formulation, for volume holograms in the reflection geometry. We will then apply the matrix formulation to the sinusoidal grating structure as illustrated in Fig. 2.1. Sinusoidal index modulation has a fundamental importance because any profile of index modulation can be represented as the linear combination thereof by means of Fourier transform. The ability to analyze such structures will play an important part in the next two chapters.

2.1 Matrix formulation for optical layered media

The well-established coupled mode analysis[1, 2] gives an accurate description of volume holographic gratings in the vicinity of the Bragg condition and is highly useful for the characterization of one dimensional photonic bandgap; however, it is not applicable away from Bragg condition; moreover, it can not deal with the cases of chirped gratings due to an implicit assumption in the analysis that only a number of propagating modes are strongly coupled by the grating structure. A more flexible method will be investigated here.

Before dealing with the sinusoidal grating structure, we first consider the more straightforward

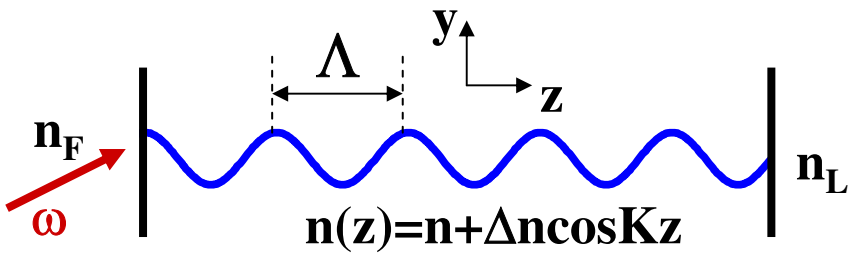

Figure 2.1: A sinusoidal grating structure.

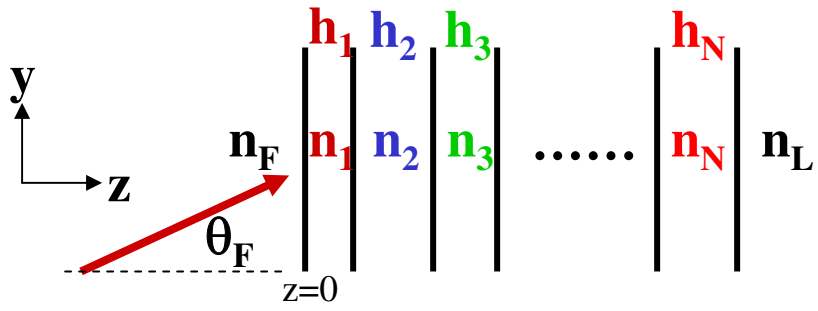

Figure 2.2: A stratified dielectric structure. The layers are homogeneous in the x and y dimensions. The layer i has a thickness h_i with a refractive index n_i, where $i = F, 1, 2 \cdots N, L$.

case of optical layered media. By optical layered media, we refer to stratified dielectric structures similar to the one depicted in Fig. 2.2 where homogeneity is assumed in each layer. We would like to know the frequency response of this structure; more specifically, we want to calculate the reflection and transmission coefficients of a plane wave of this structure as a function of its propagation direction specified by its incident angle θ_F and frequency ω.

We first consider the simplest case, i.e., a single-layer structure with index n_1 sandwiched between infinite space with indices n_F and n_L. Without loss of generality, we assume that the plane of incidence (the plane containing the incident ray and the normal to the boundary) is the yz plane; z is the direction of stratification of the optical layer(s). We need to consider separately the TE case (whose electric field has only an x component) and the TM case (whose magnetic field has only an x component) for a specific monochromatic wave with angular frequency. Boundary conditions dictate that across the interfaces (specified by $z = h_i$), the tangential components of the electric and magnetic fields (E_x, E_y, H_x, H_y) must be continuous. We also know from the source-free Maxwell's equations that

$$\begin{aligned} \mathbf{H} &= \frac{j}{\omega\mu}\nabla \times \mathbf{E}, \\ \mathbf{E} &= \frac{-j}{\omega\varepsilon}\nabla \times \mathbf{H}. \end{aligned} \tag{2.1}$$

2.1.1 TE case

We can write down the electric fields in all three layers for the TE case:

$$E_x(y,z) = \begin{cases} A_F \exp\left[-j(\beta_F y + \gamma_F z)\right] + B_F \exp\left[-j(\beta_F y - \gamma_F z)\right] & : \quad z \le 0 \\ A_1' \exp\left[-j(\beta_1 y + \gamma_1 z)\right] + B_1' \exp\left[-j(\beta_1 y - \gamma_1 z)\right] & : \quad 0 \le z \le h_1 \\ A_L' \exp\left\{-j[\beta_L y + \gamma_L (z - h_1)]\right\} + B_L' \exp\left\{-j[\beta_L y - \gamma_L (z - h_1)]\right\} & : \quad z \ge h_1 \end{cases}$$

where $\beta_i^2 + \gamma_i^2 = \omega^2 n_i^2/c^2 = k_i^2 = (2\pi n_i/\lambda_0)^2$, and $i = F, 1, L$. $A_i(B_i)$ represents the amplitude of forward(backward)-traveling wave referred to the right-side boundary of layer i, while $A_i'(B_i')$ represents the amplitude of forward(backward)-traveling wave referred to the left-side boundary of layer i. We then apply Eq. (2.1) to get the tangential component of the magnetic fields:

$$H_y(y,z) = \begin{cases} \frac{\gamma_F}{\omega\mu}\left\{A_F \exp\left[-j(\beta_F y + \gamma_F z)\right] - B_F \exp\left[-j(\beta_F y - \gamma_F z)\right]\right\} & : \quad z \le 0 \\ \frac{\gamma_1}{\omega\mu}\left\{A_1' \exp\left[-j(\beta_1 y + \gamma_1 z)\right] - B_1' \exp\left[-j(\beta_1 y - \gamma_1 z)\right]\right\} & : \quad 0 \le z \le h_1 \\ \frac{\gamma_L}{\omega\mu}\left\{A_L' \exp\left\{-j[\beta_L y + \gamma_L (z-h_1)]\right\} - B_L' \exp\left\{-j[\beta_L y - \gamma_L (z-h_1)]\right\}\right\} & : \quad z \ge h_1 \end{cases}$$

To apply the boundary conditions at interfaces $z = 0$ and $z = h_1$, it is required that the phase terms must be equal for all points on the interfaces, i.e., for all y:

$$\begin{cases} \exp(-j\beta_F y) &= \exp(-j\beta_1 y), \\ \exp(-j\beta_1 y) &= \exp(-j\beta_L y). \end{cases}$$

We then have $\beta_F = \beta_1 = \beta_L$ and therefore $n_F \sin\theta_F = n_1 \sin\theta_1 = n_L \sin\theta_L$, which is the famous Snell's Law. More intuitively, since the whole structure is homogeneous along the y direction, there cannot be a momentum change in the y direction for the photons. Application of the continuity of E_x and H_y across the first interface $z = 0$ gives us

$$\begin{cases} A_F + B_F &= A_1' + A_2', \\ \sqrt{\frac{\varepsilon_F}{\mu}}(A_F - B_F)\cos\theta_F &= \sqrt{\frac{\varepsilon_1}{\mu}}(A_1' - B_1')\cos\theta_1, \end{cases}$$

or in the matrix form

$$\begin{bmatrix} 1 & 1 \\ n_F\cos\theta_F & -n_F\cos\theta_F \end{bmatrix} \begin{bmatrix} A_F \\ B_F \end{bmatrix} = \begin{bmatrix} 1 & 1 \\ n_1\cos\theta_1 & -n_1\cos\theta_1 \end{bmatrix} \begin{bmatrix} A_1' \\ B_1' \end{bmatrix},$$

where we have used $\varepsilon_i = n_i^2 \varepsilon_0$. In shorthand, it becomes

$$\mathcal{D}_{F,TE}\mathcal{A}_F = \mathcal{D}_{1,TE}\mathcal{A}_1',$$

where $\mathcal{D}_i$ and $\mathcal{A}_i$ are the corresponding 2×2 and 2×1 matrices. The subscript TE or TM is placed for the purpose of distinguishing between TE and TM cases. We now have

$$\mathcal{A}_F = \mathcal{D}_{F,TE}^{-1}\mathcal{D}_{1,TE}\mathcal{A}_1'.$$

Obviously, the same relationship will transpire at the interface $z = h_1$ as well:

$$\mathcal{A}_1 = \mathcal{D}_{1,TE}^{-1}\mathcal{D}_{L,TE}\mathcal{A}'_L.$$

We therefore reach the conclusion that the matrix $\mathcal{D}_{i,TE}^{-1}\mathcal{D}_{i+1,TE}$ takes care of the interface effect between layers i and i+1.

Now let us account for the relationship between $\mathcal{A}'_i$ and $\mathcal{A}_i$. Since

$$A'_1 \exp\left[-j(\beta_1 y + \gamma_1 z)\right] + B'_1 \exp\left[-j(\beta_1 y - \gamma_1 z)\right]$$

and

$$A_1 \exp\left\{-j[\beta_1 y + \gamma_1 (z - h_1)]\right\} + B_1 \exp\left\{-j[\beta_1 y - \gamma_1 (z - h_1)]\right\}$$

are just two expressions of the same electric field in layer i, they must be equal. By equating the two expressions we get

$$\mathcal{A}'_1 = \begin{bmatrix} A'_1 \\ B'_1 \end{bmatrix} = \begin{bmatrix} \exp(j\phi_1) & 0 \\ 0 & \exp(-j\phi_1) \end{bmatrix} \begin{bmatrix} A_1 \\ B_1 \end{bmatrix} = \mathcal{P}_1 \mathcal{A}_1,$$

where $\phi_1 = \gamma_1 h_1 = k_1 \cos\theta_1 h_1$. It is conspicuous that the matrix $\mathcal{P}_i$ takes care of the propagation effect inside layer i with thickness h_i. Now, rather straightforwardly, we may write down

$$\mathcal{A}_F = \mathcal{D}_{F,TE}^{-1}\mathcal{D}_{1,TE}\mathcal{P}_1\mathcal{D}_{1,TE}^{-1}\mathcal{D}_{L,TE}\mathcal{A}'_L = \mathcal{D}_{F,TE}^{-1}\mathcal{M}_{1,TE}\mathcal{D}_{L,TE}\mathcal{A}'_L, \tag{2.2}$$

where

$$\mathcal{M}_{1,TE} = \begin{bmatrix} \cos\phi_1 & \frac{j\sin\phi_1}{n_1\cos\theta_1} \\ jn_1\cos\theta_1\sin\phi_1 & \cos\phi_1 \end{bmatrix}$$

is the layer matrix of dielectric layer 1 for TE wave propagation and, interestingly, $|\mathcal{M}_{1,TE}|$. We point out that all layer matrices are unimodular.

2.1.2 TM case

In the TE case we derive the layer matrices for field components E_x and H_y, while in the TM case we turn to E_y and H_x. Following a procedure similar to that in the TE case, we have

$$\mathcal{D}_{i,TM} = \begin{bmatrix} \cos\theta_i & \cos\theta_i \\ n_i & -n_i \end{bmatrix}$$

and the layer matrix

$$\mathcal{M}_{i,TM} = \begin{bmatrix} \cos\phi_i & \frac{j\cos\theta_i \sin\phi_i}{n_i} \\ \frac{jn_i \sin\phi_i}{\cos\theta_i} & \cos\phi_i \end{bmatrix}$$

for TM waves. Just as in the TE case, $\mathcal{M}_{i,TM}$ is unimodular.

2.1.3 Diffraction efficiency of a multilayer medium

Now that we have accounted for the effects of interfaces and propagation, we are ready to handle the configuration as shown in Fig. 2.2. We can directly write down

$$\mathcal{A}_F = \mathcal{D}_F^{-1}\mathcal{M}_1\mathcal{M}_2\cdots\mathcal{M}_N\mathcal{D}_L\mathcal{A}'_L, \tag{2.3}$$

where $\mathcal{D}_i$ and $\mathcal{M}_i$ are the corresponding interface and layer matrices for TE or TM waves. In either case, Eq. (2.3) can be simplified and recast as

$$\begin{bmatrix} A_F \\ B_F \end{bmatrix} = \mathcal{J}\begin{bmatrix} A'_L \\ B'_L \end{bmatrix} = \begin{bmatrix} J_{11} & J_{12} \\ J_{21} & J_{22} \end{bmatrix}\begin{bmatrix} A'_L \\ B'_L \end{bmatrix}.$$

The reflection coefficient is $r = B_F/A_F = J_{21}/J_{11}$ and the transmission coefficient is $t = A'_L/A_F = 1/J_{11}$, where $B'_L = 0$ has been adopted because the electromagnetic radiation is incident from the left side and there is no backward travelling wave in the rightmost medium. The coefficients r and t are in general complex. The reflectance of such a structure is defined as

$$R = -\frac{\mathbf{S_{FB}}\cdot\mathbf{a_z}}{\mathbf{S_{FA}}\cdot\mathbf{a_z}} = \frac{|B_F|^2}{|A_F|^2} = |r|^2, \tag{2.4}$$

where $\mathbf{S_{FB}}$ ($\mathbf{S_{FA}}$) stands for the Poynting vector of the forward (backward) travelling wave in the leftmost medium. Similarly, the transmittance is defined as

$$T = \frac{\mathbf{S_{LA}}\cdot\mathbf{a_z}}{\mathbf{S_{FA}}\cdot\mathbf{a_z}} = \frac{n_L\cos\theta_L|A'_L|^2}{n_F\cos\theta_F|A_F|^2} = |t|^2\frac{n_L\cos\theta_L}{n_F\cos\theta_F}. \tag{2.5}$$

If the indices of the dielectric layers are all real, there will be no loss and therefore $R + T = 1$.

2.2 Matrix formulation for sinusoidal gratings

Now we can deal with the sinusoidal grating structure as drawn in Fig. 2.1. The trick is to "slice" a single period (length Λ) of the grating into L layers, as illustrated in Fig. 2.3. By approximating each layer as homogeneous with the value of the refractive index at its center, we wind up with the effective transfer matrix of a single period: $\mathcal{C} = \mathcal{M}_1\mathcal{M}_2\cdots\mathcal{M}_L$.

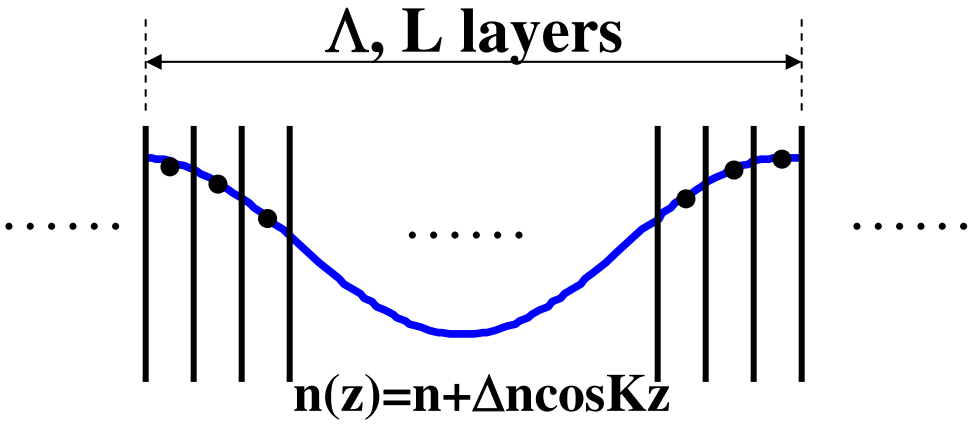

Figure 2.3: The "slicing" of a single period of a sinusoidal grating structure.

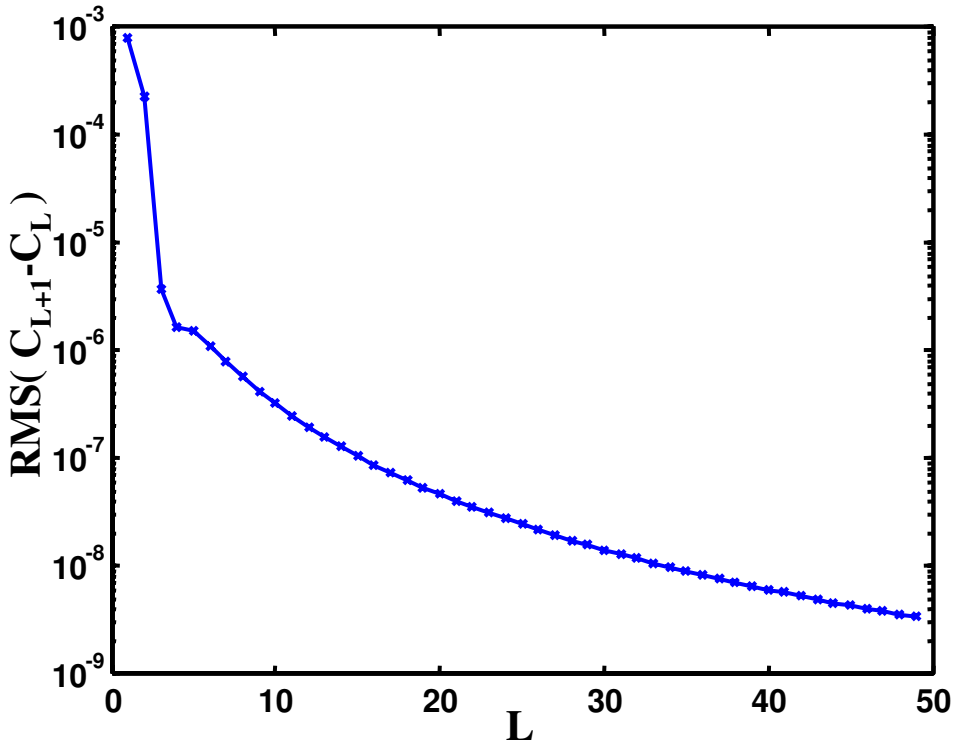

Figure 2.4: Convergence of the effective matrix $\mathcal{C}$ of a single grating period Λ.

It is conceivable that the finer we slice the period, the closer the effective matrix will be to the "real" transfer matrix of a single period. Let's say $\mathcal{C}_L$ is the effective matrix obtained by slicing a single grating period Λ into L layers. Fig. 2.4 shows that as we increase L, the effective matrix $\mathcal{C}_L$ converges. There $RMS(\mathcal{C}_{L+1} - \mathcal{C}_L)$ stands for the root-mean-square value of the four elements of the difference between matrices $\mathcal{C}_{L+1}$ and $\mathcal{C}_L$.

If the grating has N periods in total, we shall get

$$\mathcal{A}_F = \mathcal{D}_F^{-1}\mathcal{C}^N\mathcal{D}_L\mathcal{A}'_L$$

and we may then calculate the reflection and transmission coefficients. This method is computationally favorable because of the fact that the determinant of $\mathcal{C}$ is 1; it greatly facilitates the calculation of the matrix $\mathcal{C}^N$:

$$\mathcal{C} = \begin{bmatrix} C_{11} & C_{12} \\ C_{21} & C_{22} \end{bmatrix} \Leftrightarrow \mathcal{C}^N = \begin{bmatrix} C_{11}U_{N-1}(a) - U_{N-2}(a) & C_{12}U_{N-1}(a) \\ C_{21}U_{N-1}(a) & C_{22}U_{N-1}(a) - U_{N-2}(a) \end{bmatrix}$$

where $a = (C_{11} + C_{22})/2$ and

$$U_N(a) = \frac{1}{\sqrt{1-a^2}} \sin[(N+1)\arccos(a)]$$

is known as the Chebyshev polynomial of the second kind[3].

In Fig. 2.5, we simulate the reflectance, according to Eq. (2.4), of two gratings at normal incidence (therefore TE and TM cases are degenerate). The index modulation is the same for the two gratings ($\Delta n = 4 \times 10^{-4}$), while the medium ($LiNbO_3$ in this case) lengths are 0.5 cm and 2 cm, respectively. The number of slices for a single period is 35.

The bandgap centered at the Bragg wavelength 1550 nm is about 0.14 nm (corresponding to about 17.5 GHz), and it is not affected much by the sample length. This phenomenon can also be explained by the coupled mode analysis: within the bandgap of the filter, $\kappa > |\Delta\beta|$. Since κ is determined by the index modulation, the sample length should not affect the filter bandwidth. In the context of Bloch formalism[4], the range of frequency components that possess complex propagation constants is also determined by the index modulation.

We also observe local maxima and minima outside the bandgap. These "ripples" occur more frequently on the wavelength axis for a longer sample. To explain this, we can think of the grating as a collection of numerous mirrors distributed along the z-axis. If the optical path length inside the sample is an integral multiple of a half wavelength, i.e., $n_1 h_1 = m\lambda/2$ where m is an integer, the reflection from the distributed mirrors will cancel out exactly, and this is the location of a local minima. Simple calculation shows that the difference between optical frequencies of the adjacent

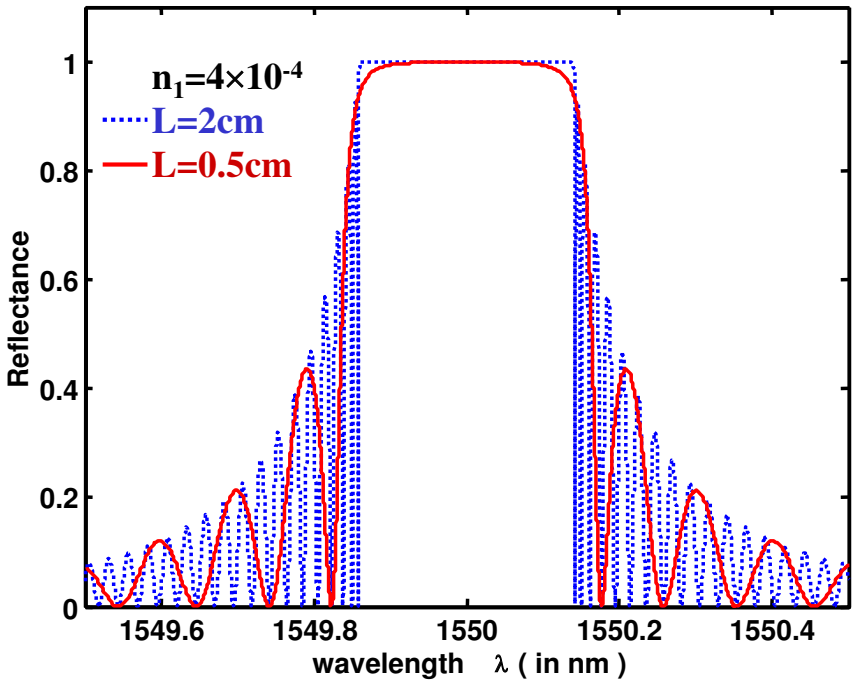

Figure 2.5: Simulated grating reflectance as a function of incident wavelength (wavelength selectivity) for $\Delta n = 4 \times 10^{-4}$. The dotted curve is obtained for a sample length of 2 cm; the solid curve, 0.5 cm.

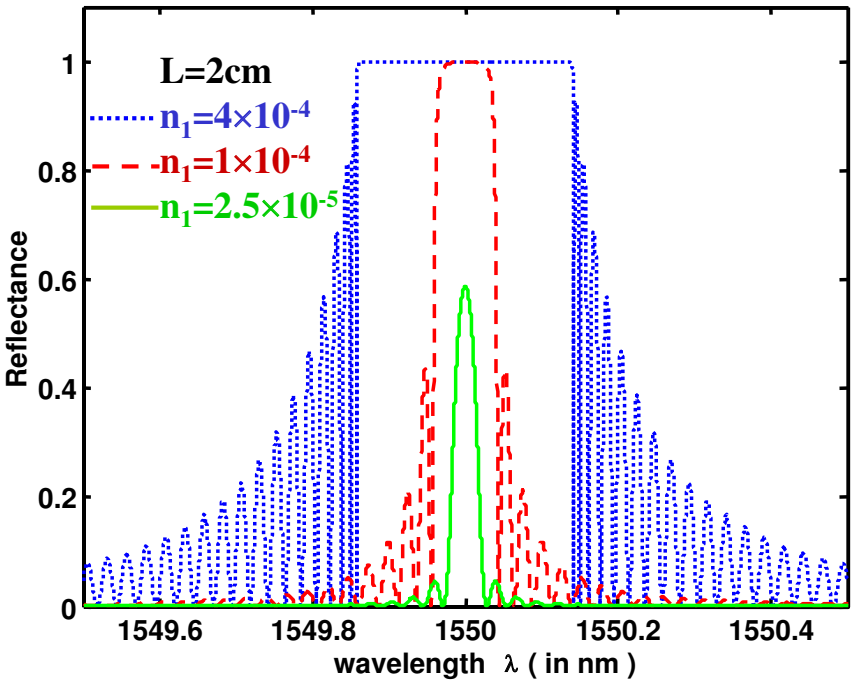

Figure 2.6: Simulated grating reflectance as a function of incident wavelength (wavelength selectivity) for a sample length of 2 cm. The dotted curve is obtained for an index modulation $\Delta n = 4 \times 10^{-4}$; the dashed curve, $\Delta n = 1 \times 10^{-4}$; the solid curve, $\Delta n = 2.5 \times 10^{-5}$.

minima satisfy $\Delta\nu = c/2n_1h_1$. Therefore the longer the crystal is, the more frequent is the ripple oscillation.

In Fig. 2.6, we show simulations for three gratings with different index modualtion but the same sample length. The bandgaps grow with increasing Δn, but the frequencies of the out-of-band oscillation are the same for all three gratings.

2.3 Experimental results

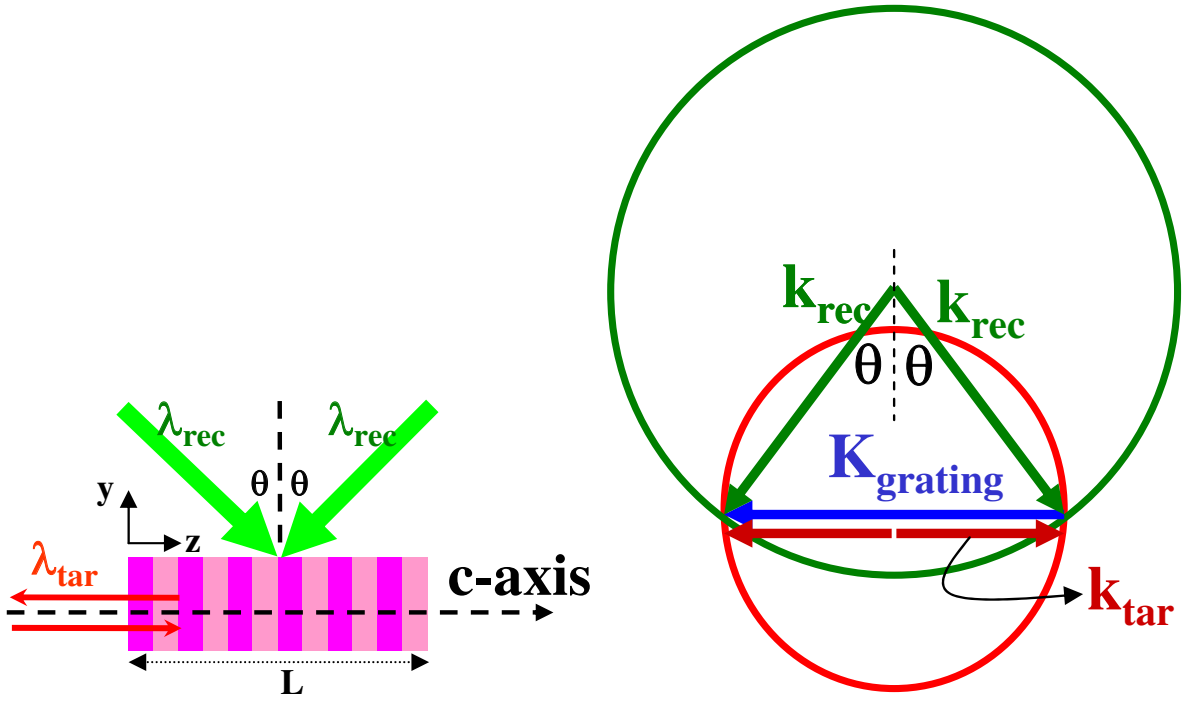

(a) Recording and readout geometry.

(b) The corresponding K-diagram

Figure 2.7: Recording a holographic grating in the transmission geometry and reading it out in the reflection geometry as a WDM filter.

2.3.1 Recording holographic WDM filters in reflection geometry in $LiNbO_3$

As shown in Fig. 2.7(a), we record a holographic grating in the transmission geometry and read out from the side. By properly choosing the half angle θ between the recording beams, we can control the (target) Bragg wavelength λ_{tar} when the grating is operated in the reflection geometry.

According to the K-diagram depicted in Fig. 2.7(b),

$$2k_{tar} = K_{grating} = 2k_{rec}\sin\theta \Longrightarrow \theta = \arcsin\left(\frac{n_{tar}\lambda_{rec}}{\lambda_{tar}}\right).$$

In our experiment, the parameters are as follows:

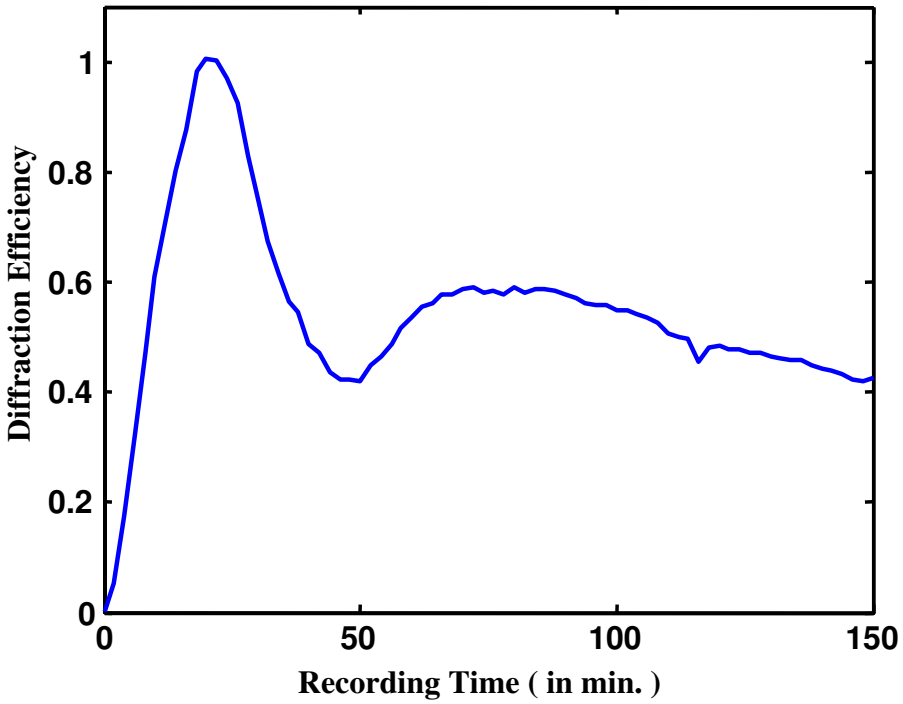

Figure 2.8: A recording curve of the holographic grating. (A stabilization system is incorporated into the recording setup for optimal stability.)

- The target readout wavelength at normal incidence $\lambda_{tar} = 1550$ nm.
- The recording wavelength $\lambda_{rec} = 514.5$ nm.
- The refractive index n_{tar} of the medium at λ_{tar}. We use $LiNbO_3$ samples in our experiment and $n_{tar} = 2.2116$.
- The half angle between the recording beams (outside the $LiNbO_3$ sample) is calculated to be $47.23°$.

A typical recording curve is shown in Fig. 2.8. A stabilization system has been incorporated into the system, and a piezo mirror is introduced to adjust the optical path of one of the recording beams in order to optimize the recording process. The "over-the-hump" behavior is rather obvious, and the modulation depth of the refractive index Δn is estimated to be 3.26×10^{-4}.

2.3.2 Measured filter response

The measured transmittance at normal incidence as a function of the incident wavelengths is plotted in Fig. 2.9. The Bragg wavelength (center wavelength) of the filter is estimated to be 1563.6 nm with a bandwidth of 0.115 nm (about 14.5 GHz). The criterion used to calculate them is as follows: we first find the two points of the filter whose through-channel transmittances are 0.5 dB higher than

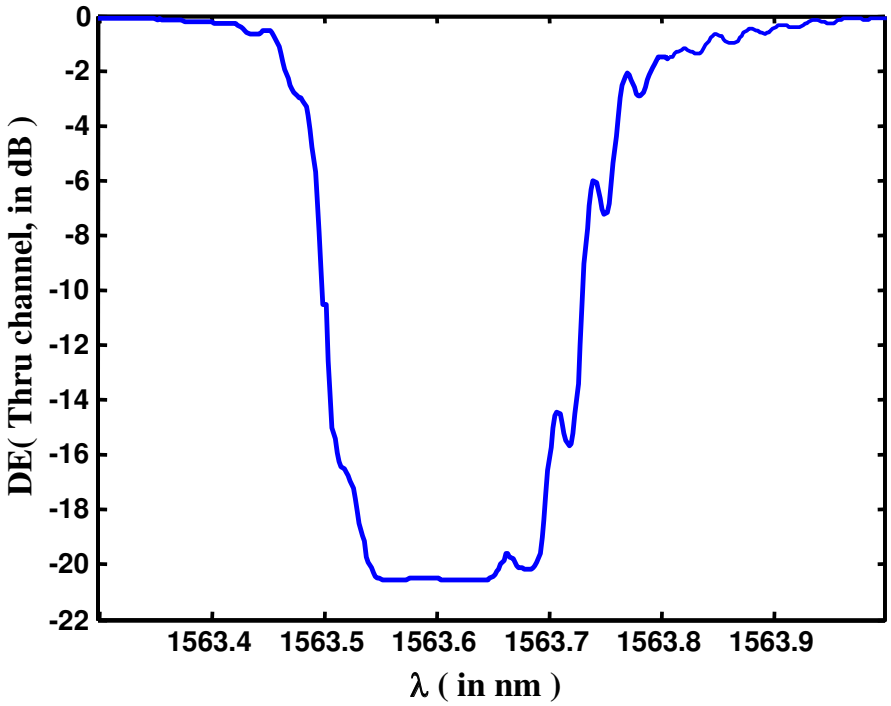

Figure 2.9: Measured filter transmittance in the through channel.

the minimum transmittance (that is, about 90% reflectance); they are defined as the edges of the filter stopband; Bragg wavelength is then calculated as the average of the two edge wavelengths, and the bandwidth is the difference between them. As we can see, the Bragg wavelength is not exactly the target wavelength we have designed. This indicates that the angle θ in the experimental setup can be slightly different from the theoretical value.

Bibliography

[1] H. Kogelnik. Coupled wave theory for thick hologram gratings. *Bell System Technical Journal*, 48(9):2909–2947, November 1969.

[2] A. Yariv. *Optical electronics in modern communications*. Oxford University Press, New York, 5th edition, 1997.

[3] Max Born and Emil Wolf. *Principles of Optics*. Cambridge, London, 7th edition, 1999.

[4] A. Yariv and P. Yeh. *Optical Waves in Crystals*. John Wiley & Sons, New York, 1984.

Chapter 3

Beam-width dependent filtering properties of volume holographic gratings

The finite dimension of the incident beam used to read out volume holographic gratings has interesting effects on their filtering properties. As the readout beam gets narrower, there is more deviation from the ideal response predicted for monochromatic plane waves. In this chapter, we experimentally explore some beam-width-dependent phenomena such as wavelength selectivities, angular selectivities and diffracted beam profiles. Volume gratings in both reflection and transmission geometries are investigated near 1550 nm. Numerical simulations utilizing the technique of Fourier decomposition provide satisfactory explanation and confirm that the spread of spatial harmonics is the main contributing factor.

3.1 Introduction

The coupling effects between plane waves mediated by VHGs has been treated rigorously before using various theoretical approaches, e.g., coupled-mode analysis[1, 2] and matrix formulation as discussed in the previous chapter. We will use these well-established results as given for our numerical simulations in this chapter.

Unlike thin gratings, VHGs are very sensitive to phase mismatch because of less ambiguity allowed in the momentum space. Thanks to its excellent selectivity, VHGs have become an ideal candidate for various promising technological applications such as neural networks[3], optical correlators[4] and holographic data storage[5, 6]. VHGs also prove useful in telecommunications. Essentially a one-dimensional photonic crystal when Δn is appreciable ($\Delta n \geq 10^{-4}$), holographic gratings in the reflection geometry can serve as superior filters[7, 8] for wavelength division multiplexing (WDM) thanks partly to their low crosstalk and readily engineered bandwidths.

The versatility of VHGs provides the motivation behind our work presented here. In this chapter,

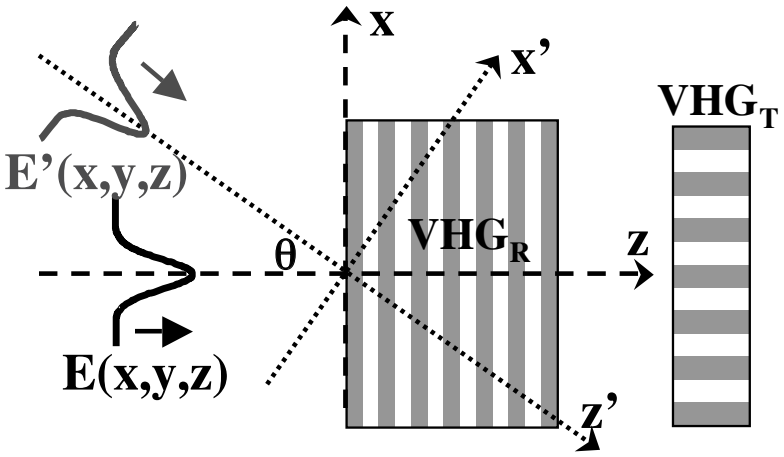

Figure 3.1: Theoretical configuration. The volume holographic grating has a transfer function $H(\mathbf{k_i}; \mathbf{k_d})$. $\mathrm{VHG_{R/T}}$ is a volume holographic grating in the reflection/transmission geometry.

we show the experimentally measured beam-width dependence of the wavelength selectivity, angular selectivity and diffracted beam profiles of VHGs in both the reflection and transmission geometries for s-polarized fields. With the help of Fourier analysis, we can satisfactorily explain the interesting discrepancies between the experimental data and the ideal results predicted for plane waves.

3.2 Theoretical consideration

In Fig. 3.1, we consider how a VHG affects a monochromatic incident optical field whose complex amplitude is $E_i(x, y, z)$. The length of the grating measures L along z-axis and is assumed to be infinite in the other two dimensions. With the knowledge of $f(x, y) = E_i(x, y, z = 0)$, the complex amplitude $E_i(x, y, z)$ can be uniquely determined by the diffraction integral in the case of propagation in a homogeneous medium:

$$E_i(x, y, z) = \iint F(k_{ix}, k_{iy}) exp[-j(k_{ix}x + k_{iy}y + k_{iz}z)] \frac{\mathrm{d}k_{ix}}{2\pi} \frac{\mathrm{d}k_{iy}}{2\pi}, \tag{3.1}$$

where $k_i = |\mathbf{k_i}| = \sqrt{k_{ix}^2 + k_{iy}^2 + k_{iz}^2}$ is the wavenumber of the monochromatic radiation and $F(k_{ix}, k_{iy})$ is the 2D Fourier transform of $f(x, y)$. Each $F(k_{ix}, k_{iy})$ represents a constituent plane-wave (or angular) component of $E_i(x, y, z)$. Basic Fourier transform relationships tell us that the narrower the incident beam is, the more spread-out its angular components will be. The "non-planeness" of $E_i(x, y, z)$ can be thought of as a natural manifestation of the linear combination of all plane wave elements $F(k_{ix}, k_{iy})e^{-j\mathbf{k_i}\cdot\mathbf{r}}$. For an obliquely incident optical field (tilted by θ), such as $E_i'(x, y, z)$

in Fig. 3.1, a simple change of variable can be used to simplify the mathematical expressions:

$$\begin{cases} x' &= x\cos\theta + z\sin\theta \\ z' &= -x\sin\theta + z\cos\theta. \end{cases}$$

Incidentally, the angle of incidence, θ, is the angle between the beam propagation direction and the normal of the input face $z = 0$. Unless noted otherwise, θ is measured inside the VHG.

The presence of the VHG with frequency response $H(\mathbf{k_i}; \mathbf{k_d})$ provides the opportunity for some of the plane wave components $F(k_{ix}, k_{iy})e^{-j\mathbf{k_i}\cdot\mathbf{r}}$ in the incident field to be diffracted and gives rise to the (diffracted) plane wave components:

$$F(k_{ix}, k_{iy})H(\mathbf{k_i}; \mathbf{k_d})e^{-j\mathbf{k_d}\cdot\mathbf{r}}.$$

Since this is a linear system, the diffracted beam will be the integral sum of all diffracted plane waves:

$$E_d(x, y, z) = \iint F(k_{ix}, k_{iy})H(\mathbf{k_i}; \mathbf{k_d})e^{-j\mathbf{k_d}\cdot\mathbf{r}}\frac{\mathrm{d}k_{ix}}{2\pi}\frac{\mathrm{d}k_{iy}}{2\pi}. \tag{3.2}$$

Placing a detector at the output plane Σ_o to measure the diffracted field intensity, the diffraction efficiency η can be calculated from the diffracted and transmitted field intensities:

$$\eta = \frac{\iint_{\Sigma_o} |E_d(x, y, z)|^2 \mathrm{d}\Sigma_o}{\iint |E_i(x, y, z = L)|^2 \mathrm{d}x\mathrm{d}y + \iint_{\Sigma_o} |E_d(x, y, z)|^2 \mathrm{d}\Sigma_o}. \tag{3.3}$$

Another parameter of interest is the group delay, which specifies the dispersive properties of the VHG. At Σ_o, a diffracted plane wave component can be written as $A(\omega)e^{j\Phi(\omega)}$, where $A(\omega)$ and $\Phi(\omega)$ are both real quantities and can be uniquely determined from the diffracted field representation; ω is the angular frequency of the radiation. The group delay τ_d of the diffracted plane wave component is defined as

$$\tau_d = \frac{\partial\Phi(\omega)}{\partial\omega}. \tag{3.4}$$

However, the diffracted beam consists of a large number of diffracted plane wave components, and we define the group delay of the diffracted beam τ_D as the (intensity) weighted average of the respective group delays of its constituent plane waves.

The derivation of the appropriate transfer function $H(\mathbf{k_i}; \mathbf{k_d})$ of a VHG has been treated by an abundance of literature[1, 2, 9]. We shall therefore use the results in our simulations as given.

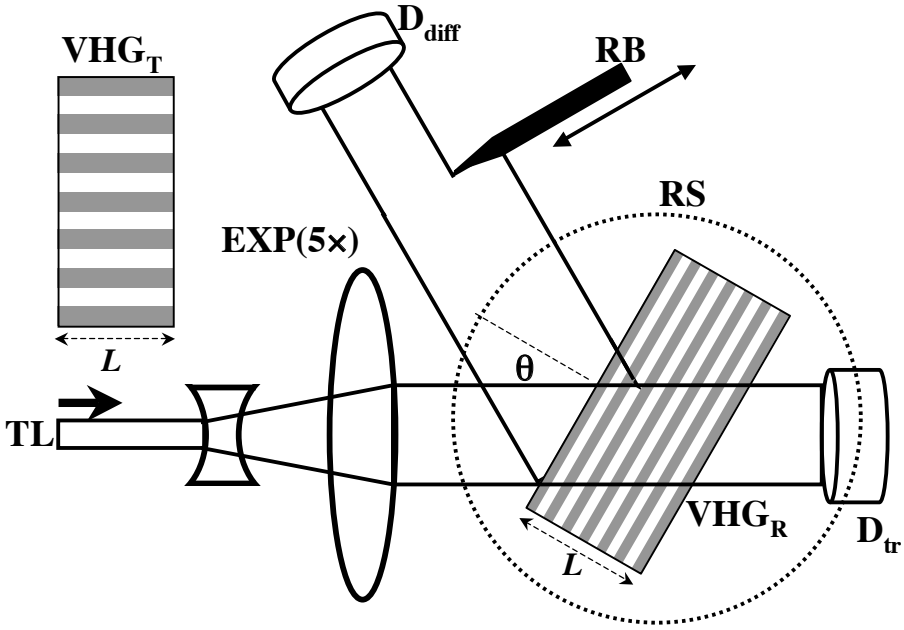

Figure 3.2: Experimental setup. TL: tunable laser source (from 1520 nm to 1600 nm); EXP(5×): beam expander; $VHG_{R/T}$: volume holographic grating in the reflection/transmission geometry; $D_{tr/diff}$: detector for the transmitted/diffracted beam; RS: rotational stage; RB: razor blade controlled by a translation stage for measurement of the diffracted beam profile.

3.3 Numerical simulations and experimental results

In this section, we present the experimental results and numerical simulations of VHGs in the reflection and transmission geometries separately. In all cases, the electric fields are perpendicular to the plane of incidence (s-polarized). For each geometry, we first describe the experimental setup and then compare the measurements and theoretical predictions for two different beam widths. All VHGs used are provided by Ondax Inc. and recorded in photosensitive glass plates. The absorption inside the glass of the wavelengths used is negligible.

3.3.1 Reflection geometry

In telecommunication, WDM filters are needed to select and/or manipulate a desired wavelength from a bank of available channels. In reconfigurable communication systems, tunable optical filters play an increasingly important part. Examples include tunable arrayed waveguide gratings (AWG) [10], wavelength tuning based on varying temperature [11] and the application of stress [12]. Tunable filters have also been realized in reflection-geometry VHGs by means of angular tuning[13]. To appreciate and efficiently utilize this filtering configuration, it is important to know how oblique incidence impacts the filtering properties.

3.3.1.1 Experimental setup

The experimental setup is schematically shown in Fig. 3.2; a reflection-geometry VHG, denoted by VHG_R, whose grating period Λ is about 532 nm (the corresponding Bragg wavelength at normal incidence is about 1581 nm) is mounted on a rotational stage for precise angular control. The light from a tunable laser source (tuning range 1520 nm $\sim$ 1600 nm) is channeled through a fiber collimator (Newport model f-col-9-15) and then used to conduct measurements. The interaction length at normal incidence L is 14 mm. The output laser beam profile from the collimator is Gaussian with a diameter of 0.5 mm, which is the spatial width across its intensity profile where it drops to $1/e^2$ of the peak value. A beam expander (5×) consisting of two cylindrical lenses (a negative lens with focal length -15 mm and a positive lens whose focal length is 75 mm) can be moved in to widen the incident beam. The angular spread of the (un-)expanded beam is calculated to be (0.15°)0.03° inside the glass, corresponding to (0.225°)0.045° in the air.

For each incident angle θ and wavelength λ of interest, the power of both the transmitted and diffracted beams are monitored, from which the diffraction efficiency can be calculated. A razor blade motion-controlled by a translation stage can be moved across the diffracted beam to measure its intensity profile. The distance between the razor blade and the output face is about 50 mm.

3.3.1.2 Wavelength selectivity

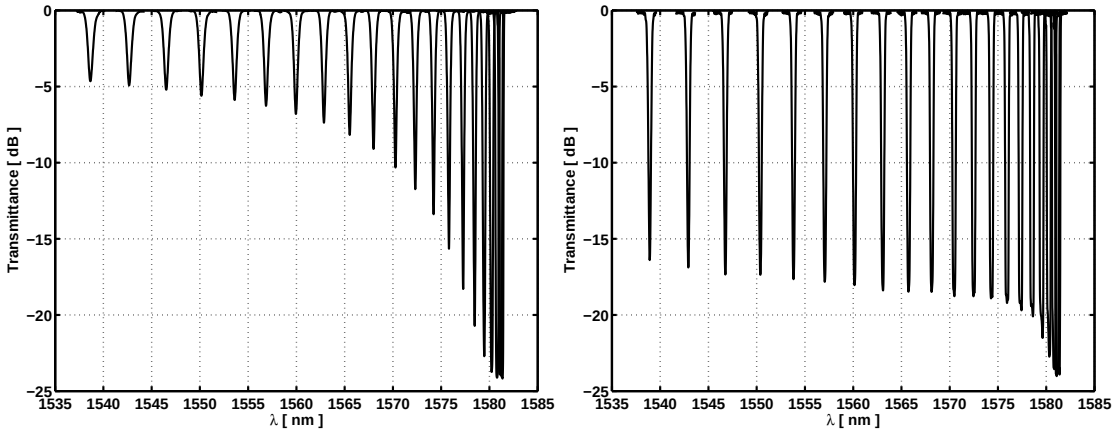

(a) $W = 0.5$ mm (b) $W = 2.5$ mm

Figure 3.3: Reflection geometry. Wavelength selectivity curves from normal to oblique incidence. The measured curves in both parts (a) and (b) correspond, from right to left, to incident angles 0°, 1°, 2°, ... 19° outside the glass sample (about 0° to 13.3° inside the glass).

To measure wavelength selectivity curves, the incident angle θ is first set to one of a series of predetermined values, from 0° to 13.3°, and then a wavelength scan is carried out. Fig. 3.3(a) shows the results obtained with the narrow/unexpanded beam B_N (beam width $W = 0.5$ mm); the transmittance ($= 1 - \eta$) curves are plotted out in dB. Each valley-like feature corresponds to

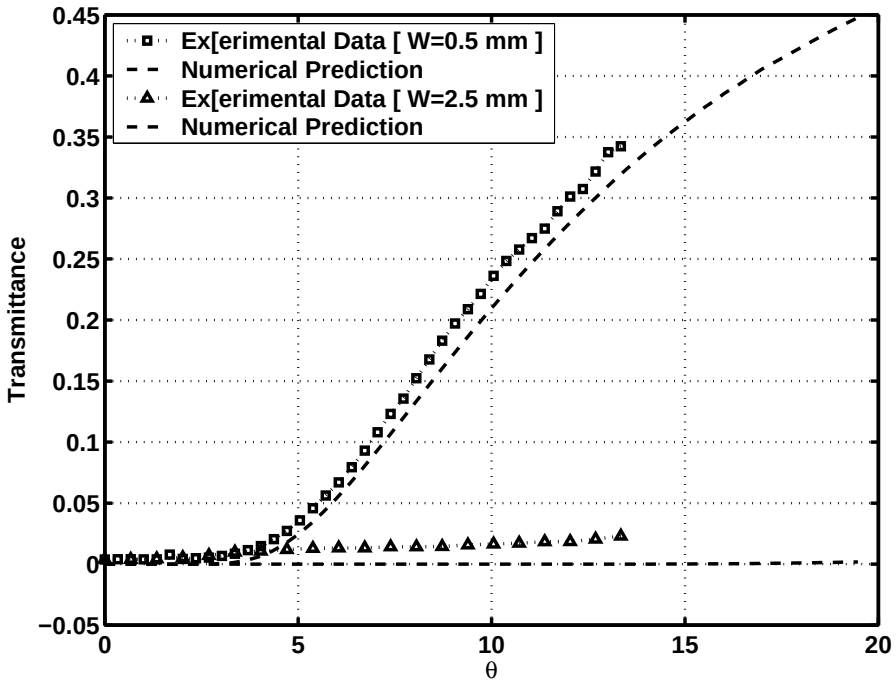

Figure 3.4: Summary of the wavelength selectivity measurements. The increasing transmission of the narrow beam at oblique incidence contrasts strongly with the transmission of the expanded beam, which does not increase much at oblique incidence.

strong coupling of the incident beam to the diffracted beam, and the wavelength of its transmission minimum, defined as the Bragg wavelength λ_B, is specified by the incident angle through the relationship

$$\lambda_B = 2n\Lambda \cos\theta. \tag{3.5}$$

The same set of measurements done for the wide/expanded beam B_W (beam width 2.5 mm) is summarized in Fig. 3.3(b). As we can see, the almost constant transmittance of B_W at oblique incidence contrasts strongly with the increasing trend of B_N, which is predicted by numerical simulations as well. The quantitative comparison is further summarized in Fig. 3.4; the numerical simulations (calculated with an index modulation $\Delta n = 4.7 \times 10^{-4}$) agree very well with the experimental data.

3.3.1.3 Angular selectivity

To measure the angular selectivity curves, the incident angle is first set to one of a series of predetermined values. With the wavelength tuned to the appropriate Bragg wavelength λ_B, an angular scan is then performed. Fig. 3.5(a) and Fig. 3.5(b) show the measured angular selectivities for B_N and B_W, respectively. The 0.5 dB angular bandwidths $\Delta\theta_{BW}$ are summarized in Fig. 3.6 along with the numerically simulated results.

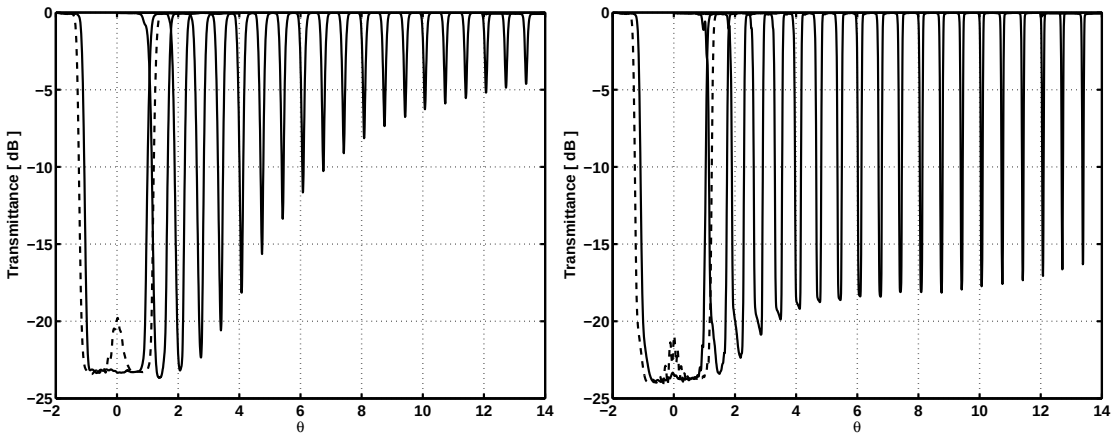

(a) $W = 0.5$ mm (b) $W = 2.5$ mm

Figure 3.5: Reflection geometry. Angular selectivity curves from normal to oblique incidence. The solid curves in both parts (a) and (b) correspond, from left to right, to incident angles 0°, 1°, 2°, ... 19° outside the glass sample (about 0° to 13.3° inside the glass). The dashed curves in both plots are measured for an incident angle of 0.5° outside the glass.

Again, the minimum transmittance increases much more rapidly for B_N than for B_W as we tilt the beam from normal to oblique incidence. An interesting feature common to both B_N and B_W is the dramatic decrease of the angular bandwidth $\Delta\theta_{BW}$ at oblique incidence.

Two of the angular selectivity curves, as traced out by dashed lines in Figs. 3.5(a) and 3.5(b), near normal incidence have a funny "twin-valley" (ω) shape. Each of them can be thought of as the "fusion" of two normal, single-dip angular selectivity curves positioned close together. Owing to geometrical degeneracy, the effects caused by a positive θ is equivalent to those caused by a negative one in the reflection geometry; whenever θ is small compared with $\Delta\theta_{BW}$, such "fusion" will inevitably occur. This is the reason why we observe the increase of $\Delta\theta_{BW}$ prior to its drastic decrease.

The angular and wavelength selectivity curves are not behaving independently. The relationships between them can be unraveled if we consider the spatial harmonic components of the incident beam. At normal incidence, the VHG's angular bandwidth $\Delta\theta_{BW}$ is wide and diffracts most spatial harmonics contained within both B_N and B_W; therefore η approaches 100%. If we slightly tilt the incident beam away from the normal, we effectively increase $\Delta\theta_{BW}$, and almost all spatial harmonics remain strongly diffracted and the wavelength selectivity curve does not change much. Around normal incidence where we get the ω-shaped angular selectivity, the wavelength selectivity of B_N differs little from that of B_W. However, as we tilt the incident beam past an angular threshold (about 1° in our case), $\Delta\theta_{BW}$ decreases sharply, and only a smaller portion of the spatial harmonic content of B_N gets diffracted efficiently by the grating. At the same time, B_W is not affected as much thanks to its narrower spatial frequency spread. At oblique incidence B_W has a higher diffraction efficiency because a bigger part of the energy of B_N spills out of the $\Delta\theta_{BW}$ angular stop band along

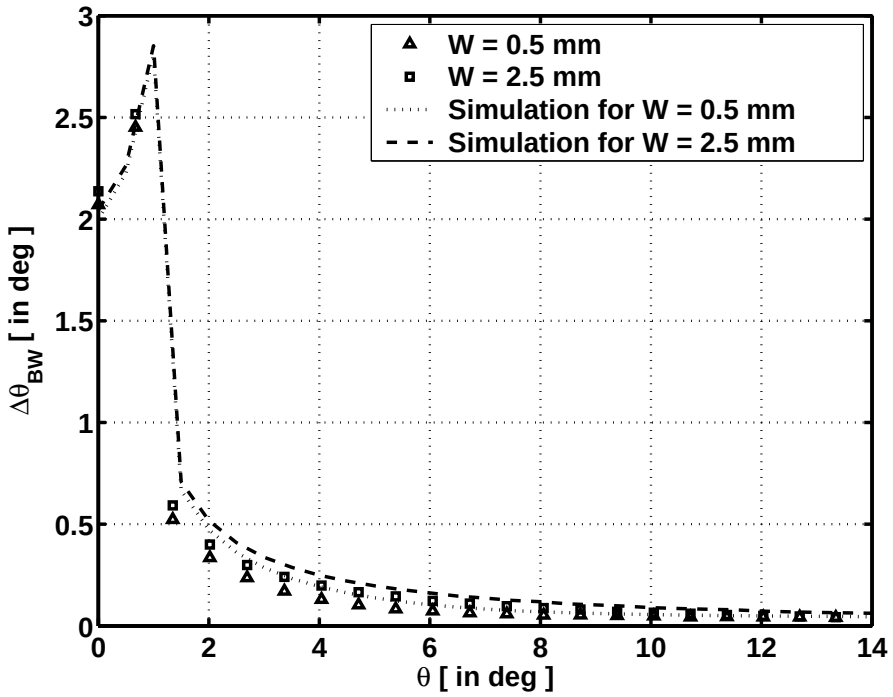

Figure 3.6: Summary of the angular selectivity measurements. The 0.5 dB angular bandwidth, $\Delta\theta_{BW}$, is plotted against the angle of incidence θ. Numerical simulations are seen to agree well with the experimental data.

with the undiffracted spatial components. To put it succinctly, the product of a VHG's angular selectivity curve and the angular spectrum of the incident beam determines the diffraction efficiency and filter shape of the VHG.

3.3.1.4 Diffracted beam profiles

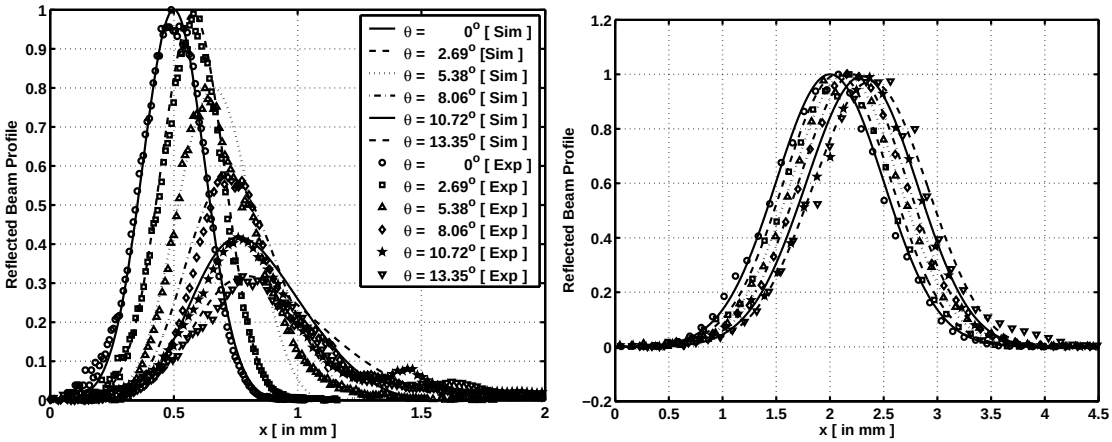

(a) $W = 0.5$ mm (b) $W = 2.5$ mm

Figure 3.7: Reflection geometry. Diffracted beam intensity profiles from normal to oblique incidence.

In Fig. 3.7(a) and Fig. 3.7(b), we show the experimentally measured and numerically simulated diffracted beam intensity profiles for B_N and B_W, respectively. The legend in Fig. 3.7(a) applies to both plots. At oblique incidence, we see that the diffracted beam of B_N is flattened out from the ideal Gaussian profile. On the contrary, the diffracted beams of B_W maintain their Gaussian-like profiles. This phenomenon is attributed to the strong angular filtering suffered by B_N thanks to the VHG: its wider diffracted beam profiles are results of less diffracted spatial harmonic components. This effect is not readily observable for B_W because most of its spatial harmonics are diffracted. Again, the simulations can accurately predict the measured data.

3.3.2 Transmission geometry

3.3.2.1 Experimental setup

For the measurements of a VHG in the transmission geometry, we replace VHG_R with VHG_T in Fig. 3.2. The only differences are the grating vector orientation and the position of the detector for the diffraction beam. The intensity profile of the diffracted beams are measured 50 mm from the output face.

The grating period Λ of the VHG used is about 5.94 μm. Since the Bragg condition in the transmission geometry is equivalent to $\lambda = 2n\Lambda \sin\theta$, the Bragg angle θ_B at 1560 nm is roughly 5°. The index modulation Δn is estimated to be 4.7×10^{-4}, and the interaction length L at normal

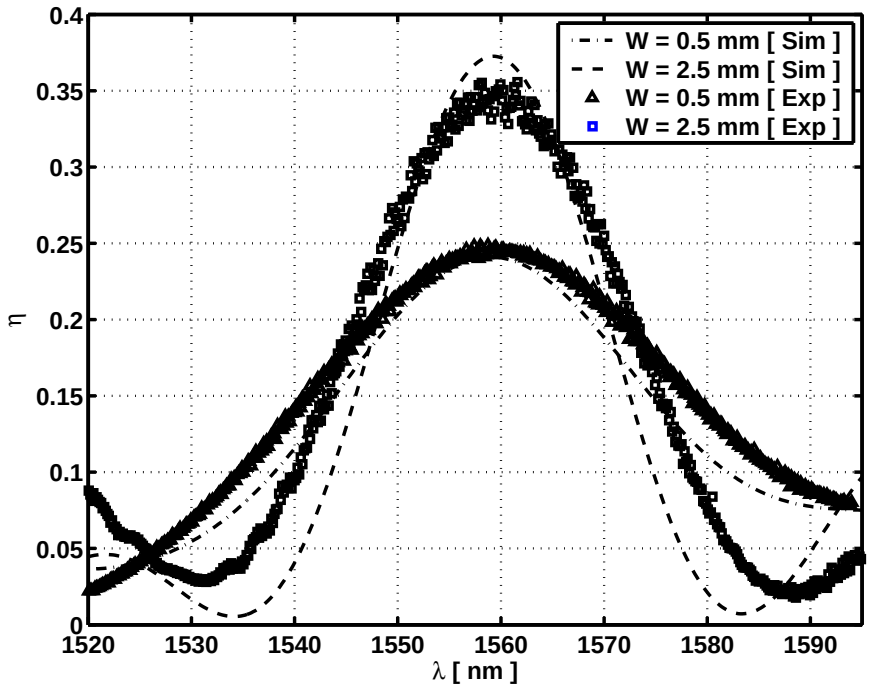

Figure 3.8: Transmission geometry. Wavelength selectivity curves for beam widths 0.5 mm and 2.5 mm.

incidence is 3 mm. For plane waves, $\eta = \sin^2(\frac{\pi \Delta n L}{\lambda \cos\theta})$ when Bragg matched. We see that η reaches 100% when the parameter $\frac{\pi \Delta n L}{\lambda \cos\theta}$ is equal to 0.5π, $1.5\pi \ldots$. In our experiments, this parameter turns out to be 0.9π, and therefore the maximum value of η will not be registered when Bragg-matched but when a phase mismatch is present. This behavior transpires because part of the diffracted beam is coupled back into the transmitted beam and η is reduced.

3.3.2.2 Wavelength selectivity

The procedure for measuring the wavelength selectivity curves is as follows: we first rotate the VHG such that $\theta \sim 5.1^\circ$ and the Bragg condition is satisfied for $\lambda = 1590$ nm, and then the wavelength is scanned from 1520 nm to 1600 nm. The resulting selectivity curves for B_N and B_W are shown together in Fig. 3.8. Along with the measured data we also plot the numerically simulated curves. The selectivity curves are seen to be quite wide. This is because of the very shallow incident angle (small value of θ).

3.3.2.3 Angular selectivity

The angular selectivity curves are measured by scanning around the Bragg angle when the wavelength is fixed at 1560 nm. The measured curves for B_N and B_W along with the theoretically predicted responses are plotted in Figs. 3.9(a) and 3.9(b). We do not get the maximum diffracted intensity

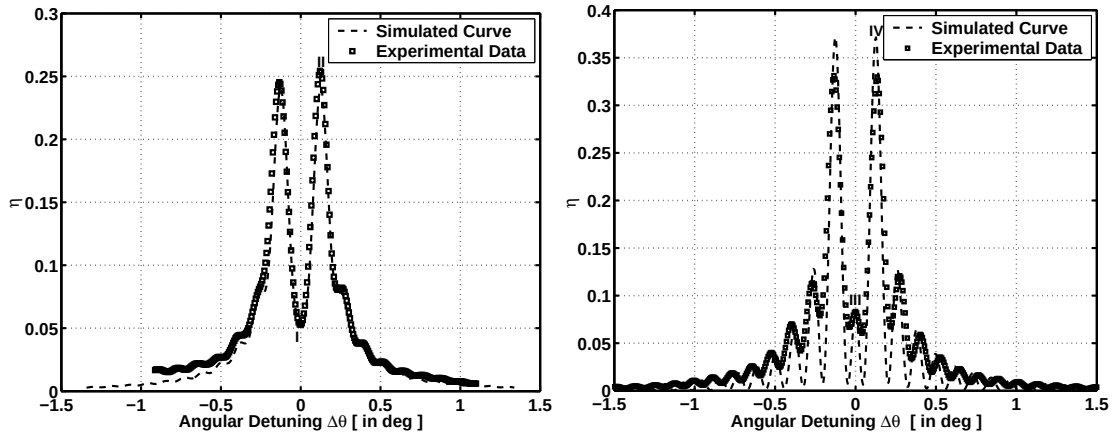

(a) $W = 0.5$ mm (b) $W = 2.5$ mm

Figure 3.9: Transmission geometry. Angular selectivity curves around Bragg angle $\theta_B \approx 5°$.

at the Bragg angle but at a certain amount of angular detuning ($\Delta\theta \sim \pm 0.14°$). As we increase the absolute angular detuning $|\Delta\theta|$ from 0°, our angular selectivity curves are traced out almost symmetrically around the Bragg angle θ_B. The numerical simulation matches the experimental data so well that even the absence/presence of a local "bump" at θ_B for B_N/B_W is accurately depicted.

3.3.2.4 Diffracted beam profiles

We plot two measured diffracted beam profiles for both B_N and B_W in Fig. 3.10. The normalized intensity profiles (a), (b), (c) and (d) correspond to indices in Roman numerals from I to IV as marked in Figs. 3.9(a) and 3.9(b). While the diffracted beam profiles (b), (c) and (d) remain Gaussian, the beam profile (a) shows a dip in the center (as predicted by the simulations). The explanation for this interesting phenomenon is that the phase relationship between the constituent diffracted plane wave components dictates destructive interference at the center of the diffracted beam.

3.4 Conclusion

Taking advantage of the technique of Fourier decomposition combined with plane wave solutions to the VHGs proves to be extremely useful for accurately characterizing and predicting the diffraction effects suffered by a finite incident beam owing to a VHG. Such characterization will be useful for evaluating the performance of optical systems employing VHGs, determining the optimal parameters at the design phase and improving existing optical systems.

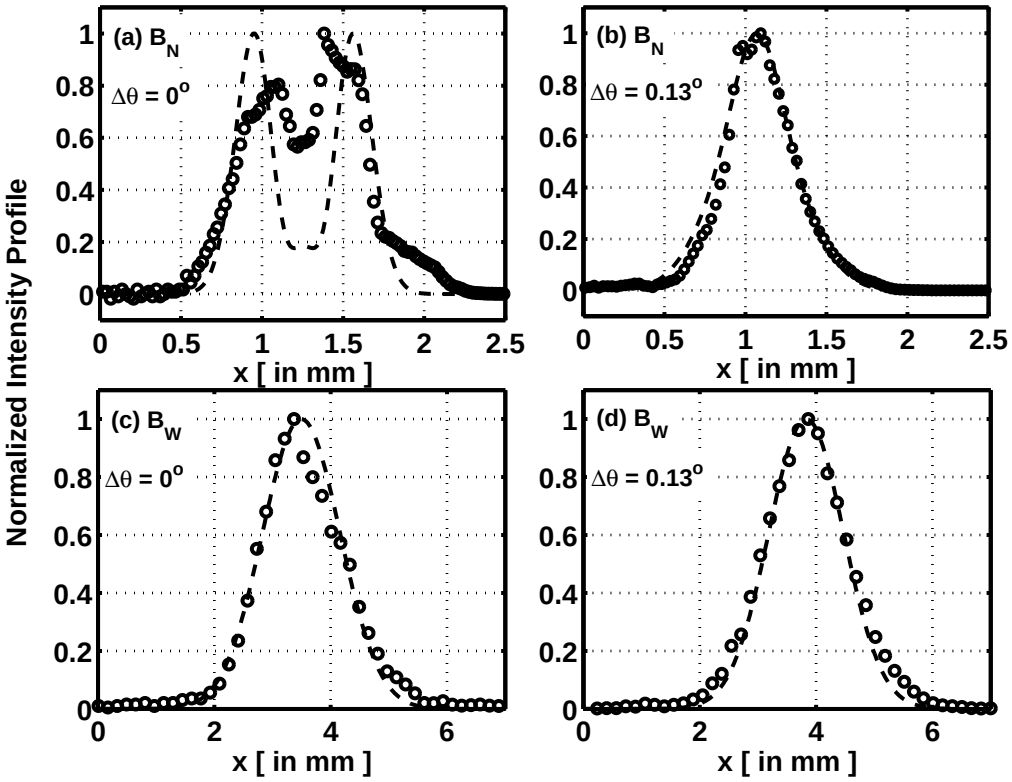

Figure 3.10: Normalized diffracted intensity beam profiles in the transmission geometry around Bragg angle $\theta_B \approx 5°$; $\Delta\theta = \theta - \theta_B$. All beam profiles are measured 50 mm from the output face. The circles represent experimental measurements and the dashed lines are the numerical simulations.

Bibliography

[1] H. Kogelnik. Coupled wave theory for thick hologram gratings. *Bell System Technical Journal*, 48(9):2909–2947, November 1969.

[2] J. W. Goodman. *Fourier Optics*. The McGraw-Hill Companies, Inc., Singapore, 1996.

[3] D. Psaltis, D. Brady, X. G. Xu, and S. Lin. Holography in articficial neural networks. *Nature*, 343:325–330, January 1990.

[4] M. Levene, G. J. Steckman, and D. Psaltis. Method for controlling the shift invariance of optical correlators. *Applied Optics*, 38:394–398, January 1999.

[5] D. Gabor. Associative holographic memories. *IBM Journal of Research and Development*, 13(2):156, 1969.

[6] D. Psaltis and F. Mok. Holographic memories. *Scientific America*, 273:70–76, November 1995.

[7] G. A. Rakuljic and V. Leyva. Volume holographic narrow-band optical filter. *Optics Letters*, 18:459–461, March 1993.

[8] S. Breer and K. Buse. Wavelength demultiplexing with volume phase holograms in photorefractive lithium niobate. *Applied Physics B*, 66:339–345, March 1998.

[9] P. Yeh. *Optical Waves in Layered Media*. John Wiley & Sons, New York, 1991.

[10] V. Polo, B. Vidal, J. L. Corral, and J. Marti. Novel tunable photonic microwave filter based on laser arrays and N×N AWG-based delay lines. *IEEE Photonics Technology Letters*, 15:584–586, April 2003.

[11] S. Y. Li, N. Q. Ngo, S. C. Tjin, P. Shum, and J. Zhang. Thermally tunable narrow-bandpass filter based on a linearly chirped fiber Bragg grating. *Optics Letters*, 29:29–31, January 2004.

[12] G. A. Ball and W. W. Morey. Compression-tuned single-frequency Bragg grating fiber laser. *Optics Letters*, 19:1979–1981, December 1994.

[13] H. T. Hsieh, G. Panotopoulos, M. Liger, Y. C. Tai, and D. Psaltis. Athermal holographic filters. *IEEE Photonics Technology Letters*, 16:177–179, January 2004.

Chapter 4

Athermal holographic filters

4.1 Introduction

Holographic filters[1] have been widely used for wavelength division multiplexing (WDM) filtering applications[2, 3]. Temperature dependence is a critical concern for telecommunications. In thin film filter technology, by proper selection of materials, we are able to combat the thermal drift of Bragg wavelengths[4]. Athermal filter designs were also reported for arrayed-waveguide gratings (AWGs)[5] and fiber Bragg gratings (FBGs)[6]. However, such flexibility is not available in bulk holographic filters. In this chapter a feasible system solution for athermalizing holographic filters will be proposed and experimentally shown to compensate for the effects of temperature changes.

4.2 Theory

A grating holographically imprinted inside a recording material can be operated as a WDM filter in the reflection geometry, as shown in Fig. 4.1. The wavelength satisfying the grating equation

$$\lambda_B = 2n(T_0)\Lambda(T_0)\cos\theta_B \tag{4.1}$$

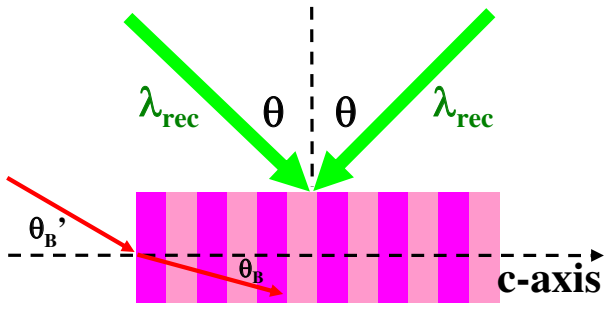

Figure 4.1: Recording a holographic grating inside a $LiNbO_3$ crystal at λ_{rec}= 488 nm in the transmission geometry and then operating it as a WDM filter in the reflection geometry.

will be strongly reflected, whereas the other wavelengths pass through the filter unaffected. In Eq. (4.1), $n(T_0)$ is the refractive index of the material at λ_B at temperature T_0, and $\Lambda(T_0)$ is the period of the index grating at T_0. By inspecting Eq. (4.1), we notice that we can Bragg match the grating to a shorter wavelength if we tilt the incident beam away from the normal.

Temperature changes affect holographic filters mainly through two mechanisms: (Other possible effects will be neglected here, e.g., the thermal dependence of the piezoelectric tensor will manifest itself when stress is being applied.)

1. Thermal expansion or contraction of the bulk material (in our experiments, $LiNbO_3 : Fe$).

2. Thermal dependence of the dielectric constant of the bulk material.

Assume that the Bragg wavelength of the filter is λ_B corresponding to an incident angle θ_B (θ_B is the angle measured inside the crystal, whereas θ'_B is measured outside the crystal) at temperature T_0. When the temperature changes to $T_0 + \Delta T$, the Bragg wavelength of the filter will have a corresponding shift and move to $\lambda_B + \Delta\lambda$. If we adjust the incident angle by $\Delta\theta$ such that the Bragg wavelength shifts back to λ_B, we will have

$$\lambda_B = 2n(T_0 + \Delta T)\Lambda(T_0 + \Delta T)\cos(\theta_B + \Delta\theta). \tag{4.2}$$

If the thermal expansion coefficient (TEC) and the refractive index dependence on temperature are both linear within the temperature range of interest, we have $n(T_0 + \Delta T) \approx n(T_0)(1 + a\Delta T)$ and $\Lambda(T_0 + \Delta T) \approx \Lambda(T_0)(1 + b\Delta T)$. From Eqs. (4.1) and (4.2), we can derive a relation between $\Delta\theta$ and ΔT for a constant Bragg wavelength in spite of temperature changes:

$$\frac{\cos(\theta_B + \Delta\theta)}{\cos\theta_B} = \frac{1}{(1 + a\Delta T)(1 + b\Delta T)}. \tag{4.3}$$

Since both thermal coefficients a and b are positive[7, 8], we conclude that as the temperature rises, the Bragg wavelength of a given filter will shift upward, i.e., to a longer wavelength. To compensate for such a shift, we tilt the beam away from the normal. On the other hand, to undo the effect caused by a temperature drop, we adjust the beam toward the normal.

Based on Eq. (4.3), we propose an athermal design to maintain the Bragg wavelengths of WDM filters as invariant as possible with respect to temperature fluctuations. The principle of operation is illustrated in Fig. 4.2. We use a bimetallic composite beam to control the direction of the incident beam. The device makes use of the TEC discrepancy between two properly chosen materials (in our case, aluminum and silicon) and deflects as the temperature changes[9]. We operate the filter away from normal incidence because compensation for negative temperature drifts cannot be carried out near normal incidence and to avoid nonlinearities ($\Delta\theta$ is a highly nonlinear function of ΔT near normal incidence).

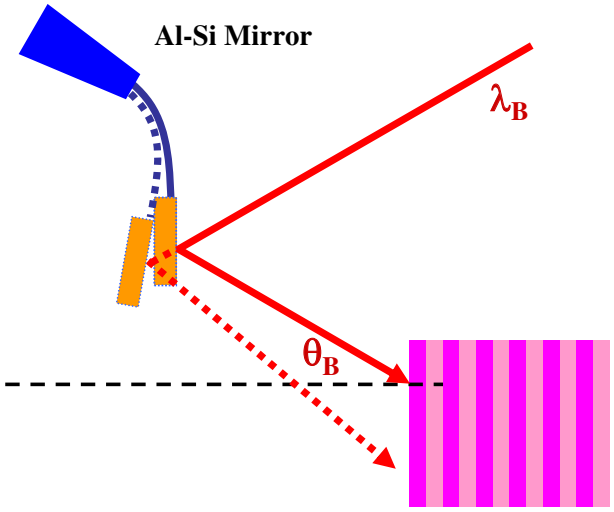

Figure 4.2: The athermal design of a holographic filter utilizing an Al-Si composite beam microactuator whose tip deflects as the temperature changes.

4.3 Experiment and results

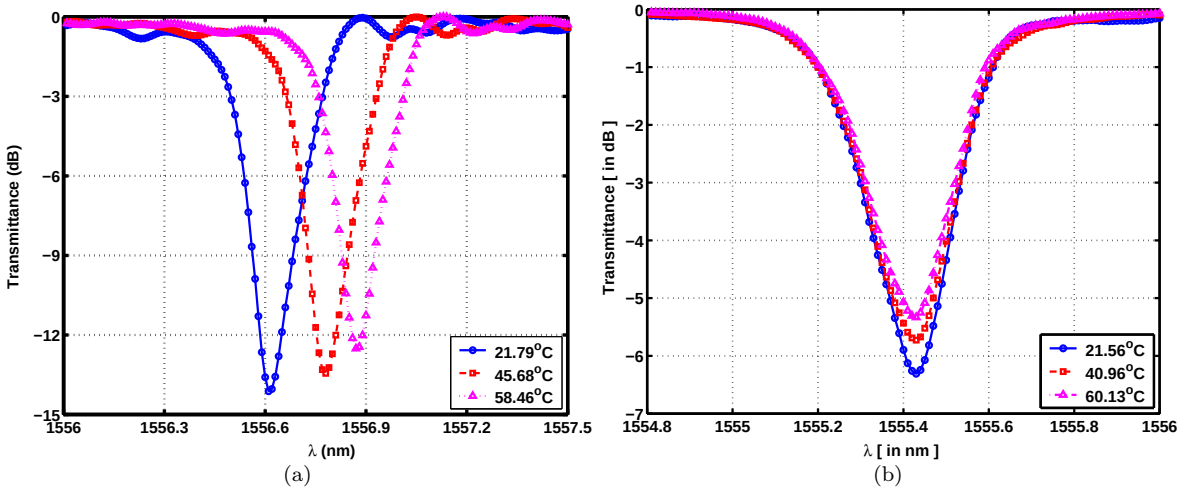

Figure 4.3: Filter response measured in the through channel at $\theta'_B = 5°$ for three different temperatures (a) without and (b) with the compensating MEMS mirror.

In our experiments, holographic filters are recorded in an iron-doped lithium niobate ($LiNbO_3$: Fe, 0.05 wt. % Fe_2O_3) crystal by interfering two coherent continuous wave (cw) laser beams inside the crystal, as shown in Fig. 4.1. The crystal sample dimensions are 2.0 cm × 1.0 cm × 0.3 cm with its c-axis running parallel to the longest edge, and the concentration of Fe^{2+} is 1.28×10^{24} m^{-3}. A stabilization system has been incorporated into the recording setup in order to prevent the interference pattern from drifting. By properly choosing the angle 2θ between the recording beams we are able to control the Bragg wavelength of the grating operated in the reflection geometry.

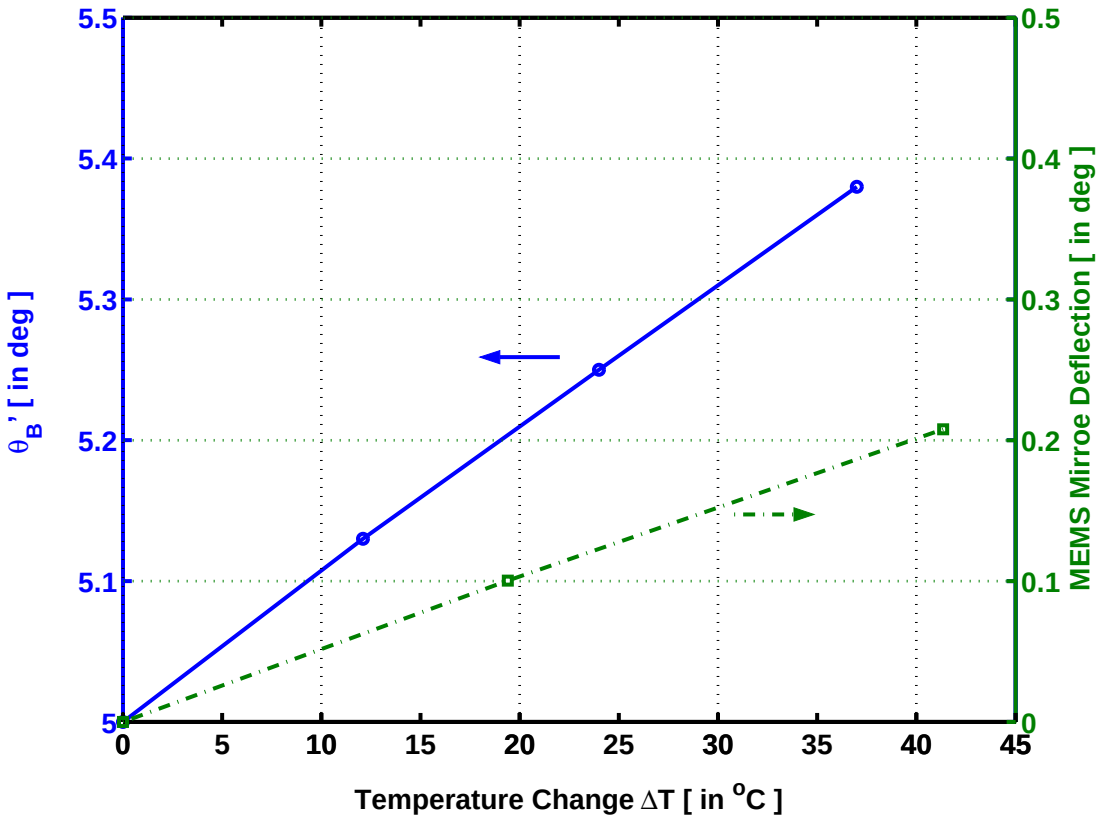

Figure 4.4: The solid curve represents the calculated optimal compensation angle θ'_B as a function of temperature change ΔT. The dash-dot curve is the measured angular deflection of the MEMS mirror subject to ΔT.

The transmittance of a typical filter at an incident angle $\theta'_B = 5°$ is shown in Fig. 4.3(a) for three different temperatures. The Bragg wavelength λ_B of the recorded filter at 21.79°C is measured to be 1556.61 nm. The filter efficiency is dropping due to hologram decay at elevated temperatures since the hologram was not thermally fixed[10].

To specify the MEMS mirror parameters, we first figure out the Bragg wavelengths for a series of incident angles at four different temperatures (21.79°C, 33.36°C, 45.68°C, 58.46°C). Temperature monitoring is made possible by reading the resistance off a thermistor in close contact with the $LiNbO_3$ crystal when the whole system is in thermal equilibrium. A thermoelectric (TE) cooler is used to control the temperature of the system. The Bragg wavelength corresponding to the incident angle $\theta'_B = 5°$ ($\theta_B \approx 2.25°$) at the lowest temperature is chosen as the target wavelength that will be maintained constant through angular compensation. By doing a fit of the data to Eq. (4.3), we end up with the optimal compensation angles as a function of temperature change. This is plotted as a solid line in Fig. 4.4.

Our data suggest that for operation around an incident angle $\theta'_B = 5°$, an angular correction of

1.18° will be required for a temperature change of 100°C. The aluminum-silicon composite beam was designed to deflect about 0.59° for a temperature change of 100°C.

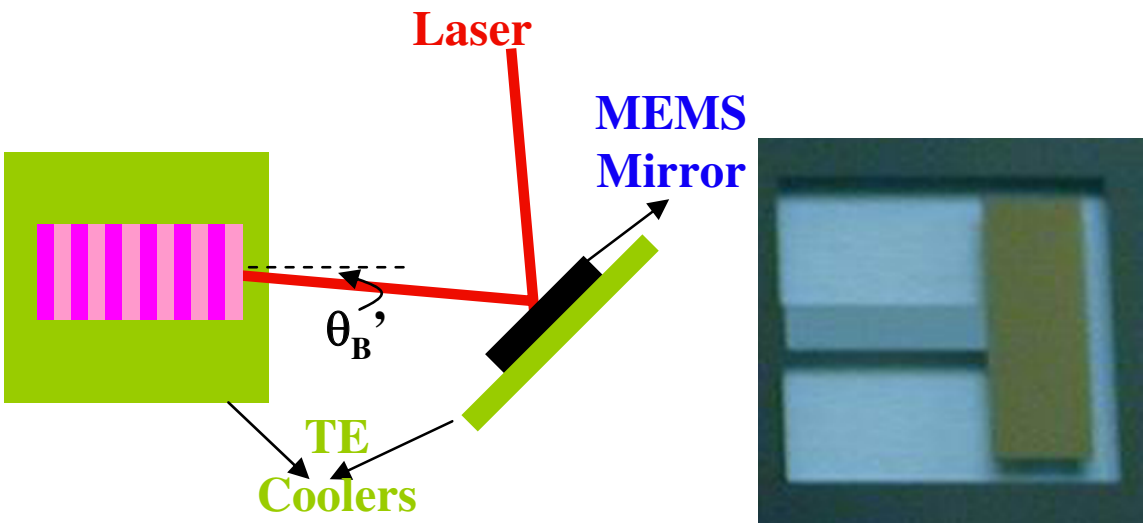

Figure 4.5: Experimental setup combining the thermally driven MEMS mirror with the recorded holographic filter to realize the athermal filter design. A picture of the MEMS mirror is also shown.

A photograph of the MEMS mirror is shown in Fig. 4.5. It is composed of two parts: a mirror part (surface dimensions 1.0 mm × 3.0mm, 50 nm of gold deposited on 0.45 mm silicon gives a reflectance of 85% at 1550 nm) and a beam (surface dimensions 2.0 mm × 0.5 mm, 500 nm aluminum deposited on 0.025 mm silicon), which deflects as the temperature varies. The measured deflection angle of the mirror as a function of temperature is also plotted in Fig. 4.4.

We mount the holographic filter and the MEMS mirror on two separate TE coolers as depicted in Fig. 4.5. Two identical thermistors are used to monitor the temperatures of the filter and the mirror. The output from a tunable laser is reflected off the mirror toward the filter at an (outside) incident angle of 5 degrees. At this point both the filter and the mirror are at room temperature. The filter response is measured, and the Bragg wavelength is determined. Then the TE coolers are turned on, and the temperatures of both are raised. The readings of the two thermistors are kept the same throughout the measurements of filter response. The filter shapes at $\theta'_B = 5°$ for three different temperatures are plotted in Fig. 4.3(b). Compared with Fig. 4.3(a), the drift of the Bragg wavelength is indeed compensated for by the deflection of the mirror. The compensation can be done easily in practice because the response time of the MEMS mirror is much shorter than that of the bulkier $LiNbO_3$ crystal.

In Fig. 4.6 we plot the Bragg wavelengths measured with the athermal design for three different incident angles. The dashed lines indicate the drifts of Bragg wavelengths due to the raised temperature in the absence of mirror compensation. We can see that for $\theta'_B = 5°$, the Bragg wavelength remains constant between 21°C and 60°C, which corroborates the plausibility of our athermal design.

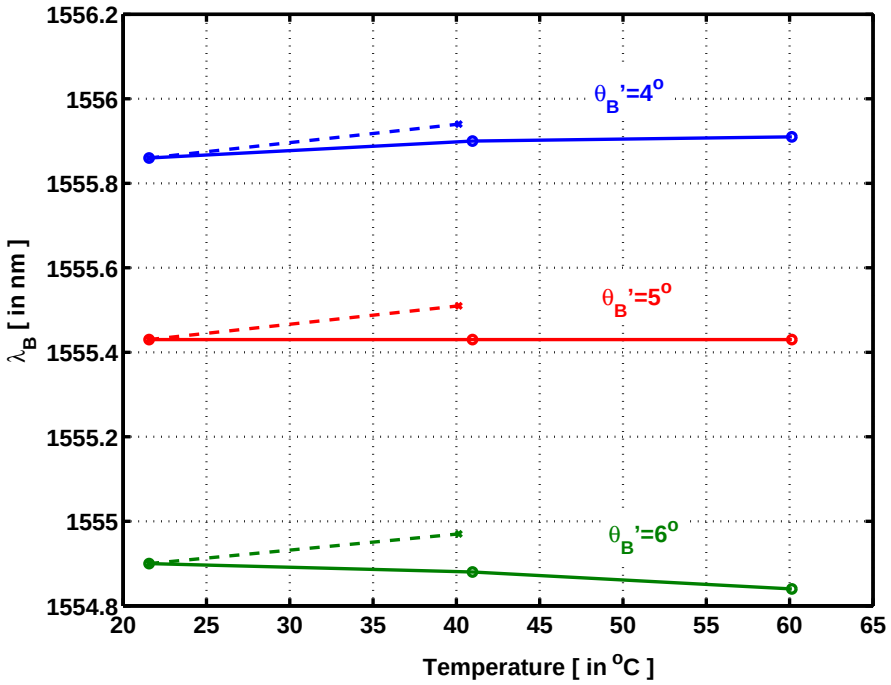

Figure 4.6: The Bragg wavelengths measured with the athermal design for three different incident angles versus temperature.

Without the athermal mechanism, the Bragg wavelength would drift about 0.16 nm (20 GHz) from 21°C to 60°C. The Bragg wavelengths for $\theta'_B = 4°$ are seen to increase with the rising temperature despite the counteracting MEMS operation although they do not increase quite as much as when there is no compensation mechanism; on the other hand, the Bragg wavelengths for $\theta'_B = 6°$ are decreasing with the rising temperature obviously because they are overcompensated by the MEMS mirror deflection. The athermal WDM filter design employing the MEMS mirror keeps the Bragg wavelength constant; however, to couple the reflected or transmitted beam back into a fiber, another counteracting MEMS mirror must be used to undo the beam walk-off.

Since many thermally actuated MEMS devices consist of materials that possess different mechanical properties, they can suffer from hysteresis. The Bragg wavelength of the athermal filter system undergoes a 0.09 nm (11.25 GHz) decrease after we cool it back down to room temperature. A possible solution to this problem is to anneal the MEMS device at an elevated temperature (about 300°C) before use. The drift in the Bragg wavelength due to hysteresis was experimentally shown to reduce to 0.01 nm (1.25 GHz) after annealing.

4.4 Conclusions

We have shown that the temperature dependence of the Bragg wavelength of a holographic filter can be compensated by incorporating a passive, thermally actuated MEMS mirror into the system. The packaging should be such that the mirror and the filter thermally track each other. To improve the performance of the athermal filter design, its vital to gain a deeper understanding of the evolution of filter shapes away from normal incidence. Other topics such as beam walk-off, polarization dependent loss (PDL) and the elimination of mirror hysteresis are also important considerations in practical applications.

Bibliography

[1] G. A. Rakuljic and V. Leyva. Volume holographic narrow-band optical filter. *Optics Letters*, 18:459–461, March 1993.

[2] S. Breer and K. Buse. Wavelength demultiplexing with volume phase holograms in photorefractive lithium niobate. *Applied Physics B*, 66:339–345, March 1998.

[3] D. Psaltis. Coherent optical information systems. *Science*, 298:1359–1363, November 2002.

[4] H. Takashashi. Temperature stability of thin-film narrow-bandpass filters produced by ion-assisted deposition. *Applied Optics*, 34:667–675, February 1995.

[5] N. Keil, H. H. Yao, and C. Zawadzki. Athermal polarization-independent array-waveguide grating (AWG) multiplexer using an all-polymer approach. *Applied Physics B*, 73:619–622, November 2001.

[6] Y. L. Lo and C. P. Kuo. Packaging a fiber Bragg grating without preloading in a simple athermal bimaterial device. *IEEE Transactions on Advanced Packaging*, 25:50–53, February 2002.

[7] R. T. Smith and F. S. Welsh. Temperature dependence of elastic, piezoelectric, and dielectric constants of lithium tantalite and lithium niobate. *Journal of Applied Optics*, 42:2219–2230, May 1971.

[8] U. Schlarb and K. Betzler. Refractive indices of lithium niobate as a function of temperature, wavelength and compositions-a generalized fit. *Physical Review B*, 48:15613–15620, December 1993.

[9] W. H. Chu, M. Mehregany, and R. L. Mullen. Analysis of tip deflection and force of a bimetalic cantilever microactuator. *Journal of Micromechanics and Microengineering*, 343:4–7, February 1993.

[10] D. L. Staebler and J. J. Amodei. Thermally fixed holograms in $LiNbO_3$. *Ferroelectrics*, 343:107–113, 1972.

Chapter 5

Holographic filters in the 90 degree geometry

Holograms in the 90 degree geometry have been theoretically treated before for the Bragg-matched case, but little has been done experimentally to corroborate the analytical results. In this chapter, we adopt coupled-mode equations to analyze such holograms in the presence of wavelength detuning. Then we numerically simulate the field distribution and diffraction efficiency for both the Bragg-matched and Bragg-mismatch cases, taking advantage of the characteristic spatial causality inherent in this geometry. Experimental results of beam profiles and filtering properties will also be presented and compared with the theoretical predictions.

5.1 Introduction

Holography has found widespread applications in modern optics. High-density data storage has been demonstrated in transmission, 90 degree and reflection geometry holography with numerous multiplexing schemes[1]. Over the last couple of decades, holography has also proved itself to be a promising candidate for WDM filters, mainly in the reflection geometry[2, 3]. However, the beam profiles and filtering properties of holograms in the 90 degree geometry remain relatively unexplored[4]. In this chapter, we will present some experimental results for the 90-degree-geometry holography as well as numerical simulations based on coupled mode analysis.

This chapter is organized as follows. In section 2 we define a hologram of interest in the 90 degree geometry and summarize theoretical predictions by Kenan[5] in the Bragg-matched condition. In section 3 we take a step farther and derive the coupled mode equations in the presence of wavelength mismatch, therefore laying the foundation for numerical simulation, the results of which will then be subsequently presented in section 4. Section 5 will be devoted to showing some of the relevant experimental results and comparing them with the theoretical and numerical analyses. In section 6, we draw our conclusion as to the possible applications of the 90-degree-geometry holograms in

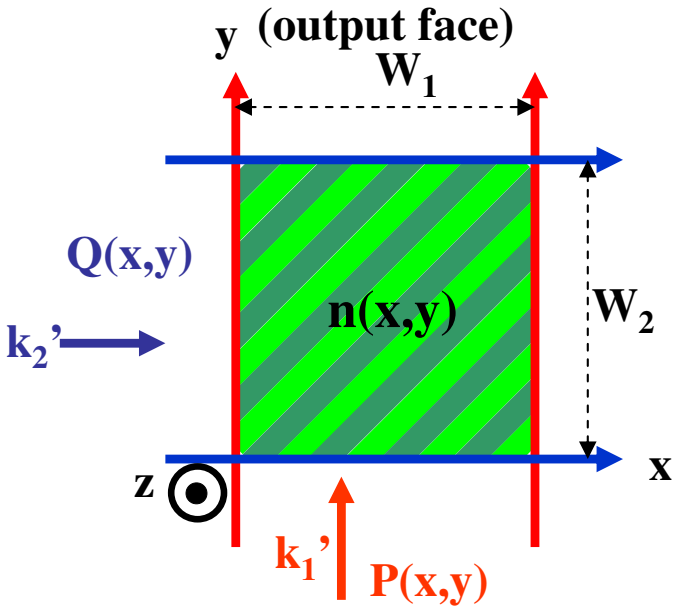

Figure 5.1: A schematic graph of a grating in the 90 degree geometry.

WDM filter design.

5.2 Beam propagation in the 90 degree geometry holograms

A grating in the 90 degree geometry is shown in Fig. 5.1. It is formed by interfering two coherent beams inside a piece of photorefractive material ($LiNbO_3$, for example) whose refractive index is therefore periodically modulated. Assume that the two beams used to generate the grating are polarized perpendicular to the xy plane and have the following field profiles:

$$E_1(\mathbf{r}) = E_{10}\exp(-j\mathbf{k_1}\cdot\mathbf{r}), \tag{5.1}$$

$$E_2(\mathbf{r}) = E_{20}\exp(-j\mathbf{k_2}\cdot\mathbf{r}), \tag{5.2}$$

where E_{10} and E_{20} are the amplitudes of the plane wavefronts and $\mathbf{k_1} = (k/2, -k/2, k_z)$, $\mathbf{k_2} = (-k/2, k/2, k_z)$. Furthermore, k and k_z are related to the recording wavelength λ_{rec} by the following equation:

$$|\mathbf{k_1}| = |\mathbf{k_2}| = \frac{2\pi n_{rec}}{\lambda_{rec}} = \sqrt{\frac{k^2}{2} + k_z^2}, \tag{5.3}$$

where n_{rec} stands for the bulk refractive index of the medium at the recording wavelength λ_{rec}. The two beams interfere with each other throughout the crystal and create a grating of constant index

modulation Δn on each plane defined by a constant z:

$$n(x,y) = n_0 + \Delta n \cos k(x-y). \tag{5.4}$$

The bulk index of the medium n_0 and the index modulation Δn are constants whose values will be determined by the readout wavelength λ_0'. We will assume $\Delta n \ll n_0$, as is usually the case. Now say we have an incident beam (assumed to be polarized along the z-axis) with a beam profile $Q(x,y)$ and wave vector $\mathbf{k_2'} = k'\mathbf{a_x}$ (here $\mathbf{a_x}$ is the unit vector along the x-axis and $k' = 2\pi n_0 \lambda_0' = k_0' n_0$, where λ_0' is the incident wavelength in vacuum) as in Fig. 5.1. If $k' \approx k$, the total field distribution inside the grating region that thus ensues can be cast into the form:

$$E(x,y) = P(x,y)\exp(-j\mathbf{k_1'}\cdot\mathbf{r}) + Q(x,y)\exp(-j\mathbf{k_2'}\cdot\mathbf{r}), \tag{5.5}$$

conceivably, $k_1' = k'\mathbf{a_y} \approx k\mathbf{a_y}$ and $P(x,y)$ is the diffracted field distribution. Kenan has detailed the Bragg-matched case (i.e., $k' = k = 2\pi n_0/\lambda_0$, where λ_0 is the Bragg wavelength) in his paper[5], and we repeat his analytical results below:

$$\begin{aligned} Q(x,y) &= Q_0 J_0(2\kappa\sqrt{xy}) - jP_0\sqrt{\frac{x}{y}}J_1(2\kappa\sqrt{xy}), \\ P(x,y) &= P_0 J_0(2\kappa\sqrt{xy}) - jQ_0\sqrt{\frac{y}{x}}J_1(2\kappa\sqrt{xy}), \end{aligned} \tag{5.6}$$

where $\kappa = \pi\Delta n/\lambda_0$. We therefore realize that for the Bragg-matched case, the incident and diffracted beam profiles within the uniform grating region can be described analytically by the zeroth- and first-order Bessel functions of the first kind. What Kenan did not consider in his paper, however, are the cases where we have a Bragg-mismatch component either due to a wavelength detuning or an angular deviation.

In the 90 degree geometry, the diffracted beam is nonuniform for a constant refractive index modulation and a uniform incident beam. As a result, the diffraction efficiency is defined as the total power ratio of the incident and diffracted beams[6]. We have from Eq. (5.6):

$$\eta = 1 - J_0^2(2\kappa\sqrt{W_1 W_2}) - J_1^2(2\kappa\sqrt{W_1 W_2}). \tag{5.7}$$

It is worth pointing out that the diffraction efficiency η is a non-decreasing function that has zero derivatives only at zeros of the Bessel function of the first kind, order 1.

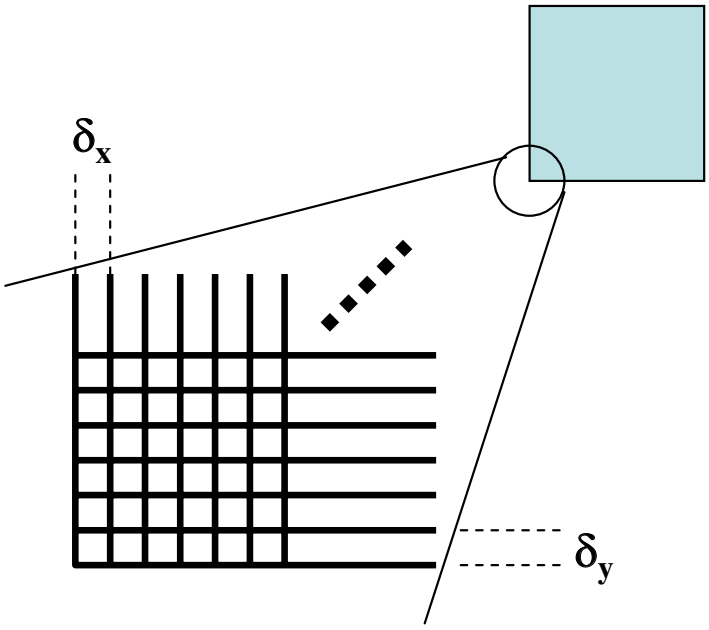

Figure 5.2: The grating region has been divided into tiny rectangular regions to facilitate numerical simulation.

5.3 Wavelength selectivity

Now we consider the case where the incident wavelength λ_0' is different from the Bragg wavelength λ_0 assuming the absence of angular detuning for simplicity, i.e., $\mathbf{k_1'}//\mathbf{a_y}$, $\mathbf{k_2'}//\mathbf{a_x}$ and $\mathbf{k_1'} = \mathbf{k_2'} \neq k$. We also assume that the difference between λ_0 and λ_0' is small enough that the material dispersion is negligible. Substituting Eq. (5.5) into the Helmholtz equation we get:

$$[\frac{\partial^2}{\partial x^2}P + \frac{\partial^2}{\partial y^2}P - 2jk'\frac{\partial}{\partial y}P - k'^2P]\exp(-jk'y) + [\frac{\partial^2}{\partial x^2}Q + \frac{\partial^2}{\partial y^2}Q - 2jk'\frac{\partial}{\partial x}Q - k'^2Q]\exp(-jk'x)$$
$$+k_0'^2[n_0^2 + 2n_0\Delta n\cos k(x-y)][P\exp(-jk'y) + Q\exp(-jk'x)] = 0. \quad (5.8)$$

We have neglected the term involving Δn^2 because it is minute compared with terms associated with n_0^2 and $n_0\Delta n$; we further adopt the parabolic approximation that entitles us to ignore the second order partial differential terms. After some straightforward algebraic manipulations, we end up with

$$\begin{aligned} \frac{\partial Q}{\partial x} + j\kappa' P\exp\left[j(k'-k)(x-y)\right] &= 0, \\ \frac{\partial P}{\partial y} + j\kappa' Q\exp\left[j(k-k')(x-y)\right] &= 0, \end{aligned} \quad (5.9)$$

where $\kappa' = \pi\Delta n/\lambda_0'$. To get back the Bragg-matched case, we can simply set $k' = k$. Although the analytical solution to Eq. (5.9) is not available, we can numerically simulate the Bragg-mismatch case and still get the desired beam profiles and diffraction efficiency, which will be presented shortly.

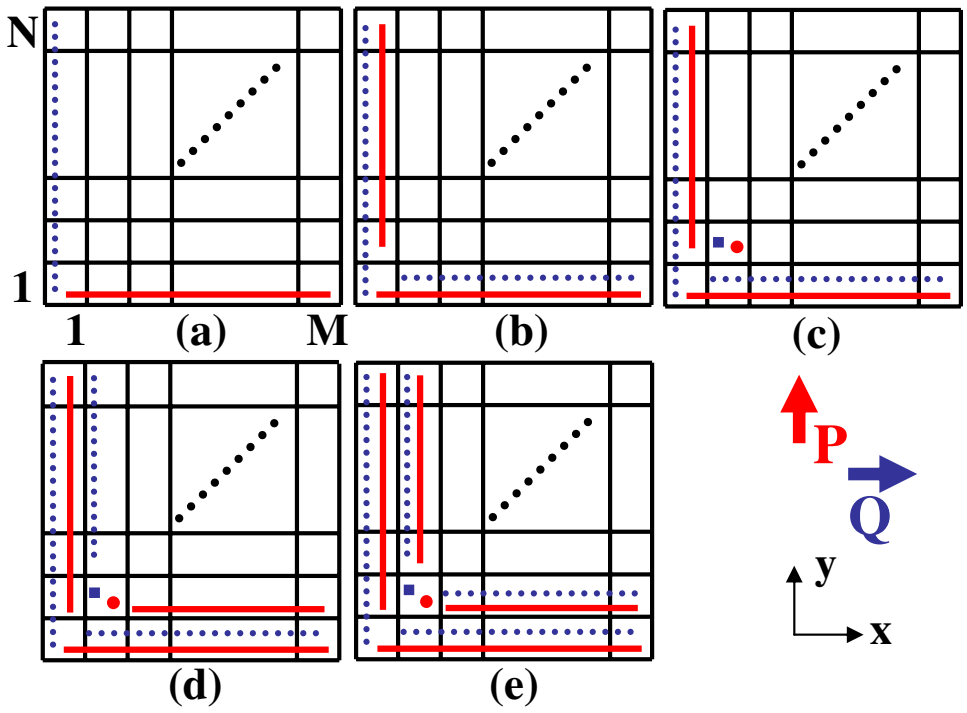

Figure 5.3: Working principle of the numerical simulation. The inherent causality of gratings in the 90 degree geometry facilitates the algorithm.

5.4 Numerical simulations

In this section we shall simulate for the wavelength detuning case. We start by discretizing Eq. (5.9):

$$\begin{cases} \frac{Q(x+\delta_x,y)-Q(x,y)}{\delta_x} + j\kappa' P(x,y)\exp\left[j(k'-k)(x-y)\right] &= 0, \\ \frac{P(x,y+\delta_y)-P(x,y)}{\delta_x} + j\kappa' Q(x,y)\exp\left[-j(k'-k)(x-y)\right] &= 0, \end{cases}$$

which can be further simplified to

$$\begin{aligned} Q(x+\delta_x,y) &= Q(x,y) - j\delta_x\kappa' P(x,y)\exp\left[j(k'-k)(x-y)\right], \\ P(x,y+\delta_y) &= P(x,y) - j\delta_y\kappa' Q(x,y)\exp\left[-j(k'-k)(x-y)\right]. \end{aligned} \tag{5.10}$$

Eq. (5.10) implies that if we divide the grating region into tiny rectangular cells with dimension $\delta_x \times \delta_y$ as shown in Fig. 5.2 and happen to know the values of both $P(x,y)$ and $Q(x,y)$ in a certain cell, we can calculate both the value of $P(x,y+\delta_y)$ in the next cell along the y-direction and the value of $Q(x+\delta_x,y)$ in the next cell along the x-direction. In our simulations, the incident beam is uniform over the input face defined by $x=0$, $0 \le y \le W_2$, and no diffracted beam is present at the face defined by $y=0$, $0 \le x \le W_1$; therefore we have the following boundary conditions:

1. $Q(0, 0 \leq y \leq W_2) = Q_0$.

2. $P(0 \leq x \leq W_1) = 0$.

Refer to the five plots in Fig. 5.3. The grating has been divided into $M \times N$ cells (say, $\delta_x = W_1/M$, $\delta_y = W_2/N$). In Fig. 5.3(a), we put in the boundary conditions specified above. A red solid (blue dotted) line or red dot (blue square) in a cell denotes that the value of $P(x, y)$ ($Q(x, y)$) within that cell is known to us. Using Eq. (5.10), we can go on and figure out all the $P(Q)$ values in the first column (row), which is illustrated in Fig. 5.3(b). We then continue to obtain the value of $P(Q)$ in the cell (2,2) and afterwards all the values in the cells belonging to the second row and column as shown in Figs. 5.3(c) and (d); if we stick to this algorithm, well get all the values inside the grating region. Obviously, the smaller the cell size is, the more details of the beam profiles we can grasp. This method works extremely well in the 90 degree geometry holograms due to the inherent causality in the geometry: the field value in a cell can only be affected by field values in the cells that are lower or to the left. On the other hand, holograms in the reflection geometry do not possess this property because multiple reflections will inevitably destroy such causality. Before presenting some simulated results, the parameters adopted in our simulations are as follows:

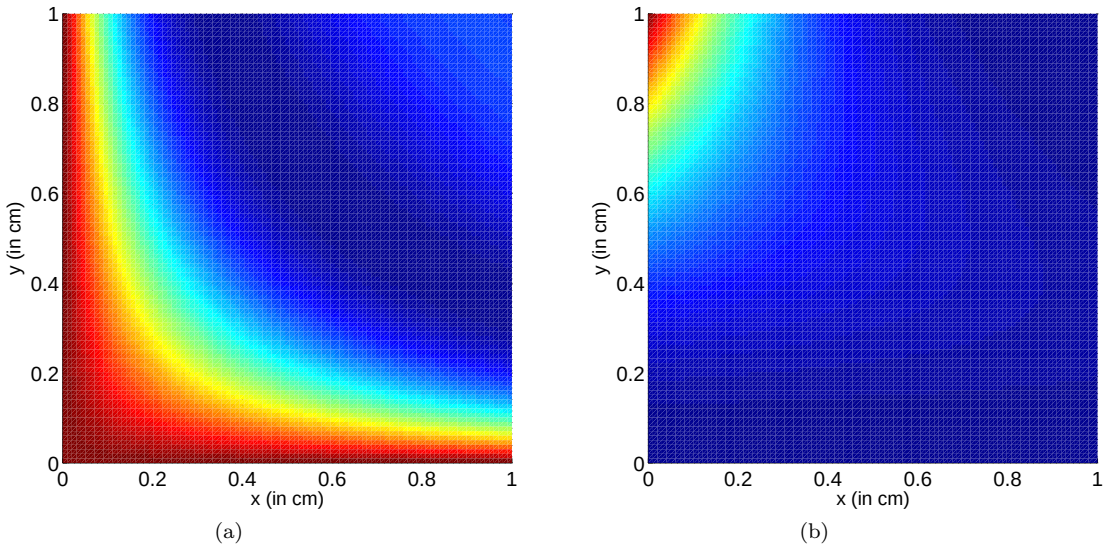

Figure 5.4: Simulated incident (a) and diffracted (b) beam profiles for the Bragg-matched case.

- $W_1 = W_2 = 10^{-2}$ m.
- $M = N = 100$, which implies $\delta x = \delta y = 10^{-4}$ m.
- The index modulation $\Delta n = 1 \times 10^{-4}$.
- The Bragg wavelength λ_B of the grating is 1550 nm.

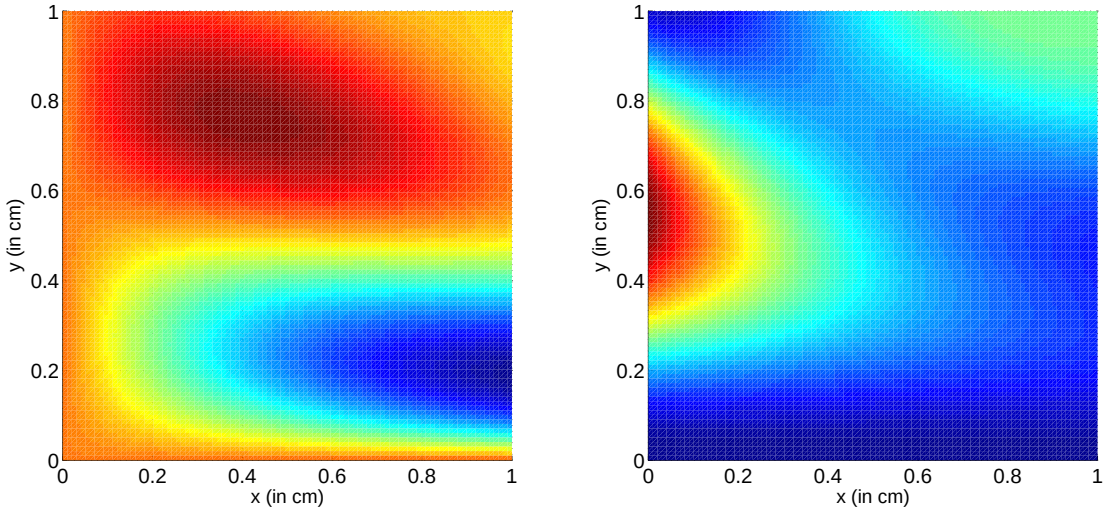

Figure 5.5: Simulated incident (a) and diffracted (b) beam profiles for the Bragg mismatch case.

We numerically simulate the beam profiles in Fig. 5.1 using Eq. (5.10) for the Bragg-matched case where Δn is constant and the incident beam is uniform over the input face. The beam profiles at Bragg wavelength are shown in Fig. 5.4. We can see that the field distribution of the incident beam is symmetric with respect to the line $x = y$, which is consistent with the analytical prediction; furthermore, the grating directs most of the incident beam towards the output face, and the diffracted beam has a tendency to concentrate as close to the input face as possible. The stronger the grating is, the more obvious the phenomenon will be. A uniform incident beam will invariably result in a nonuniform diffracted beam profile. In light of Eq. (5.6), the diffracted beam profile at the output face can be described by the Bessel function of the first kind. The diffracted beam intensity profile at the crystal output face obtained from the numerical simulation is indistinguishable from the analytical expression.

Being confident that our numerical method does produce results confirmed by the analytical solution, we go on and simulate the diffracted beam profile in the Bragg-mismatch case for a uniform incident beam, the result of which is plotted in Fig. 5.5 for a wavelength mismatch $\Delta\lambda = \lambda_0 - \lambda_0' = 0.1$ nm, other parameters are the same as those adopted in Fig. 5.4. We notice that the beam deflection ability is weaker for this (Bragg-mismatch) case, and less incident light manages to make its way to the output face.

Plotted for comparison in Fig. 5.6 is the normalized diffracted beam intensity along the output face; they have been normalized to the peak diffracted intensity of the Bragg-matched case.

To visualize the magnitude response of a given grating, we run the program for different wavelengths of interest and then calculate the diffraction efficiency for each wavelength. For wavelengths other than the Bragg wavelength a mismatch phase factor has to be included in the simulation. To

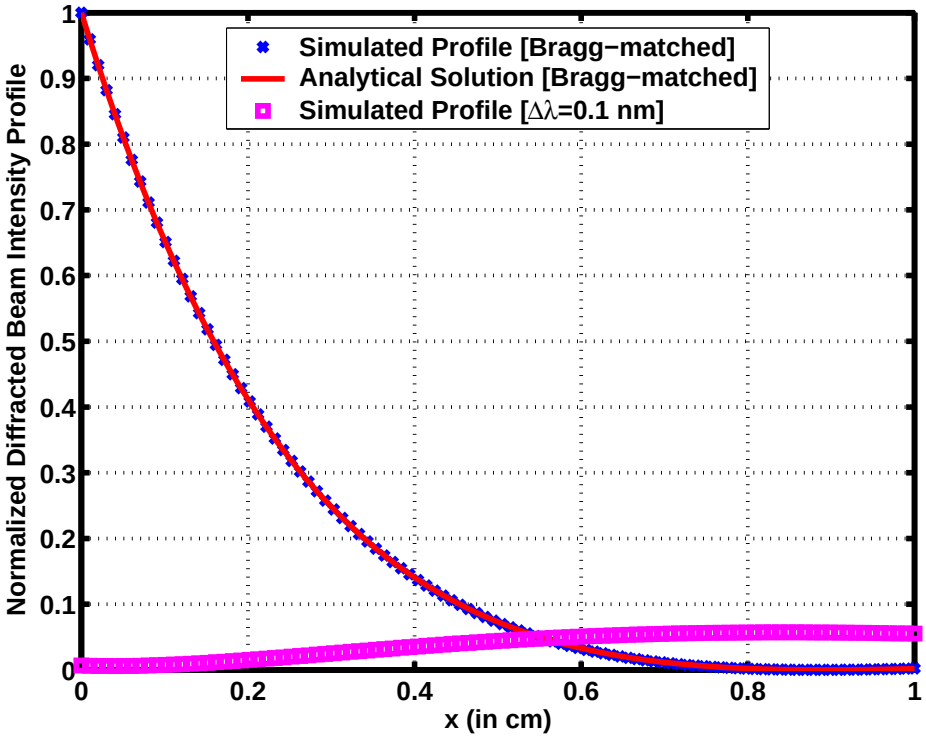

Figure 5.6: Normalized diffracted beam intensity profiles for the Bragg-matched (traced out by crosses) and Bragg-mismatch cases (denoted by squares). The solid curve is plotted according to the analytical solution of the Bragg-matched case Eq. (5.6), which fits excellently with our numerical prediction.

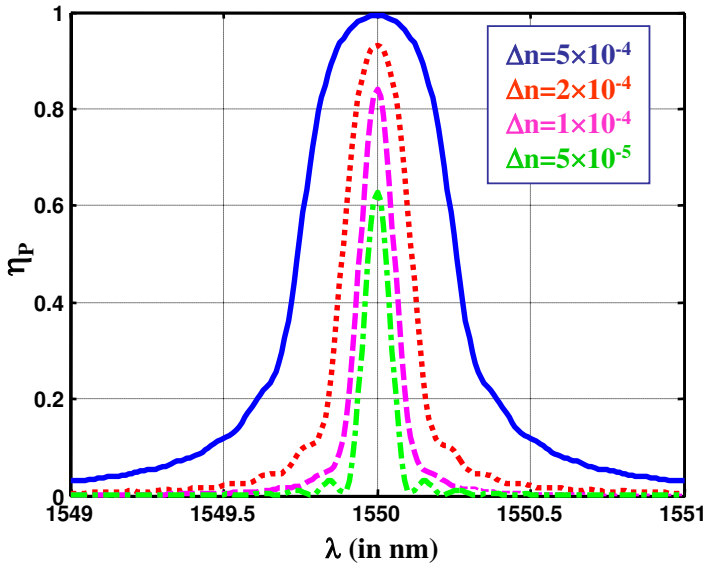

Figure 5.7: Simulated magnitude response of 90 degree geometry gratings for various index modulation Δn.

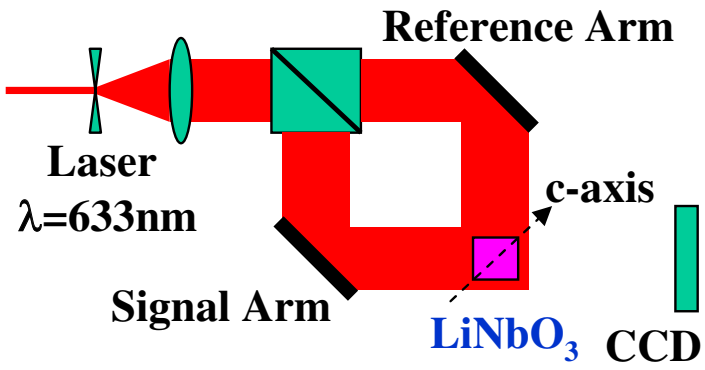

Figure 5.8: Experimental setup for monitoring the diffracted beam profile.

compare the magnitude responses of different values of refractive index modulation, we carry out the simulation for $\Delta n = 5 \times 10^{-4}$, 2×10^{-4}, 1×10^{-4}, 5×10^{-5}. The rest of the parameters remain the same as those in Fig. 5.4. The results are shown in Fig. 5.7. We can see clearly that as we increase the index modulation Δn, the bandwidth of the magnitude response will broaden, and the peak diffraction efficiency goes up.

5.5 Experimental results

5.5.1 Beam profile experiment

The experimental setup used to explore the temporal evolution of the diffracted beam profile is shown in Fig. 5.8. A laser beam is first split into two (for future reference, we call one of them the reference beam, the other signal beam) and then recombined to imprint the interference pattern inside our photorefractive crystal. Cerium (Ce) doped $LiNbO_3$ is used because of its sensitivity to 632 nm radiation. Both of the beams cover the entire crystal. Each beam has an intensity of 1.35 mW/cm^2 in the beam center, which is the part used to record the grating. After passing through the crystal, the intensity drops to 0.543 mW/cm^2. We monitor the diffracted beam profile every 15 minutes by blocking the signal arm and grabbing the image formed on the CCD camera. The total recording time is 5 hours, therefore we obtain 20 frames depicting the temporal evolution of the diffracted beam. Since the diffracted beam profile is highly nonuniform, a measure of diffraction efficiency should be defined. In our experiment, the diffraction efficiency is calculated as the ratio of the average diffracted intensity to the reference beam intensity attenuated by the crystal without hologram.

Four of the frames taken are shown in Fig. 5.9. Each of them describes a two-dimensional intensity distribution corresponding to the diffracted beam profile at the output crystal surface. (Refer to Fig. 5.10.) We can see that as time goes by, not only does the average diffracted intensity increase,

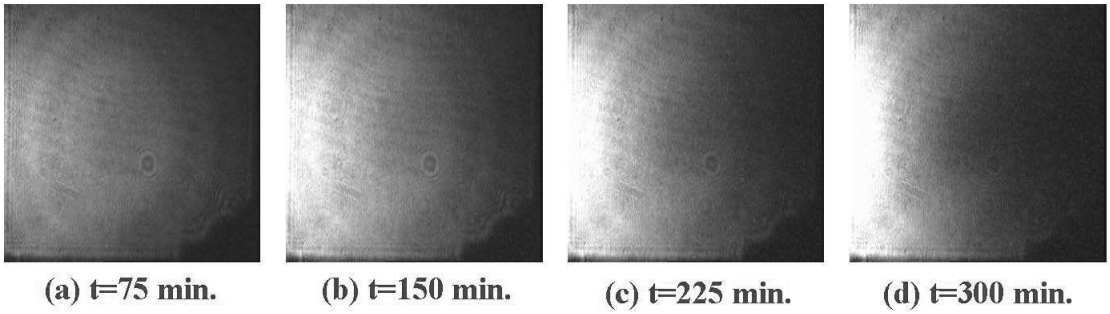

Figure 5.9: Temporal evolution of the diffracted beam profile formed on the CCD camera.

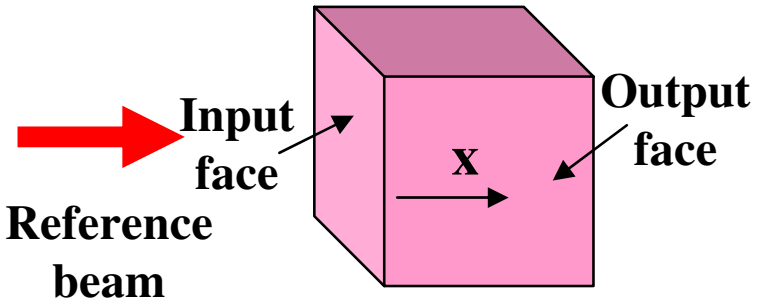

Figure 5.10: The variable x is used in Eq. (5.11) for the calculation of diffracted beam profiles.

but more light is also squeezed toward the input surface. These phenomena can be explained if we write down the analytical solution of the diffracted beam intensity profile at the output surface according to Eq. (5.6):

$$I_P(x) = I_{Q0} W \frac{J_1^2(2\kappa\sqrt{Wx})}{x}, \tag{5.11}$$

where $\kappa = \pi\Delta n/\lambda_0'$ is the coupling constant and the variable x represents the distance along the output face measured from the input plane, as shown in Fig. 5.10. W is the dimension of the crystal, which is 1 cm in our case. To illustrate the squeezing effect brought about by the buildup of index modulation, we plot the theoretical $I_P(x)/I_P(0)$ for three different coupling constants in Fig. 5.11. It is obvious that as Δn increases, the relative intensity of the diffracted beam close to the input face will also increase.

To explain the increasing trend of overall diffraction efficiency η, we remember that the analytical solution for the diffraction efficiency is (from Eq. (5.7), substitute W for W_1 and W_2):

$$\eta = 1 - J_0^2(2\kappa W) - J_1^2(2\kappa W). \tag{5.12}$$

Eq. (5.12) is seen to be a monotonically non-decreasing function of κ ($\partial\eta/\partial\kappa \geq 0$). Therefore, we

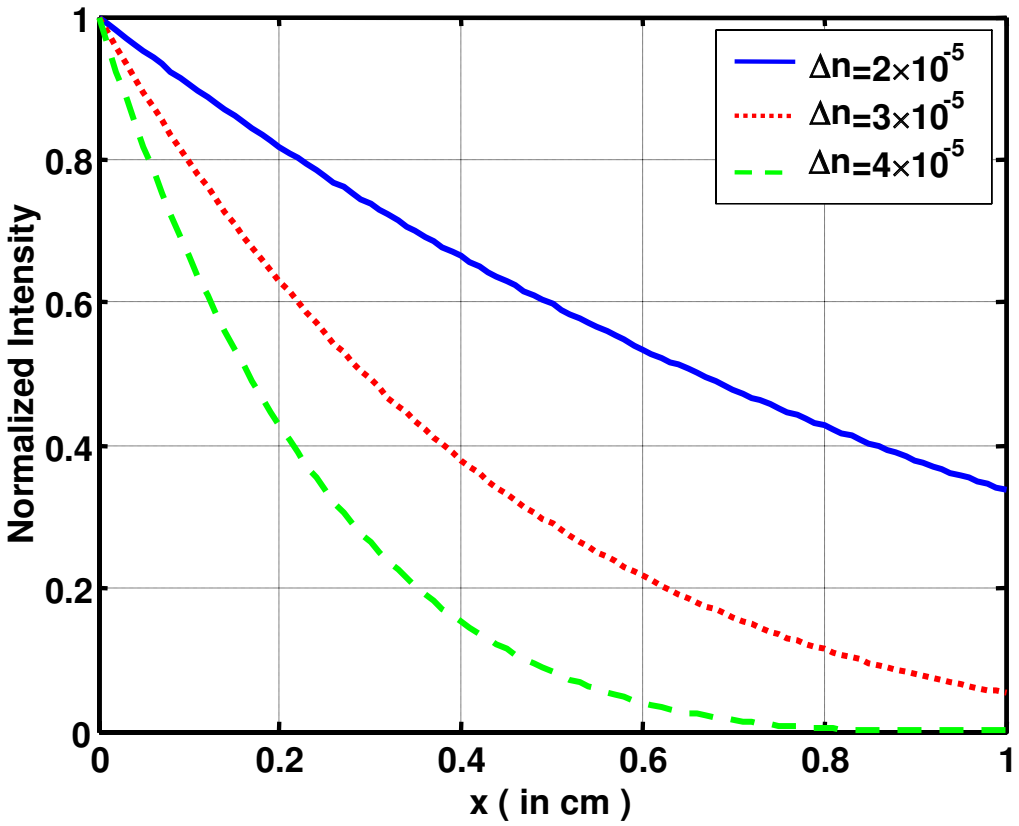

Figure 5.11: Theoretical plot of the normalized beam profile for different values of index modulation.

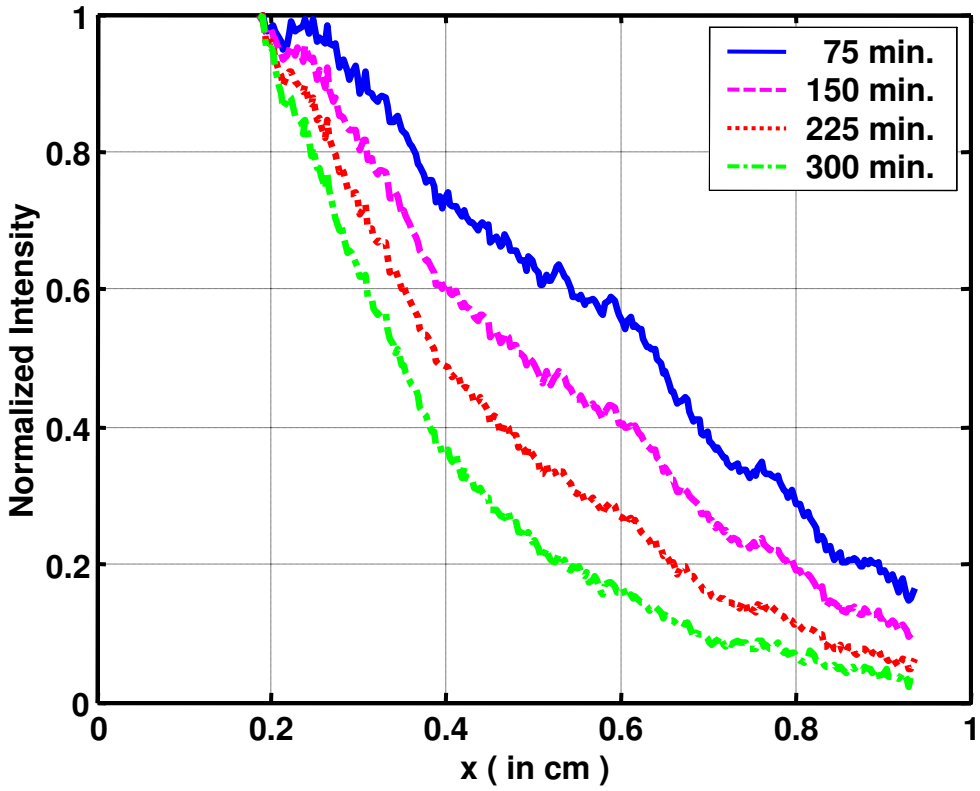

Figure 5.12: Averaged diffracted beam profile at different temporal points. (Experimental)

will definitely get more diffracted light over time as Δn goes up. At the end of our 5-hour recording session, the average diffracted beam intensity is 0.427 mW/cm^2, accounting for a diffraction efficiency of 80.57%, and this corresponds to an index modulation of 2.89×10^{-5}.

We can also estimate the index modulation Δn by fitting the beam profile captured by the CCD camera to Eq. (5.12). Care, however, must be exercised when we perform the curve fit. First, a dark frame should be taken on the CCD as the background frame, which will be subsequently subtracted from other frames taken later. Then parts of the images may have to be discarded in order to get rid of the funny beam structures caused by the crystal edges and CCD saturation, if any. The averaged diffracted beam profiles are shown in Fig. 5.12. These profiles are derived from the data in Fig. 5.9, and the first 1.875 mm and the last 0.625 mm are cut off to discard the saturated CCD image parts and edge effects. The temporal behavior of the diffracted profile does follow the prediction of Eq. (5.12). A fit according to the equation is then performed to extract the index modulation information from the 30 frames taken over a time duration of 5 hours, which is plotted in Fig. 5.13. The index modulation Δn at $t = 5$ hrs is estimated to be $\Delta n = 3.69 \times 10^{-5}$, which is larger than $\Delta n = 2.89 \times 10^{-5}$ deduced from the diffraction efficiency. This could be due to the clipping of the beam profiles when we process them prior to the fitting. The processed beam profiles are relatively

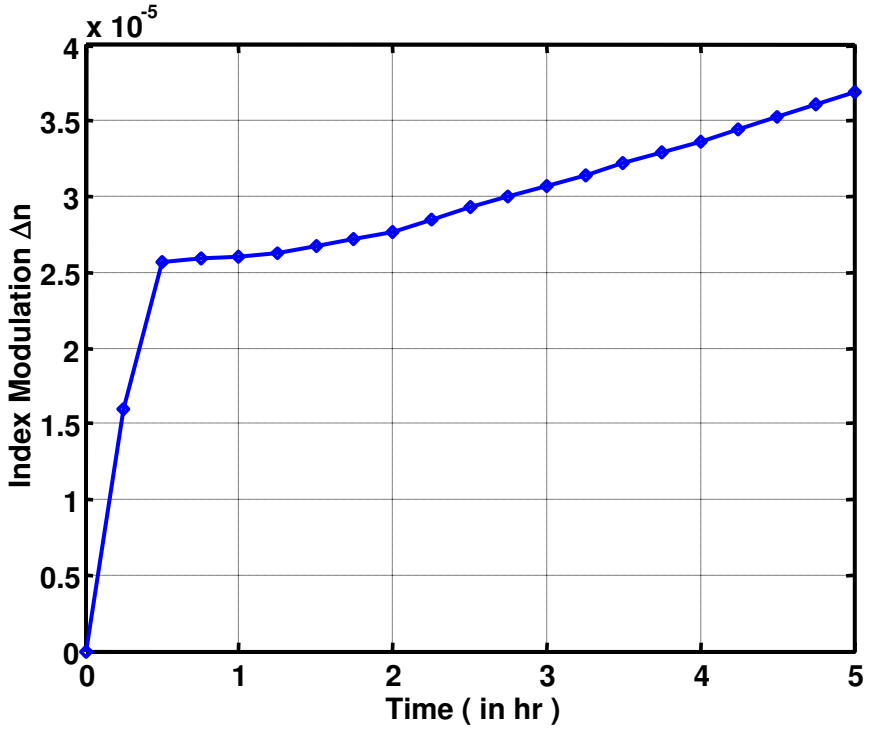

Figure 5.13: Temporal evolution of index modulation Δn derived by fitting the diffracted beam profile to Eq. (5.12).

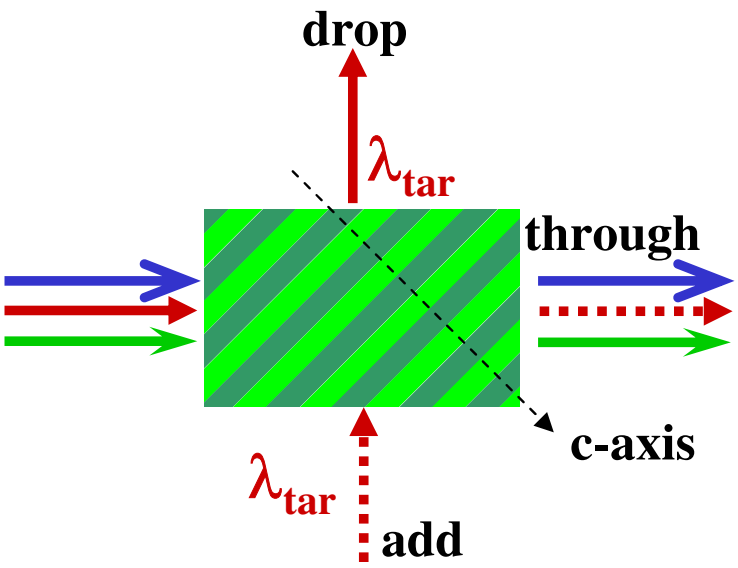

Figure 5.14: Implementation of a holographic add-drop filter in the 90 degree geometry.

free from imperfections such as the edge effects. Moreover, the grating seems to build up very fast during the first 30 minutes of recording.

5.5.2 Filtering properties of the 90 degree geometry holograms

Holographic filters in the 90 degree geometry are special because they separate the through and drop channels naturally; in the reflection geometry, such a separation will have to be achieved by slightly tilting the beam or by using a circulator. This property renders the add-drop operation easier in the 90 degree geometry. Except for this, the idea of a 90 degree geometry holographic filter is not too different from that in the reflection geometry: both of them target the Bragg wavelength determined by the grating period and separate it from other frequency components. The principle of operation of a holographic filter in the 90 degree geometry is shown in Fig. 5.14. Such a filter is generated by interfering two coherent beams onto the surface of a photosensative material. The angle between the recording beams will determine the Bragg wavelength in the 90 degree geometry through the following equation:

$$\theta = \arcsin\left(\frac{n_{tar}\lambda_{rec}}{\sqrt{2}\lambda_{tar}}\right), \tag{5.13}$$

where λ_{rec}, λ_{tar} and n_{tar} are the recording wavelength, target wavelength and the refractive index of the material at the target wavelength. In our experiment, $\lambda_{tar} = 1556$ nm, $\lambda_{rec} = 488$ nm and the refractive index of the material ($LiNbO_3$) at λ_{tar} is $n_{tar} = 2.2113$ for an ordinarily polarized readout beam; therefore the external angle for recording should be $\theta = 29.37°$. We record the holographic filter in the transmission geometry with beams of intensity 15 mW/cm^2 each for 2

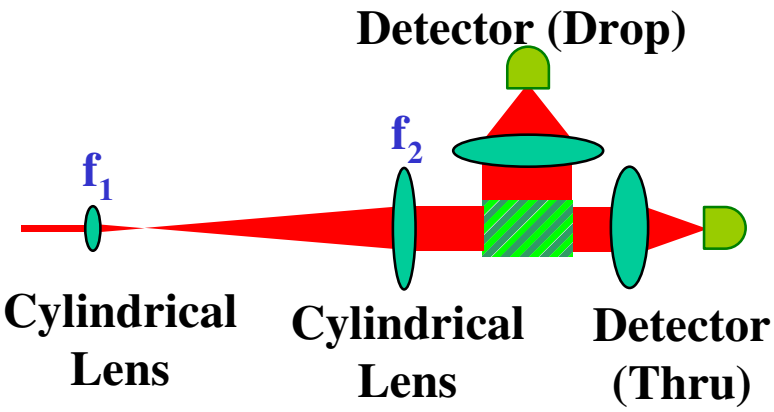

Figure 5.15: Experimental setup for testing the 90 degree holographic filter.

hours. The crystal specifications are as follows:

- Crystal dimension: $LiNbO_3$ 2 cm by 1.5 cm by 0.5 cm with c-axis parallel to the 2 cm by 1.5 cm face at 45 degrees to the edges.
- Doping level: 0.05 wt% Fe doping.
- Oxidation states: $C_{Fe^{2+}} = 1.26 \times 10^{18}\ cm^{-3}$.

The setup for measuring the diffraction efficiency of such a filter is shown in Fig. 5.15. The output from a tunable laser source (1520 nm to 1600 nm) is first expanded in one dimension by the combination of two cylindrical lenses (f_1 = -3 cm, f_2 = 25 cm) and then passed through the holographic filter. The output of the laser has a beam diameter of 0.5 mm, carrying a power of 1.5 mW (or 1.76 dBm). After widening, the beam dimension will be approximately 4 mm by 0.5 mm. Another lens is placed behind the crystal to collect the transmitted light onto a detector for the purpose of measurement. The filter response in the through channel is plotted in Fig. 5.16. The Bragg wavelength is 1556.44 nm with a diffraction efficiency close to 58%. To explain why we expand the beam, we refer to the analytical expression of the diffraction efficiency in Eq. (5.7). W_1 is the beam width, and W_2 is the crystal dimension parallel to the propagation direction of the input beam. In our case, W_1 = 4 mm and W_2 = 15 mm, from which an index modulation of 6.05×10^{-15} can be inferred. Without the beam expansion, the diffraction efficiency is a smaller 10.5% and harder to measure. Sometimes a small dip may even be masked by the background fluctuation and be practically invisible to the observer. By inspection of Eq. (5.7), to increase the diffraction efficiency of the 90 degree geometry filter, we have to increase either the dimensions of the crystal (and therefore the width of the incident beam) or the index modulation Δn.

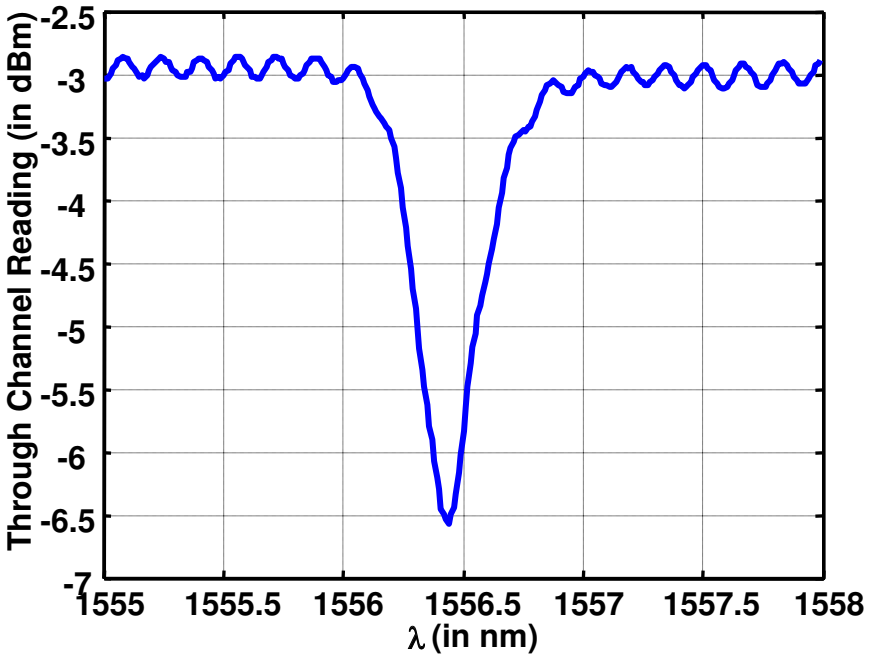

Figure 5.16: Experimental filter response measured in the filter through (transmission) channel. (This corresponds to an index modulation of $\Delta n = 6 \times 10^{-5}$.)

5.6 Conclusion

Experiments on beam profiles in the 90 degree geometry holography corroborate the theoretical predictions and give us a clear idea of how an incident beam interacts with the grating. The selective behavior demonstrated in the frequency response is certainly reminiscent of holographic filters. Holographic filters in the 90 degree geometry have the advantage of naturally separating the diffracted frequency components from the transmitted ones. Nevertheless, deliberation on the filter geometry also reveals the fact that strong dispersion will be introduced for the diffracted wavelength components. Such a property is generally undesirable in WDM filters, but it may be valuable in applications regarding dispersion compensation.

Bibliography

[1] M. H. Yukselici, R. Ince, and A. T. Ince. Data storage characteristics of iron doped $LiNbO_3$ under a 90 degrees geometry two-beam coupling configuration. *Optics and Lasers in Engineering*, 42:277–287, September 2004.

[2] G. A. Rakuljic and V. Leyva. Volume holographic narrow-band optical filter. *Optics Letters*, 18:459–461, March 1993.

[3] S. Breer and K. Buse. Wavelength demultiplexing with volume phase holograms in photorefractive lithium niobate. *Applied Physics B*, 66:339–345, March 1998.

[4] Y. Yang, A. Adibi, and D. Psaltis. Comparison of transmission and the 90-degree holographic recording geometry. *Applied Optics*, 42(17):3418–3427, June 2003.

[5] R. P. Kenan. Theory of crossed-beam diffraction gratings. *IEEE Journal of Quantum Electronics*, 14:924–930, December 1978.

[6] L. Solymar and D. J. Cooke. *Volume Holography and Volume Gratings*. Academic Press, New York, 1981.

Chapter 6

Femtosecond holography in Kerr media

The femtosecond holographic pump-probe technique is useful for investigating ultrafast material phenomena. We demonstrate, in theory and experiment, that the temporal resolution in such configurations does not degrade appreciably despite increasing angular separation between the pump pulses. Transient Kerr gratings are generated inside calcium fluoride (CaF_2) crystals by two interfering femtosecond (pump) pulses at 388 nm and read out by a Bragg-matched probe pulse at 776 nm. The solution to the coupled mode equations of pulse holography is well corroborated by the experimental results, yielding a value of Kerr coefficient 4.4×10^{-7} cm^2/GW for CaF_2.

6.1 Introduction

Femtosecond pump-probe techniques have become a very powerful tool for investigating various ultrafast phenomena in materials. They proved fruitful in many research areas, e.g., characterization of carrier dynamics in semiconductors[1, 2], parametric up-conversion processes[3], femtosecond spectroscopy[4] and nondestructive examination of materials[5], just to name a few.

In a holographic pump-probe experiment, two intense, identical pump pulses overlap temporally and spatially in a nonlinear medium to induce (by interference) periodically modulated material responses within the region of intersection. A probe pulse then experiences the ensuing optical perturbations and gets diffracted when the Bragg condition is met. The diffracted probe pulse is picked up by a detector; the detected signal as a function of the time delay between the pump and probe pulses is then mapped out and gives information about the involved ultrafast mechanisms of interest.

The coupled mode equations of femtosecond holography are different from those of continuous-wave holography[6]. In this article, the coupled mode equations for pulse holography are solved in the case of Kerr nonlinearity for an undepleted, Bragg-matched probe pulse. The nonlinear responses

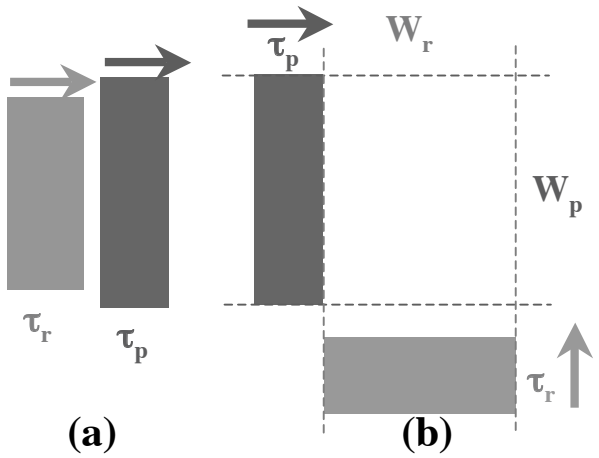

Figure 6.1: The temporal resolution in two-pulse pump-and-probe experiments is strongly affected by the transverse pulse widths and the angle θ between the pulses involved. Optimal resolution is obtained when the pulses propagate collinearly, as in case (a); deviation from collinearity causes the resolution to deteriorate due to the transverse dimensions of the pulses, as in case (b).

of the medium are assumed to be instantaneous compared with the pulse duration[7].

In the conventional single-pump-and-single-probe experiments[8], the temporal resolution cannot be better than the cross-correlation trace of the pulses involved. Optimal resolution is obtained when the pulses propagate collinearly; deviation from collinearity generally causes the resolution to deteriorate as a result of the transverse dimensions of the pulses[9, 10].

For a simple illustration, refer to Fig. 6.1. We consider two extreme cases, i.e., when the pump and probe pulses are propagating parallel, in case (a), or perpendicular, in case (b), to each other. For clarity, we assume that the two pulses are spatially and temporally rectangular and they have the same group velocity v. In the figure, τ/W specifies the pulse temporal duration/transverse dimension and subscript p/r stands for pump/probe. In case (a), the temporal resolution is approximately $\tau_p + \tau_r$; on the other hand, in case (b) it will roughly be $\tau_p + \tau_r + \frac{W_p+W_r}{v}$. When propagating collinearly, the pulse temporal durations alone determine the temporal resolution. Moving away from collinearity, the pulse transverse dimensions start to affect temporal resolution, dominating in the perpendicular case. The bigger W_p and W_r are, the more pronounced such an effect will be. We will show that such a phenomenon is almost absent in the holographic pump-and-probe configuration.

In this chapter, experiments conducted in calcium fluoride (CaF_2) samples are used to verify the theoretical prediction; the temporal resolution of the femtosecond holographic configuration is investigated. An advantage of this configuration is that the natural separation between the diffracted probe pulse and the pump pulses mitigates the difficulty of detection suffered by collinear pump-and-probe experiments.

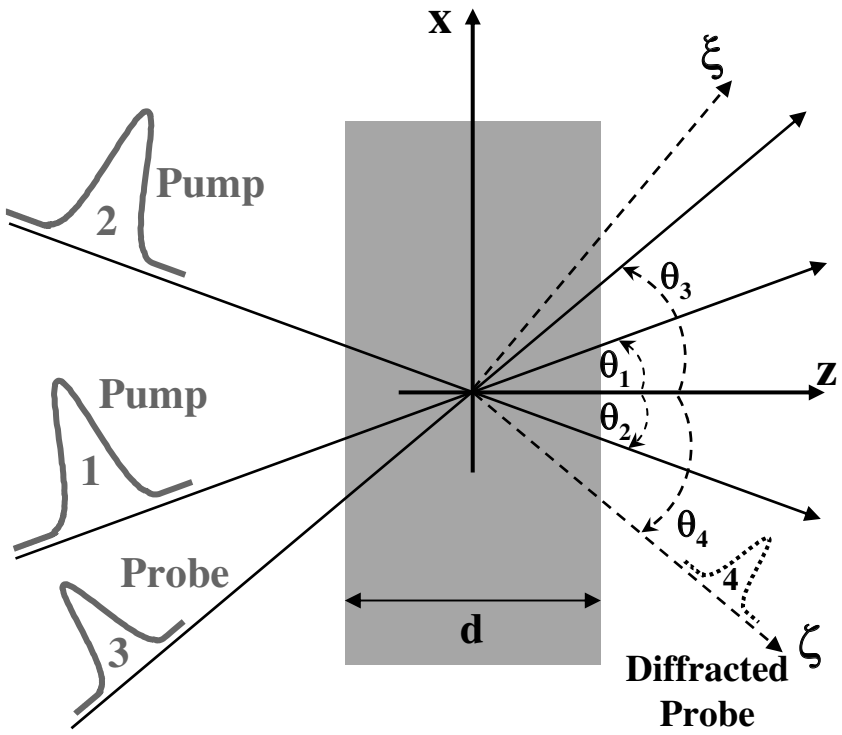

Figure 6.2: Configuration of a femtosecond holographic experiment in the transmission geometry; 1 and 2 are the pump (recording) pulses, while 3 and 4 are the probe and diffracted pulses. The ζ- and ξ- axes are parallel and perpendicular to the direction of propagation of the diffracted probe pulse.

6.2 Theory

Consider the holographic configuration depicted in Fig. 6.2: the spatial and temporal overlap of two pump pulses 1 and 2 results in interference and thus the modulation of light intensity, which modifies the refractive index of the material through the optical Kerr effect

$$n(I) = n_0 + n_2 I, \tag{6.1}$$

where n_0 is the usual, weak-field refractive index of the medium, n_2 is the Kerr coefficient and I is the optical intensity. The probe pulse 3 is diffracted from the resulting index grating, giving rise to the diffracted pulse 4. The quantities $E_i(\mathbf{r}, t)$, ω_i and $\mathbf{k_i}$ represent the electric field, carrier frequency and wavevector of pulse i. Here θ_i is the angle between z-axis and $\mathbf{k_i}$, $\mathbf{r} = (x, y, z)$.We know $\omega_1 = \omega_2 \equiv \omega_p$ and $\omega_3 = \omega_4 \equiv \omega_r$, where subscripts p and r denote pump and probe.

Let $\mathbf{s_i} = (\sin\theta_i, 0, \cos\theta_i)$ be a unit vector along the direction of the wavevector $\mathbf{k_i}$ and $k_i = |\mathbf{k_i}| = \omega_i n_0/c$. We have

$$E_i(\mathbf{r}, t) = \frac{1}{2} A_i(\mathbf{r}, t) e^{j(\omega_i t - k_i \mathbf{s_i}\cdot\mathbf{r})} + c.c.,$$

where $A_i(\mathbf{r},t)$ is the slowly varying field amplitude of $E_i(\mathbf{r},t)$. For convenience, the quantity $E_i(\mathbf{r},t)$ has been normalized such that $|A_i(\mathbf{r},t)|^2 = I_i(\mathbf{r},t)$, the optical intensity.

The Kerr coefficient n_2 is closely related to the third-order nonlinear susceptibility of the material[7]; the polarization of the diffracted pulse is determined by the polarizations of pulses 1, 2 and 3 as well as the tensorial properties of the medium.

In the subsection to follow we resort to the scalar electromagnetic theory for its simplicity to deal with the case when all four pulses are polarized along y direction. It is straightforward to extend this approach to a full tensorial notation. We will write down the equations describing the coupling between the probe and diffracted pulses owing to the concurrent pump pulses. Solutions under the assumption of undepleted probe pulse for the Bragg-matched case will be derived.

6.2.1 Coupled mode equations for pulse holography

We start from the following wave equation for the light field $E_r(\mathbf{r},t) = E_3(\mathbf{r},t) + E_4(\mathbf{r},t)$,

$$\nabla^2 E_r(\mathbf{r},t) - \frac{n_r^2(I_p)}{c^2}\frac{\partial^2}{\partial t^2}E_r(\mathbf{r},t) = 0, \tag{6.2}$$

which applies when the variation Δn_0 of $n_0(\omega)$ is small within the spectral width $\Delta\omega$ of the probe pulse and the effects of dispersion broadening is negligible for the sample thickness d satisfying $d \ll c/\Delta n_0 \Delta\omega$. This inequality holds for most reasonably thin samples; for example, it is satisfied in a 1-mm thick calcium fluoride crystal (1 mm $\ll$ 700 mm) for a Gaussian pulse at 776 nm whose temporal FWHM is 0.22 psec.

The refractive index $n_r(I_p)$ in Eq. (6.2) is specified by Eq. (6.1). In our formalism, the nonlinear contribution $n_2 I_p$ comes from the perturbation caused by pump pulses and couples the probe pulse to the diffracted pulse when the Bragg condition

$$\mathbf{k_1} - \mathbf{k_2} = \mathbf{k_3} - \mathbf{k_4}$$

is satisfied. The Kerr effect transcribes the intensity pattern established by the two intense, interfering pump pulses into an instantaneous, transient index modulation

$$n_2 I_p = n_2\left(|A_1|^2 + |A_2|^2 + A_1^* A_2 e^{j\mathbf{K}\cdot\mathbf{r}} + A_1 A_2^* e^{-j\mathbf{K}\cdot\mathbf{r}}\right). \tag{6.3}$$

The spatially oscillating part on the right-hand side of Eq. (6.3), which can be cast as $\Delta n(\mathbf{r},t)\cos(\mathbf{K}\cdot\mathbf{r})$, is responsible for the coupling between the (much weaker) pulses 3 and 4. Here $\mathbf{K} = \mathbf{k_1} - \mathbf{k_2}$ is the grating vector.

In general, a set of four equations is required to describe the coupling effects between the four field amplitudes in Fig. 6.2, just as in the optical four-wave mixing (FWM) configuration. In our

femtosecond holographic setting, the pump amplitudes A_1 and A_2 are barely affected by the probe amplitudes A_3 and A_4 because pump pulses are much more intense. Moreover, it is justifiable to neglect the coupling effects between A_1 and A_2 due to a weak coupling strength. As a result, we can conveniently discard the differential equations associated with A_1 and A_2 and incorporate their effects into the term $\Delta n(\mathbf{r}, t)$.

We can write down the following coupled mode equations for pulse holography when the Bragg condition is satisfied (v_r is the group velocity of the probe pulse):

$$\left[(\mathbf{s_3} \cdot \nabla) + \frac{1}{v_r}\frac{\partial}{\partial t}\right] A_3 = -j\frac{\pi \Delta n}{\lambda_r} A_4, \tag{6.4a}$$

$$\left[(\mathbf{s_4} \cdot \nabla) + \frac{1}{v_r}\frac{\partial}{\partial t}\right] A_4 = -j\frac{\pi \Delta n}{\lambda_r} A_3. \tag{6.4b}$$

In arriving at the equations Eqs. (6.4a) and (6.4b) above, several approximations have been adopted:

- Only the third-order material nonlinearity comes into play. The second-order nonlinearity term is discarded for irrelevance; higher order terms are also ignored because the third order term dominates in magnitude.

- We ignore the terms associated with $(\Delta n)^2$ and keep those involving $n\Delta n$ because typically (and in our experiments) $\Delta n/n \leq 10^{-4}$.

- We ignore the second order terms $\frac{\partial^2}{\partial t^2} A_i$ compared with $\omega_r \frac{\partial}{\partial t} A_i$ since the spectral bandwidth $\Delta\omega_i$ of A_i is much smaller than its carrier frequency ω_r.

- The longitudinal second-order derivative $(\mathbf{s_i} \cdot \nabla)^2 A_i$ is ignored compared with $k_r(\mathbf{s_i} \cdot \nabla) A_i$ because the spatial bandwidth Δk_i of A_i is much smaller than its carrier k_r (slowly varying amplitude approximation). The transverse second-order derivative are also ignored thanks to the next two conditions.

- Diffraction broadening is negligible because the Rayleigh range of the pulse is much longer than the sample thickness.

- The self-focusing effects experienced by the intense pump pulses can be ignored when the self-focusing distance is much larger than the sample thickness[7].

The main difference between the coupled mode equations Eqs. (6.4a) and (6.4b) for pulse holography and those for continuous-wave (cw) holography is the presence of the time derivative to account for the short pulse temporal duration. Furthermore, the amplitude A_i is a function of both x and z since the pulses have finite spatial extent[11].

6.2.2 Solution of the diffracted pulse: undepleted incident probe

We can solve for the amplitude of the diffracted pulse A_4 using only Eq. (6.4b) if we make the assumption that the probe pulse is undepleted by the transient grating; this is equivalent to the first Born approximation[12]. To facilitate the solution, we convert to a retarded time frame by performing the following change of variables:

$$\begin{aligned}\zeta &= z\cos\theta_4 + x\sin\theta_4,\\ \xi &= x\cos\theta_4 - z\sin\theta_4,\\ \tau &= t - \frac{z}{v_r}\cos\theta_4 - \frac{x}{v_r}\sin\theta_4,\end{aligned}$$

where τ is the retarded time and ζ/ξ is the longitudinal/transverse spatial coordinate of the diffracted pulse, as shown in Fig. 6.2. Let $\mathbf{r}' = (\xi, y, \zeta)$; straightforward substitution leads us to a much more simplified differential equation from Eq. (6.4b):

$$\frac{\partial A_4(\mathbf{r}',\tau)}{\partial\zeta} = -j\frac{\pi\Delta n(\mathbf{r}',\tau)}{\lambda_r}A_3(\mathbf{r}',\tau). \tag{6.5}$$

The boundary condition $A_4\left(z=-\frac{d}{2}\right)=0$ translates into $A_4\left(\zeta=-\frac{d}{2}\sec\theta_4+\xi\tan\theta_4\right)=0$ and leads to the solution at $z=d/2$

$$A_4(\xi,y,z=d/2,\tau) = \frac{-j\pi}{\lambda_r}\int\limits_{-\frac{d}{2}\sec\theta_4+\xi\tan\theta_4}^{\frac{d}{2}\sec\theta_4+\xi\tan\theta_4}\Delta n A_3 \mathrm{d}\zeta. \tag{6.6}$$

The diffraction efficiency η is defined as the energy ratio between the diffracted pulse and transmitted pulse.

$$\eta = \frac{\iiint\limits_{-\infty}^{\infty}|A_4(\zeta=\frac{d}{2}\sec\theta_4+\xi\tan\theta_4)|^2\mathrm{d}\xi\mathrm{d}y\mathrm{d}\tau}{\iiint\limits_{-\infty}^{\infty}|A_3(z=\frac{d}{2})|^2\mathrm{d}x\mathrm{d}y\mathrm{d}t}. \tag{6.7}$$

The amplitudes of pump and probe pulses ($i=1,2,3$) can be represented as $A_i(\mathbf{r}',t)=\sqrt{I_{i0}}e^{\phi_i(\mathbf{r}',\tau)}$, where I_{i0} is the peak intensity of the i-th pulse. Let pump and probe pulses possess temporally and spatially Gaussian profiles and be incident simultaneously onto the sample. Then the exponent ϕ_i, which describes the free propagation of pulses 1, 2 and 3, obeys the following relation:

$$\phi_i(\mathbf{r}',\tau) = -4\ln 2\left[\frac{(\tau+\frac{\zeta}{v_r}-\frac{\zeta\cos\alpha_i+\xi\sin\alpha_i}{v_i})^2}{\tau_i^2}+\frac{(\xi\cos\alpha_i-\zeta\sin\alpha_i)^2+y^2}{D_i^2}\right], \tag{6.8}$$

where v_i ($v_1=v_2\equiv v_p$, $v_3=v_4\equiv v_r$) is the group velocity, and τ_i and D_i ($\tau_1=\tau_2\equiv\tau_p$, $\tau_3\equiv\tau_r$, $D_1=D_2\equiv D_p$, $D_3\equiv D_r$) are the temporal and spatial FWHM of the pulse amplitude, $\alpha_i=\theta_i-\theta_4$.

Now we solve for the case when the incident probe pulse is delayed by Δt with respect to the pump pulses. The diffracted pulse amplitude $A_4(z = d/2)$ becomes

$$\frac{-j\pi}{\lambda_r} \int_{-\frac{d}{2}\sec\theta_4+\xi\tan\theta_4}^{\frac{d}{2}\sec\theta_4+\xi\tan\theta_4} 2n_2\sqrt{I_{10}I_{20}I_{30}}e^{[\phi_1(\mathbf{r}',\tau)+\phi_2(\mathbf{r}',\tau)+\phi_3(\mathbf{r}',\tau-\Delta t)]}\mathrm{d}\zeta, \tag{6.9}$$

where we have used $\Delta n(\mathbf{r}',\tau) = 2n_2\sqrt{I_{10}I_{20}}e^{\phi_1+\phi_2}$. Carrying out the integral and placing the result in Eq. (6.7), we end up with an analytical expression of the diffraction efficiency, whose form lends to numerical evaluation:

$$\eta(\Delta t) = \frac{D_p}{4\sqrt{2}\mathcal{P}\tau_r D_r\sqrt{D_p^2+2D_r^2}}\left(\frac{\pi n_2}{\lambda_r}\right)^2 I_{10}I_{20}\mathcal{I}, \tag{6.10}$$

where

$$\begin{aligned}
\mathcal{I}(\Delta t) &= \int_{-\infty}^{\infty}\!\!\int\left\{\mathrm{erf}\left[2\sqrt{\ln 2\mathcal{P}}\left(\frac{d}{2}\sec\theta_4+\mathcal{S}\right)\right]+\mathrm{erf}\left[2\sqrt{\ln 2\mathcal{P}}\left(\frac{d}{2}\sec\theta_4-\mathcal{S}\right)\right]\right\}^2\exp\left\{8\ln 2\left[\frac{\mathcal{Q}^2}{\mathcal{P}}-\mathcal{R}\right]\right\}\mathrm{d}\xi\mathrm{d}\tau,\\
\mathcal{P} &= \sum_{i=1}^{3}\left(\frac{\sin\alpha_i}{D_i}\right)^2+\sum_{i=1}^{3}\frac{1}{\tau_i^2}\left(\frac{\cos\alpha_i}{v_i}-\frac{1}{v_r}\right)^2,\\
\mathcal{Q}(\xi,\tau,\Delta t) &= \xi\sum_{i=1}^{3}\frac{\sin 2\alpha_i}{2D_i^2}+\sum_{i=1}^{3}\frac{\left(\tau-\frac{\xi\sin\alpha_i}{v_i}\right)\left(\frac{\cos\alpha_i}{v_i}-\frac{1}{v_r}\right)}{\tau_i^2}+\Delta t\frac{1-\cos\alpha_3}{v_r\tau_r^2},\\
\mathcal{R}(\xi,\tau,\Delta t) &= \xi^2\sum_{i=1}^{3}\left(\frac{\cos\alpha_i}{D_i}\right)^2+\sum_{i=1}^{2}\frac{1}{\tau_i^2}\left(\tau-\frac{\xi\sin\alpha_i}{v_i}\right)^2+\frac{1}{\tau_r^2}\left(\tau-\Delta t-\frac{\xi\sin\alpha_3}{v_r}\right)^2,\\
\mathcal{S}(\xi,\tau,\Delta t) &= \xi\tan\theta_4-\frac{\mathcal{Q}}{\mathcal{P}}.
\end{aligned}$$

To gain some insight into how the parameters θ_p and Δt affect the diffraction efficiency, we adopt the paraxial approximation: $\sin\theta_p \approx \theta_p$ and $\cos\theta_p \approx 1$. By setting $\tau_p = \tau_r$ and $v_p = v_r$, we obtain after some straightforward algebraic manipulations:

$$\eta(\Delta t) \approx \eta_{peak}\exp\left[-8\ln 2\left(\frac{\Delta t}{\delta\tau_r}\right)^2\right], \tag{6.11}$$

The peak value of the diffraction efficiency $\eta_{peak} = \eta(\Delta t = 0)$ and the dimensionless broadening factor δ are given by

$$\eta_{peak} = \left(\frac{2\pi d}{\lambda_r}\right)^2\frac{n_2^2 I_{10}I_{20}}{\sqrt{3+14q}(1+2D_r^2/D_p^2)},$$

and

$$\delta = \sqrt{\frac{3+14q}{2+4q}}, \tag{6.12}$$

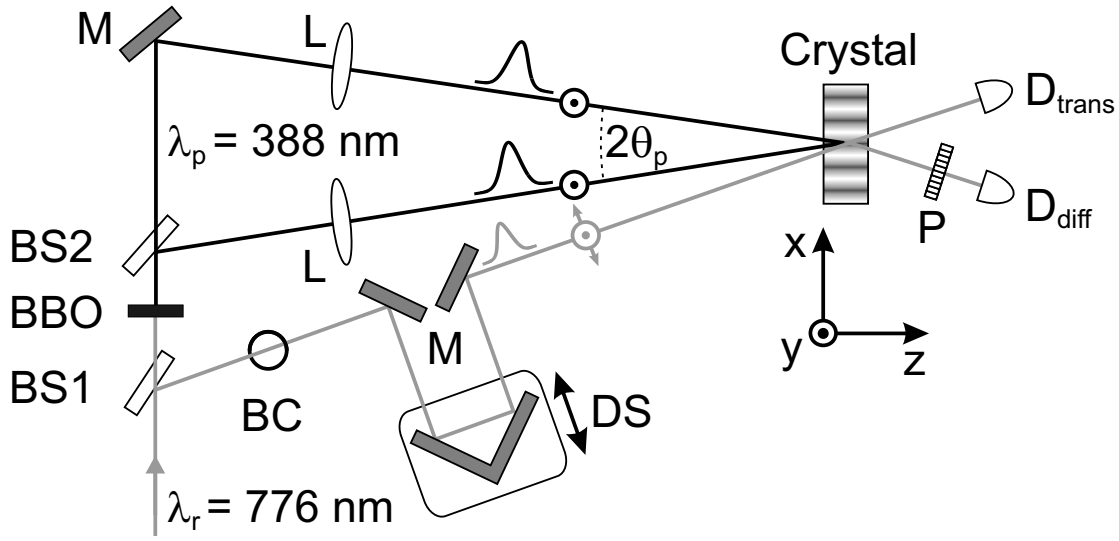

Figure 6.3: Schematic illustration of the holographic pump-and-probe setup. (BC: Berek compensator, serving as half-wave plate for the probe pulse; BS: beam splitter; D: photodetector; DS: probe delay stage; L: lens; M: mirror; P: polarizer)

where we have used $D = D_p D_r / \sqrt{D_p^2 + 2D_r^2}$, $\theta_1 = -\theta_2 = \theta_p$ and $q = (D\theta_p/\tau_r v_r)^2$. The function $\eta(\Delta t)$ gives us a measure of the temporal resolution of the holographic pump-and-probe setup through the broadening factor $\delta(\theta_p)$, which is the ratio between the FWHM of $\eta(\Delta t)$ and that of our probe pulse intensity profile. Although $\delta(\theta_p)$ is a monotonically increasing function of θ_p, it has a rather narrow range: $1.22 \leq \delta < 1.87$ according to Eq. (6.12). It is explicit that the temporal resolution is not severely affected by the angle of intersection.

The assumption of negligible difference between the pump and probe group velocities, being applicable to some materials (for instance, CaF_2), cannot be justified in the general case. The velocity difference can result in an additional broadening of $\eta(\Delta t)$.

6.3 Experimental results and discussion

Our experimental setup is illustrated in Fig. 6.3. An axially symmetric pulse at $\lambda_r = 776$ nm is obtained from a Ti:Sapphire amplified laser system CPA-2010 from Clark-MXR, Inc. The temporal and spatial FWHM of the pulse intensity are measured to be 0.22 psec and 3.5 mm, respectively. Four percent of the pulse energy is tapped and serves as the probe pulse displaced by a variable delay stage. The rest of the pulse is passed through a 1-mm-thick BBO ($\beta - BaB_2O_4$) crystal to generate a pulse at $\lambda_p = 388$ nm, which is split into two identical pump pulses and then focused down to one-fifth of their original diameter inside the 1 mm thick calcium fluoride sample for more pronounced nonlinear response. The angle between the pump pulses $2\theta_p$ is the value "inside" the

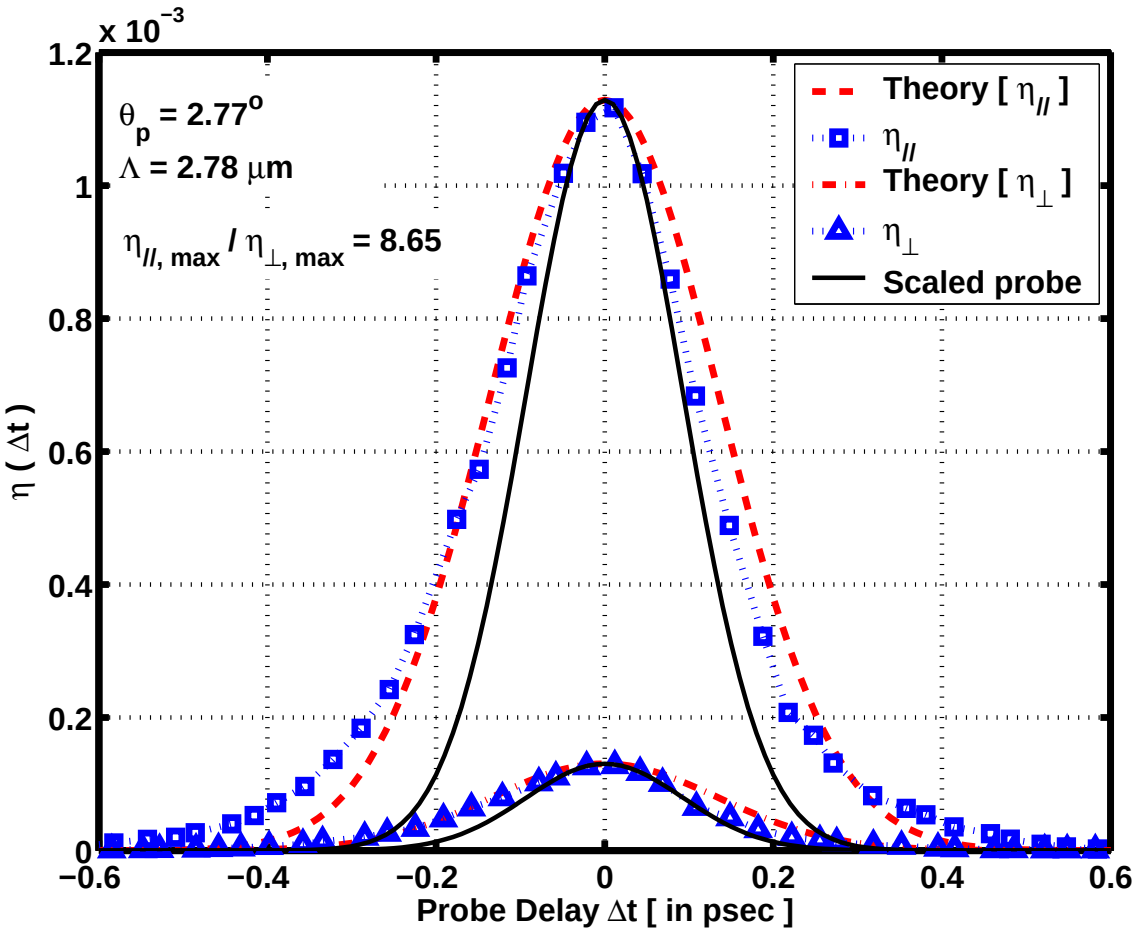

Figure 6.4: Comparison between theory and experiment ($\theta_p = 2.77^o$). Polarization dependence of the measured diffracted probe trace $\eta(\Delta t)$ is shown. The dashed lines are obtained from the theory. The solid lines are scaled probe pulse intensity profiles. Λ stands for the grating period.

sample. The peak intensity of each of the pump pulses inside the sample is about 180 GW/cm^2. The diffracted pulse is detected by a photodiode, in front of which a polarizer is used to extract the desired polarization. The optimal overlap of the pulses is then obtained by maximizing the detected diffracted pulse energy.

Calcium fluoride (chemical formula: CaF_2) is an ionic crystal with a face centered cubic structure (point group symmetry $m3m$). It has a very wide bandgap of about 12 eV[13] and a Kerr coefficient n_2 of 3×10^{-7} cm^2/GW around 580 nm[7, 14]. Since the photon energy carried by our pump pulses (3.2 eV) is far lower than the bandgap, the bound electrons are responsible almost exclusively for the observed nonlinear effect. In our experiment, the third-order, nonresonant nonlinearity (or Kerr nonlinearity) is the dominant effect.

The measured diffraction efficiency for $\theta_p = 2.77°$ as a function of probe delay, $\eta(\Delta t)$, is shown by the symbols in Fig. 6.4 for two different probe polarizations: parallel (the $\eta_{//}$ trace) or perpen-

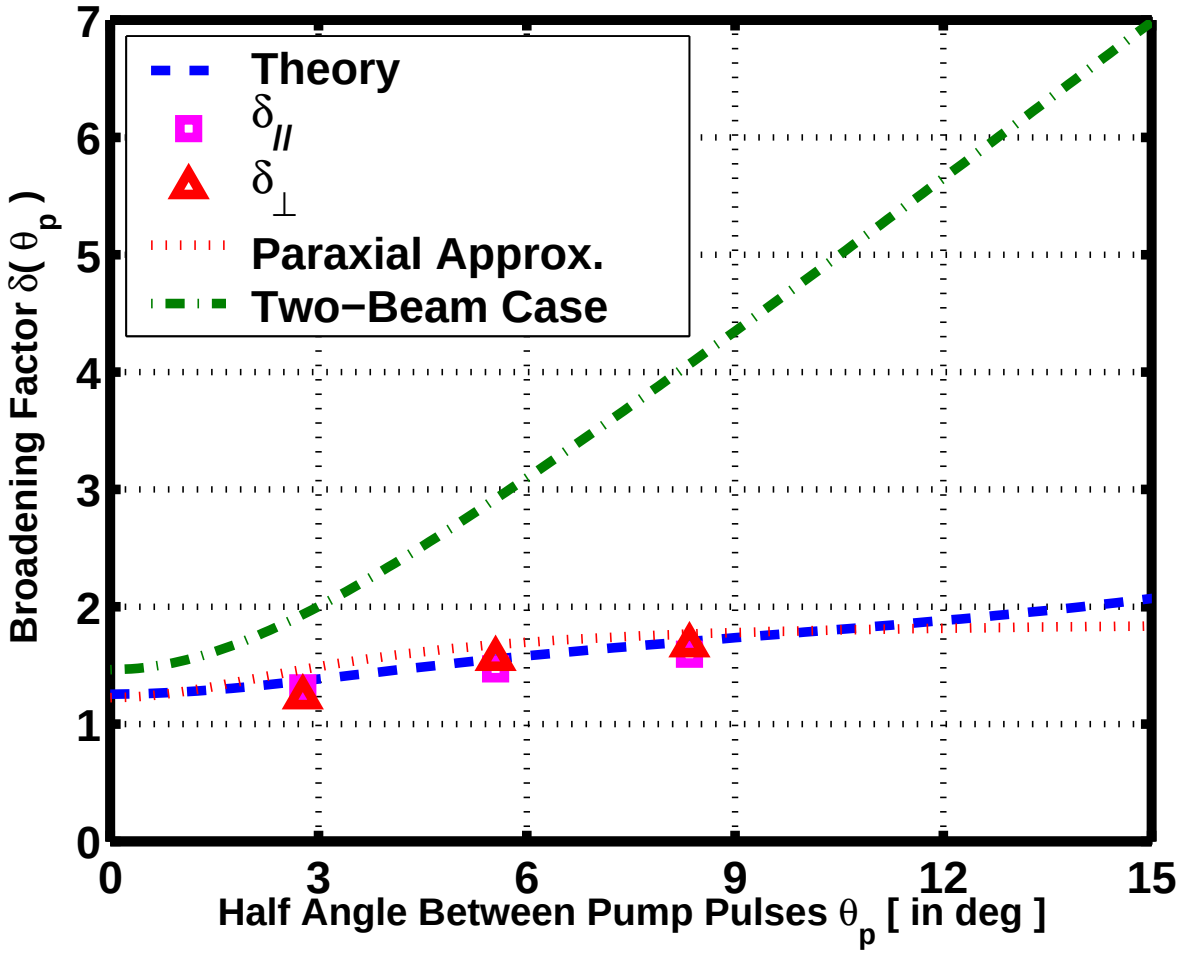

Figure 6.5: Temporal resolution of the holographic pump-and-probe setup. The dashed curve is calculated numerically according to the theory; the solid curve is plotted under paraxial approximation, using Eq. (6.12). The dash-dot curve, drawn here for comparison, is the temporal resolution for the single-pump-single-probe configuration.

dicular (the $\eta_\perp$ trace) to the pumps' polarization. The dashed and dash-dot lines are the theoretical predictions; the appropriate group velocities used in numerical evaluations are calculated with the help of the data compiled in Ref.[15]. The peak diffraction efficiency of each experimental trace is interpolated by quadratically fitting the three highest values of $\eta(\Delta t)$. For the purpose of comparison, the scaled profiles of the incident probe intensity are also shown as solid lines. Numerical simulation shows that the trace $\eta(\Delta t)$ is symmetric and its maximum always occurs at $\Delta t = 0$ when the intensity peaks of all three pulses coincide at the center of the CaF_2 sample, which is also the origin of our coordinate system. We can see that the experimental results agree well with the theory. Moreover, the fitted value of the nonlinear refractive index n_2 from our experiment is 4.4×10^{-7} cm^2/GW, a reasonable value compared with that from the literature.

According to the isotropic, anharmonic model of nonlinear electronic response away from material

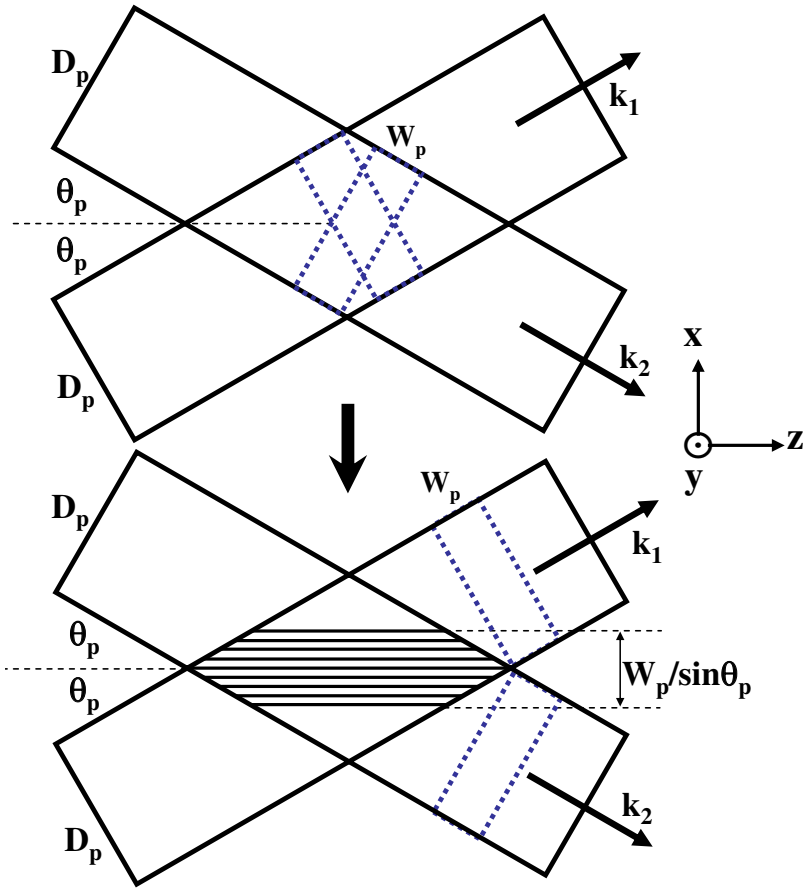

Figure 6.6: The concept of the composite pump. The limited longitudinal dimension of femtosecond pulses gives rise to a strip-like region of actual overlap whose width is determined by the pulse temporal duration as well as the angle of intersection, as shown in the lower part.

resonance, the peak diffraction efficiency of the $\eta_{//}$ trace is expected to be 9 times as large as that of the $\eta_{\perp}$ trace[7]. In our experiment, this factor turns out to be 8.2 ± 0.4; the discrepancy can be explained by the deviation from Kleinman's symmetry[14].

The broadening factor as a function of the half-angle between pump pulses $\delta(\theta_p)$ is plotted in Fig. 6.5: the dashed curve is computed numerically according to the theory, and the solid curve is plotted using Eq. (6.12) under the assumption of paraxial approximation. Experiments are carried out for three different values of θ_p, namely, 2.77°, 5.55° and 8.35°. We see that the experimental results closely track the theoretical trend, and $\delta(\theta_p)$ almost remains constant for the experiments, as opposed to the conventional two-beam pump-and-probe setup[10, 9], whose broadening factor is defined based on the cross-correlation trace of the pump and probe intensities. We reproduce the two-beam broadening factor (in this case, θ_p is the half-angle between the pump and probe) as the dash-dot curve in Fig. 6.5 for the same parameters as used in our holographic experiment.

The key to this almost undegraded temporal resolution in the holographic pump-and-probe

setup lies in the concept of "composite pump," which can be explained with the help of Fig. 6.6. For simplicity, we consider the case when the pump pulses have rectangular spatial intensity distribution with transverse and longitudinal dimensions D_p and $W_p = v_p\tau_p$ ($W_p \approx 46\mu$m in CaF_2 if $\tau_p = 220$fs). The overlap of pump pulses is shown in the upper part of the figure as a diamond-shaped region traced out by dotted lines. As the pump pulses travel and intersect, this region of overlap, the composite pump, propagates along the z-axis with a velocity $v_c = v_p/\cos\theta_p$ and has an effective transverse width of $D_c = W_p/\sin\theta_p$ (shown in the lower part of the figure); this effective width becomes smaller when θ_p gets bigger. As evident from the expression, D_c is independent of the spatial dimension D_p of the pump pulses and solely determined by the pulse temporal duration τ_p and the angle of intersection. If we increase the angle $2\theta_p$ between the pump pulses, the incident angle θ_3 of the probe pulse must also get bigger in order to satisfy the Bragg condition.

Now we can consider the influence of the composite pump on the probe pulse just as in a two-beam case. Two-beam cross-correlation simulation suggests a broader temporal response for the increased angular intersection; on the other hand, it produces a narrower temporal response owing to a shrinking D_c. The reduction in the transverse width of the composite pump constantly counteracts the effect of an augmented probe incident angle and leaves the temporal resolution in this configuration almost unchanged.

6.4 Conclusion

With the assumption of an undepleted incident probe pulse, we solved the coupled mode equations for the femtosecond holography in the case of instantaneous material response. The solution is well corroborated by the experiments conducted in calcium fluoride crystals. An important implication of the experimental data obtained for different intersection angles and grating periods is that the temporal resolution in the holographic pump-and-probe setup is not reduced much by the non-collinearity. This result will be useful for probing grating-period-dependent mechanisms, such as diffusion, in materials.

Bibliography

[1] Andreas Othonos. Probing ultrafast carrier and phonon dynamics in semiconductors. *Appl. Phys. Rev.*, 83(4):1789–1830, February 1998.

[2] P. C. Becker, H. L. Fragnito, C. H. B. Cruz, J. Shah, R. L. Fork, J. E. Cunningham, J. E. Henry, and C. V. Shank. Femtosecond intervalley scattering in GaAs. *Appl. Phys. Lett.*, 53(21):2089–2090, November 1988.

[3] H. Mahr and M. D. Hirsch. Optical up-conversion light gate with picosecond resolution. *Opt. Commun.*, 13(2):96–99, 1975.

[4] R. T. Hayes, C. J. Walsh, and M. R. Wasielewski. Using three-pulse femtosecond spectroscopy to probe ultrafast triplet energy transfer in zinc meso-tetraarylporphyrin-perylene-3,4-dicarboximide dyads. *J. Phys. Chem. A*, 108(16):3253–3260, April 2004.

[5] P. M. Norris, A. P. Caffrey, R. J. Stevens, J. M. Klopf, J. T. McLeskey, and A. N. Smith. Femtosecond pump-probe nondestructive examination of materials. *Rev. Sci. Instrum.*, 74(1):400–406, January 2003.

[6] Herwig Kogelnik. Coupled wave theory for thick hologram gratings. *Bell Syst. Tech. J.*, 48(9):2909–2947, November 1969.

[7] R. W. Boyd. *Nonlinear Optics*. Academic Press, New York, 2nd edition, 2003.

[8] C. L. Thomsen, D. Madsen, S. R. Keiding, J. Thogersen, and O. Christiansen. Two-photon dissociation and ionization of liquid water studied by femtosecond transient absorption spectroscopy. *J. Chem. Phys.*, (7):3453–3462, February 1999.

[9] J. C. Diels and W. Rudolph. *Ultrashort Laser Pulse and Phenomena*. Academic Press, New York, 1st edition, 1996.

[10] M. Ziolek, R. Naskrecki, M. Lorenc, J. Karolczak, J. Kubicki, and A. Maciejewski. The influence of the excitation geometry on the temporal resolution in femtosecond pump-probe experiments. *Opt. Commun.*, 197(4-6):467–473, October 2001.

[11] L. Solymar and D. J. Cooke. *Volume Holography and Volume Gratings*. Academic Press, New York, 1981.

[12] M. Born and E. Wolf. *Principles of Optics*. Cambridge, London, 7th edition, 1999.

[13] M. Huisinga. *Ultraviolet Photoelectron Spectroscopy and Electron Stimulated Desorption from* CaF_2. PhD thesis, Freie University Berlin, April 1999.

[14] R. T. Lynch, M. D. Levenson, and N. Bloembergen. Experimental test for deviation from Kleinman's symmetry in third-order susceptibility tensor. *Phys. Lett. A*, 50(1):61–62, November 1974.

[15] H. H. Li. Refractive-index of alkaline-earth halide and its wavelength and temperature derivatives. *J. Phys. Chem. Ref. Data*, 9(1):161–289, 1980.

Chapter 7

Nonlinear absorption processes in lithium niobate crystals investigated with femtosecond light pulses

7.1 Introduction

Femtosecond high-power light pulses have become increasingly important in physics and technology of light-matter interactions. One crucial advantage of such pulses is the possibility to deposit rapidly and precisely light energy in solids. The relevant experiments have led to the discovery of a number of new effects in wide-gap transparent optical materials including the direct recording of 3D photonic structures[1, 2], self-organized nanogratings[3] and light-induced anisotropy in glasses[4]. Some publications, see[5, 6] and references therein, dealt with determination of Kerr and two-photon absorption coefficients in wide-gap optical materials, including liquids.

Several publications were devoted to pulsed studies of the photorefractive effect in semiconductors, mostly in the sub-nanosecond range, i.e., $10^{-11} \sim 10^{-9}$ sec, see[7, 8, 9] and references therein. It was found that a free-carrier contribution to the refractive index change and two-photon absorption can be important in the high intensity range in addition to the conventional photorefractive nonlinearity caused by charge separation and the linear electro-optic effect.

In this chaper we present the results of the experimental and theoretical studies of the light-induced nonlinear absorption processes in lithium niobate crystals ($LiNbO_3$) on the sub-picosecond ($\sim 10^{-13}$ sec) time scale. This material is rather important for various nonlinear and photorefractive applications including frequency conversion[10], optical parametric oscillation, holographic data storage[11], Bragg reflection[12, 13, 14] and domain engineering[15].

Moving from the sub-nanosecond to the subpicosecond range is expected to result in a strong change of the character of nonlinear-optical effects, in particular, direct two-photon absorption

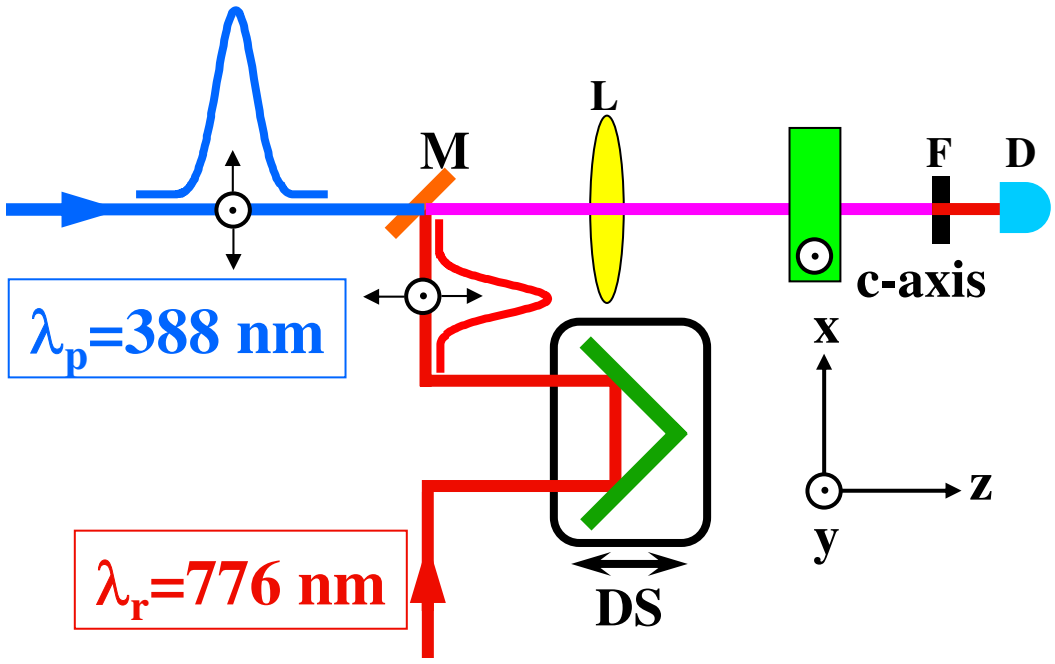

Figure 7.1: Schematic diagram of a collinear pump-probe experiment; M is a dielectric dichroic mirror, L is a long-focus (500 mm) lens, F is a band edge filter for the pump light, D is a photodiode, DS is the probe delay stage.

processes and the Kerr nonlinearity, the latter of which has been addressed in the previous chapter for intense femtosecond pulses. Two-photon absorption processes will therefore be the main topic of this chapter.

7.2 Collinear pump-and-probe experimental setup

The pump and probe pulses in our experiment are acquired as follows: an axially symmetric pulse at the wavelength $\lambda_r = 776$ nm is obtained from a Ti:Sapphire amplified laser system CPA-2010 from Clark-MXR, Inc. The temporal and spatial full-width-at-half-maximum (FWHM) of the pulse intensity are measured to be 0.22 psec and 3.5 mm, respectively. Four percent of the pulse energy is tapped and serves as the probe pulse displaced by a variable delay stage. The rest of the pulse is passed through a 1-mm-thick BBO ($\beta - BaB_2O_4$) crystal to generate the pump pulse at the wavelength $\lambda_p = 388$ nm; the conversion efficiency of the second harmonic generation (SHG) process is about 45%, and the remaining light at λ_r is then blocked with the help of a dielectric mirror.

Our experimental setup is illustrated schematically in Fig. 7.1. Both the pump and probe pulses are propagating along the z-axis and incident normally onto the xy face of a $LiNbO_3$ sample. The temporal delay of the probe pulse relative to the pump pulse can be adjusted by a variable delay stage. The optic axis (c-axis) of the sample is parallel to the y coordinate. The polarization vectors

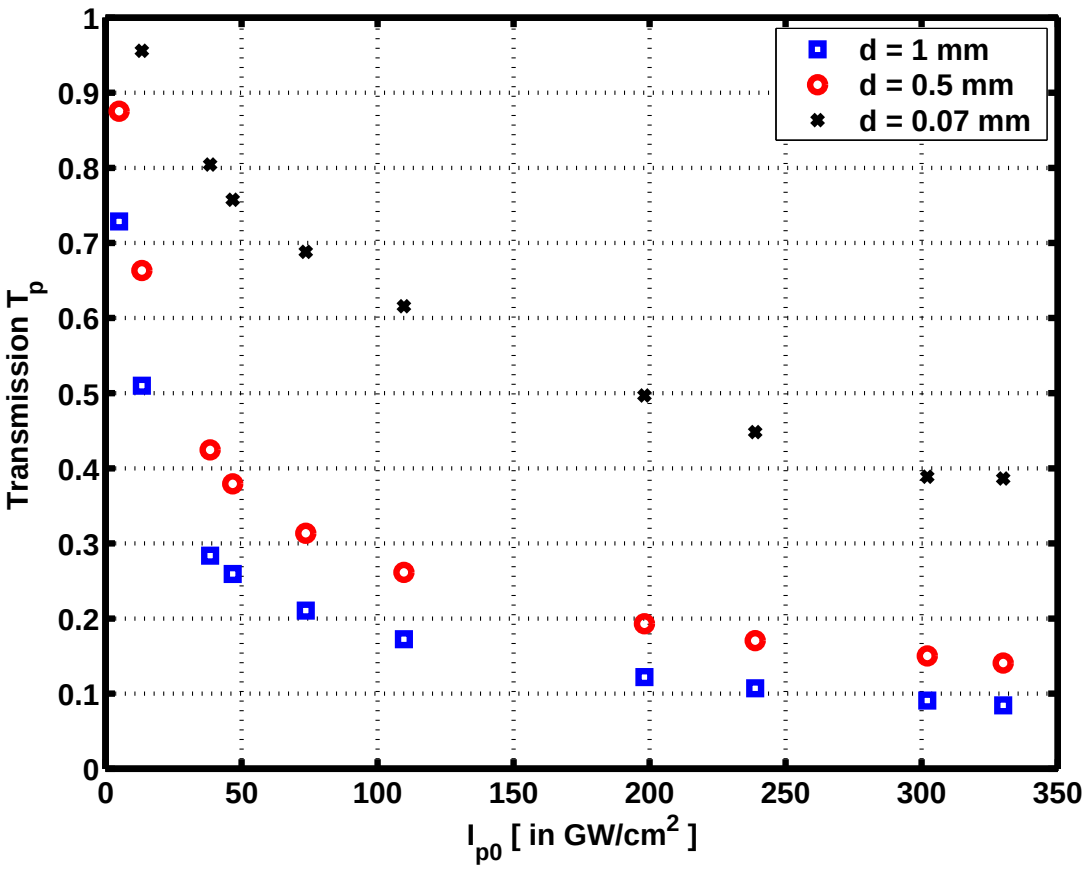

Figure 7.2: Transmission coeffcient T_p versus peak pump pulse intensity I_{p0}. The squares, circles and crosses correspond to the samples 1, 2 and 3, respectively.

of the pulses are separately controlled by specialized half-wave plates (Berek compensators) and are either parallel or perpendicular to the optic axis. The spatial FWHM of the pulses (after passing through a converging lens) at the input face is about 0.6 mm. The peak intensity of the pump pulse I_{p0} ranges from ~ 1 to ~ 330 GW/cm^2. The maximum fluence of the pump pulse is about 79 mJ/cm^2. A photo-diode is used to measure the output energy of either the pump or probe pulse by choosing the proper filter to block one of them out.

Four different samples of $LiNbO_3$, labelled as 1, 2, 3 and 4, are used in the experiments. The values of the thicknesses d are 1, 0.5, 0.07 and 0.07 mm, respectively. Samples 1, 2 and 3 are nominally undoped and possess very small ($\alpha_0 \leq 0.1$ cm^{-1}) linear absorption coefficients at 388 and 776 nm. Sample 4 is iron doped; the iron concentration c_{Fe} is about 5.6×10^{-19} cm^{-3}, and the linear absorption coefficient α_0 at 388 nm is about 15 cm^{-1}. For all the samples and wavelengths used, the linear absorption is negligibly small, i.e., $\alpha_0 d \ll 1$.

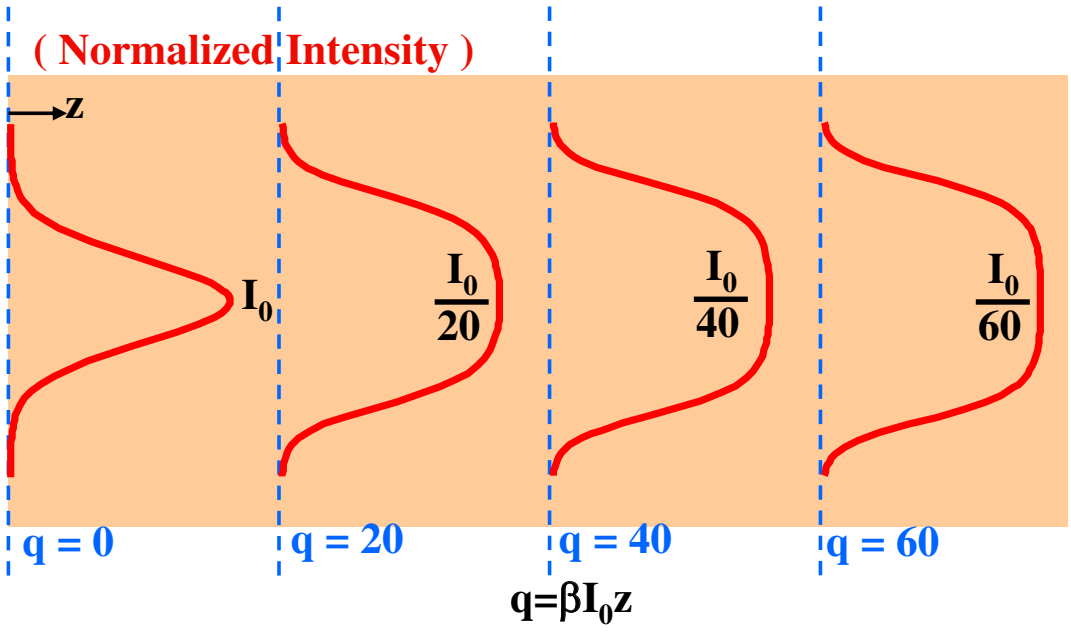

Figure 7.3: Transverse beam profile (normalized intensities) for different values of the nonlinear absorption parameter $q_p = \beta_p I_{p0} d$.

7.3 Two-photon absorption process for a single femtosecond pulse

7.3.1 Motivation

To understand and facilitate the modeling of the phenomena observed in the experimental setup as shown in Fig. 7.1, we first need to know how a single, intense femtosecond pulse evolves in the $LiNbO_3$ sample. Some preliminary experimental results with only the presence of the pump pulse at λ_p are shown in Fig. 7.2: T_p, the transmission coefficient corrected for surface reflections, is plotted against the peak intensity I_{p0}. Without nonlinear absorption, we would have got roughly the same T_p values for all input intensities. It is conspicuous that the more intense the pulse is, the more strongly it gets absorbed in the sample. The presence of nonlinear absorption is indisputable. In the following subsection we shall develop a simple theory for two-photon absorption and try to explain the trend observed in Fig. 7.2.

7.3.2 Theory of two-photon absorption

We can write down the following equation directly from the Maxwell's equations under the assumptions of negligible beam diffraction and frequency dispersion:

$$\left(\frac{\partial}{\partial z}+\frac{1}{v_p}\frac{\partial}{\partial t}\right)I_p=-\beta_p I_p^2, \tag{7.1}$$

where $v_p=c/n_p$ is the pulse velocity in the medium. Eq. (7.1) belongs to a special class of differential equations called Bernoulli's equation; it can be solved analytically. The quantity $\alpha_p=\beta_p I_p$ can be regarded as the effective absorption coefficient for the pulse, where β_p represents the quadratic absorption coefficient at λ_p. We have ignored the linear absorption in Eq. (7.1).

The solution to the differential equation Eq. (7.1) subject to the boundary condition at the input plane $z=0$

$$I_p(x,y,z=0,t)=I_{p0}\exp\left(-\frac{t^2}{\tau_p^2}-\frac{x^2+y^2}{D_p^2}\right)$$

is

$$I_p(x,y,z,t)=\frac{I_{p0}}{\beta_p I_{p0} z+\exp\left[\frac{(t-z/v_p)^2}{\tau_p^2}+\frac{x^2+y^2}{D_p^2}\right]}, \tag{7.2}$$

where a Gaussian intensity profile of the pulse has been assumed; τ_p and D_p specify the temporal and spatial extent of the pulse, respectively. Eq. (7.2) gives a description of the pulse intensity with the presence of two-photon absorption. If we ride on the top of the pulse as it is propagating inside the nonlinear medium, i.e., setting $t-z/v_p=0$, the intensity profile will appear to us as depicted in Fig. 7.3. We see that the preferential absorption near the center of the pulse results in the flattening of the Gaussian intensity profile. This flattening effect is more and more obvious as the pulse travels farther down the road within the medium.

The transmission coefficient T_p is defined as the ratio of the output pulse energy to the input pulse energy, and for a crystal thickness of d, T_p can be computed from Eq. (7.2) by integrating the output intensity $I_p(x,y,z=d,t)$ over t and the transverse coordinates x,y and dividing the quantity by its value at $z=0$:

$$T_p=\frac{\int_{-\infty}^{\infty}\iint\frac{I_{p0}\mathrm{d}x\mathrm{d}y\mathrm{d}t}{q_p+\exp\left[\frac{(t-d/v_p)^2}{\tau_p^2}+\frac{x^2+y^2}{D_p^2}\right]}}{\pi\sqrt{\pi}\tau_p D_p^2 I_{p0}},$$

where $q_p=\beta_p I_{p0} d$ is the unitless nonlinear absorption parameter. By making the change of variable $\rho=x^2+y^2$ and taking advantage of the indefinite integral relation

$$\int\frac{\mathrm{d}x}{q+pe^{ax}}=\frac{x}{q}-\frac{1}{aq}\ln\left(q+pe^{ax}\right),$$

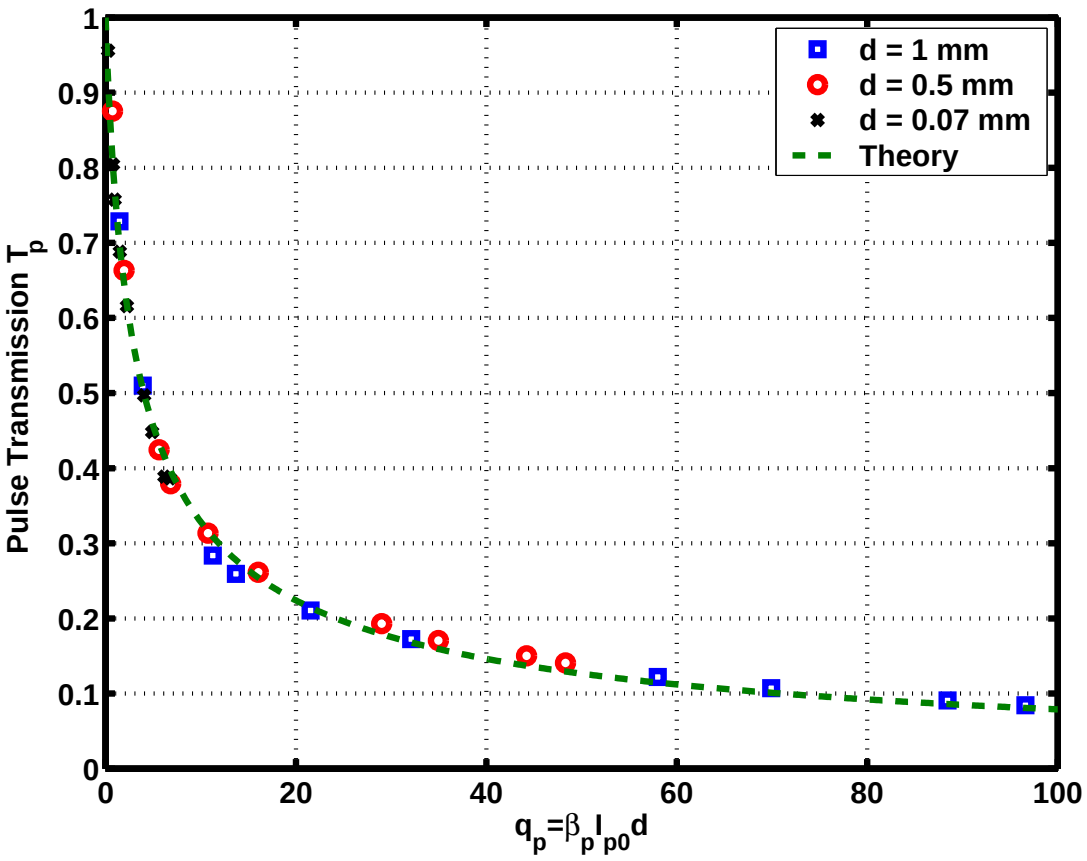

Figure 7.4: Dependence of the transmission coefficient T_p on $q_p = \beta_p I_{p0} d$. The dashed curve is plotted from Eq. (7.3). The squares, circles, and crosses represent the experimental data for samples 1, 2 and 3, respectively.

we end up with an analytical expression for T_p:

$$T_p = \frac{2}{q_p\sqrt{\pi}} \int_0^\infty \ln\left(1 + q_p e^{-t^2}\right) \mathrm{d}t. \tag{7.3}$$

The transmission coefficient is seen to be determined by a single parameter q_p. Plotted as the dashed curve in Fig. 7.4 is T_p as a function of the variable q_p. The curve has a very unique shape: after a rapid initial fall, the further decrease of T_p occurs very slowly; this is due to the relatively weak energy absorption at the pulse wings. Even for a high nonlinear absorption parameter, $q_p = 100$, about 8% of the incident energy is transmitted.

7.3.3 Experimental results

In Fig. 7.4 we also plot the data previously shown in Fig. 7.2 as squares, circles and crosses; only now the peak intensity I_{p0} is incorporated in the parameter q_p. The data points have been fitted in accor-

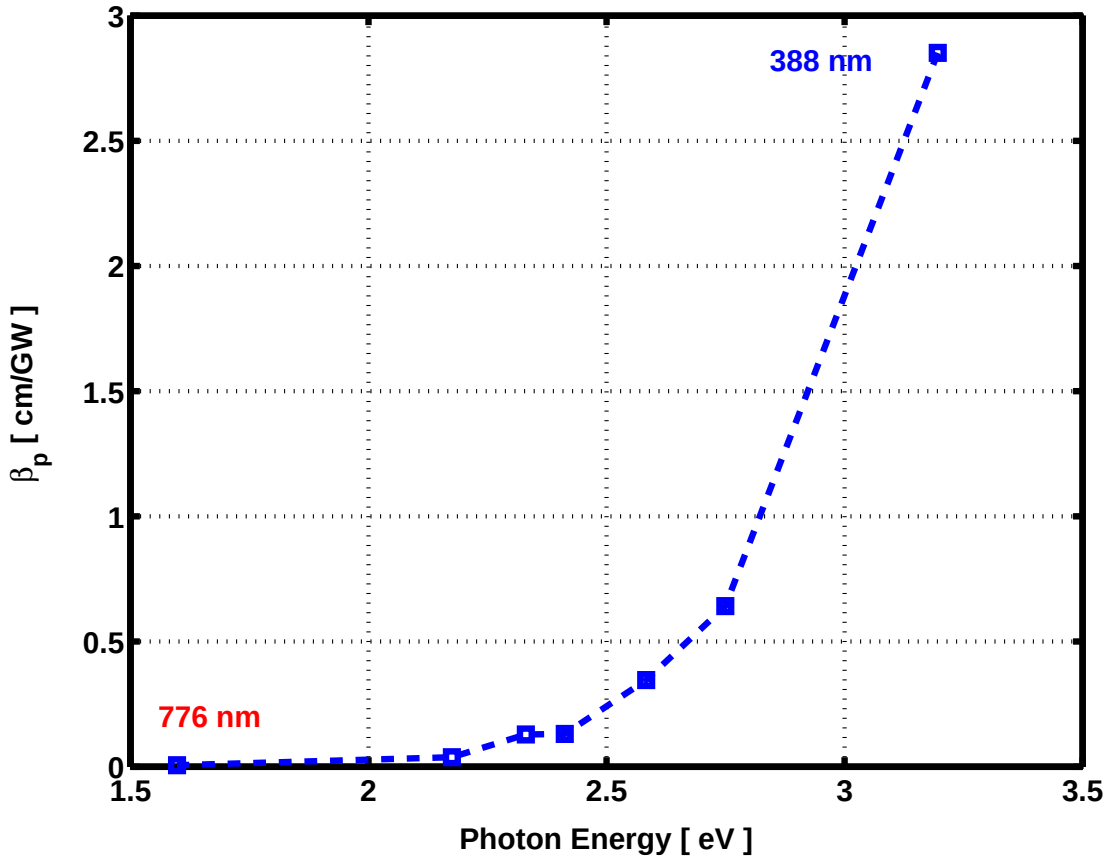

Figure 7.5: The quadratic absorption coefficient β_p of $LiNbO_3$ as function of photon energy.

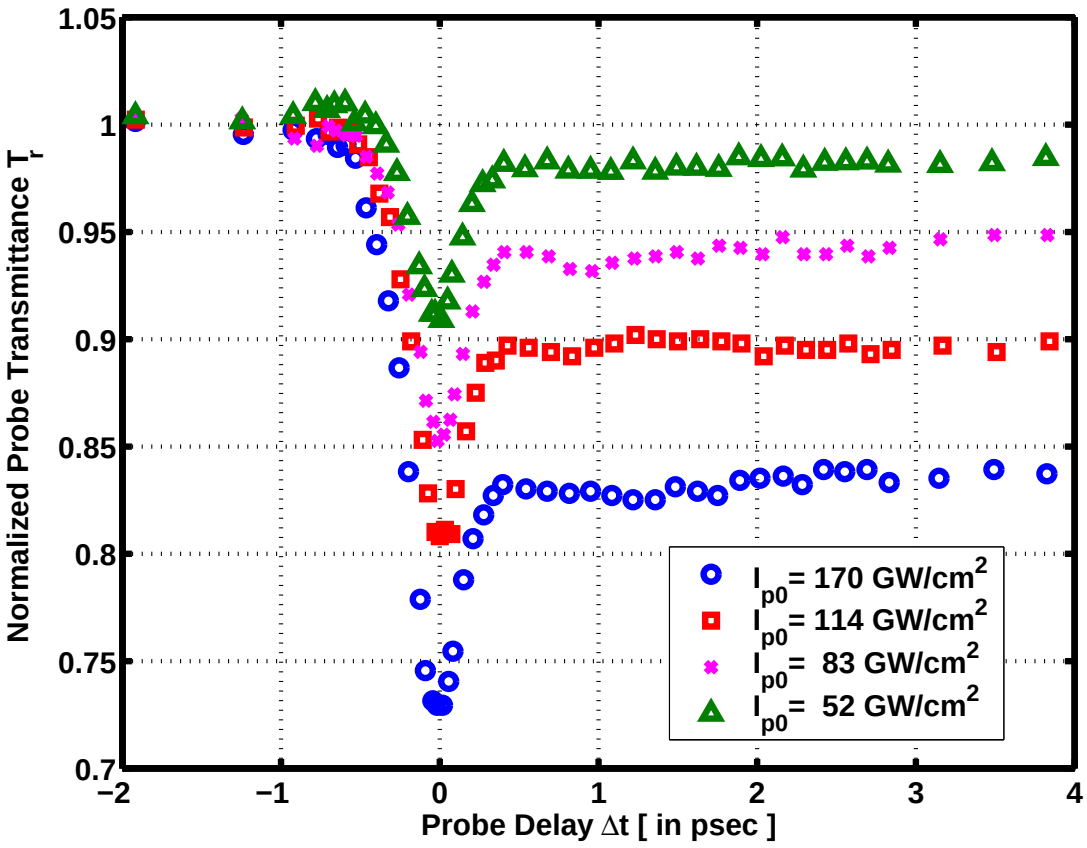

Figure 7.6: Transmission coefficient T_r of the probe pulse versus the time delay Δt for sample 4 and four different values of the pump intensity. The circles, squares, crosses, and triangles correspond to $I_{p0} \sim 52$, 83, 114 and 170 GW/cm^2, respectively.

dance with Eq. (7.3), and the value of β_p for 388 nm thus extracted is 2.85 cm/GW (corresponding to a q_p value of ~ 96). The excellent agreement between the data points and the theoretical curve implies that the two-photon absorption process is indeed the dominant nonlinear effect. In general, the quadratic absorption coefficient should depend on the light polarization. Our experiments have shown, however, that the corresponding difference is fairly small, less than 10%.

We also investigate the wavelength dependence of β_p: femtosecond pulses at five different wavelengths (451 nm, 480 nm, 514 nm, 532 nm and 570 nm) are obtained by passing the seed pulse at 776 nm through a parametric amplifier. The transmission coefficients are measured for all wavelengths, and the values of β_p are fitted just as for the 388 nm pulse. The results are summarized in Fig. 7.5; β_p is plotted as a function of the photon energy in eV. As expected, β_p depends rather strongly on the photon energy: it starts increasing rapidly after ~ 2.2 eV, which agrees well with the fact that the bandgap of $LiNbO_3$ is ~ 4 eV.

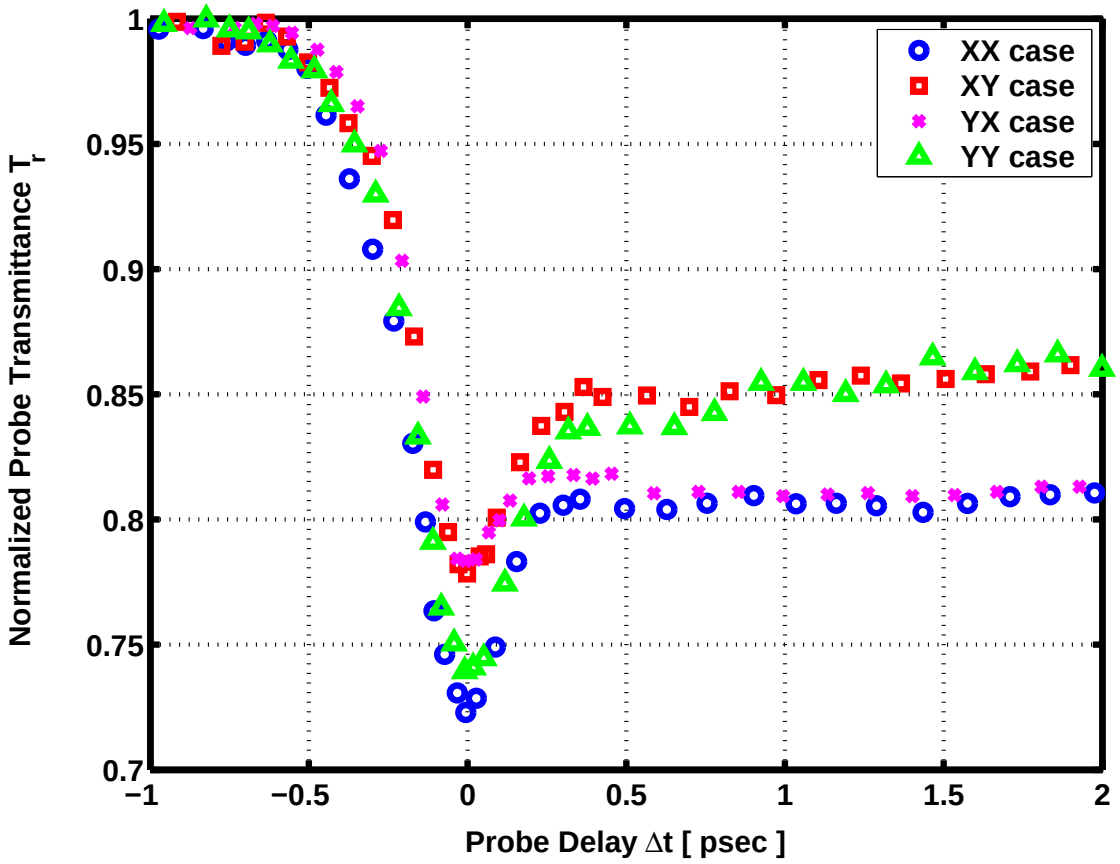

Figure 7.7: Transmission coefficient T_r versus Δt for different combinations of pump and probe polarizations; the first and second characters of each pair in the legend (e.g., "X") specify the orientation of the polarization vector of the pump and probe pulses, respectively.

7.4 Collinear pump-and-probe experiment and modeling

7.4.1 Experimental results

Now that we have a better understanding of the nonlinear absorption process experienced by the pump pulse at λ_p, we can go on to investigate the results obtained with the setup in Fig. 7.1. Shown in Fig. 7.6 is the probe pulse (at λ_r) transmission coefficient T_r as a function of its temporal delay Δt for $LiNbO_3$ sample 4; the dependence is plotted for four different values of the pump pulse intensity. All data have been obtained with both pulses polarized along the x-axis, i.e., ordinarily polarized.

Another set of experimental data are shown in Fig. 7.7, where the dependence $T_r(\Delta t)$ in the same sample for all four possible combinations of pulse polarizations (XX, XY, YX and YY) is plotted, the peak pump intensity I_{p0} being kept constant at ~ 128 GW/cm^2. Pulses polarized along y-axis are extraordinary waves.

We make the following observations based on the experimental data mentioned above:

- The dependence $T_r(\Delta t)$ has two outstanding features: a dip, which supposedly happens near $\Delta t = 0$, and a quasi-permanent "plateau" after the dip. The temporal width of the dip is comparable with that of the pulse.
- The value of $T_r(\Delta t)$ at both the dip and plateau increases with decreasing pump pulse energy.
- A smaller dip transmission T_r^{dip} comes about for parallel-polarized pulses (XX and YY) than for pulses polarized perpendicular to each other.
- The value of T_r at the plateau is determined by the probe polarization; extraordinarily polarized probe experiences a slightly larger plateau transmission $T_r^{pl.}$.

7.4.2 Modeling of collinear pump-and-probe experiment

We attribute the dip manifested by the probe transmission $T_r(\Delta t)$ to the two-photon absorption process involving a pump and a probe photon; the sum of the photon energy in this case is ~ 4.8 eV, which is larger than the band gap of $LiNbO_3$ (~ 4 eV).

On the other hand, the plateau section in the dependence $T_r(\Delta t)$ is attributed to the absorption of the probe pulse by charge carriers (electrons and/or holes) that are excited by the intense pump pulse; the concentration of the excited free carriers due to pump and probe photons is negligible in comparison. The polarization dependence of the plateau value is explained by the anisotropy inherent in the $LiNbO_3$ crystal. We shall model the dip and the plateau sections of $T_r(\Delta t)$ separately in the following.

7.4.2.1 Modeling the dip of $T_r(\Delta t)$

We can write down the following equation for the probe pulse intensity:

$$\left(\frac{\partial}{\partial z} + \frac{1}{v_r}\frac{\partial}{\partial t}\right) I_r = -\beta_r I_p I_r. \tag{7.4}$$

The similarity between Eq. (7.4) and Eq. (7.1) is obvious. The only difference is that the effective absorption coefficient in Eq. (7.4) is $\alpha_r = \beta_r I_p$, which is determined by a much more intense pump pulse, and β_r is the quadratic absorption coefficient characterizing the two-photon absorption participated by a pump and a probe photon. To solve this equation, it helps to make the change of variables

$$\begin{cases} \zeta &= z, \\ \tau &= t - \frac{z}{v_r}, \end{cases}$$

after which Eq. (7.4) becomes

$$\frac{\partial}{\partial \zeta} I_r = -\beta_r I_p I_r,$$

where

$$I_r(x,y,\zeta=0,\tau) = I_{r0}\exp\left[-\frac{(\tau-\Delta t)^2}{t_p^2} - \frac{x^2+y^2}{D_p^2}\right],$$

and

$$I_p(x,y,\zeta,\tau) = \frac{I_{p0}}{\beta_p I_{p0}\zeta + \exp\left[(\frac{\tau}{t_p} - \frac{\delta_0\zeta}{d})^2 + \frac{x^2+y^2}{D_p^2}\right]}.$$

according to Eq. (7.2). In these expressions, Δt is the delay of the probe pulse, and $\delta_0 = (n_p - n_r)d/ct_p$ is the parameter accounting for the difference of pump and probe velocities. We have also assumed that the pump and probe pulses have the same temporal duration and transverse spatial dimension.

The solution of the probe intensity $I_r(x,y,\zeta=d,\tau)$ is therefore

$$\begin{aligned} & I_r(x,y,\zeta=d,\tau) \\ &= I_r(x,y,\zeta=0,\tau)\exp\left[-\int_0^d \beta_r I_p \mathrm{d}\zeta\right] \\ &= I_r(x,y,\zeta=0,\tau)\exp\left\{-\frac{\beta_r}{\beta_p}\int_0^d \frac{q_p \mathrm{d}u}{q_p u + \left[(\frac{\tau}{t_p} - \frac{\delta_0\zeta}{d})^2 + \frac{x^2+y^2}{D_p^2}\right]}\right\}, \end{aligned} \tag{7.5}$$

where $\zeta = ud$ has been used.

The transmitted probe energy can be calculated from Eq. (7.5), and the corresponding transmission coefficient is

$$T_r = \frac{1}{\sqrt{\pi}}\int_{-\infty}^{\infty}\exp\left[-(s-\Delta t/t_p)^2\right]\int_0^1 \exp\left[-\frac{\beta_r}{\beta_p}\int_0^1 \frac{q_p f \mathrm{d}u}{q_p f u + \exp[(s-\delta_0 u)^2]}\right]\mathrm{d}f\mathrm{d}s. \tag{7.6}$$

If we neglect the velocity difference between pump and probe pulses, $\delta_0 = 0$; the integrals involving variables u and f can be carried out analytically, and we obtain from Eq. (7.6)

$$T_r = \frac{e^{-(\Delta t/t_p)^2}}{\sqrt{\pi}aq_p}\int_{-\infty}^{\infty} e^{2s\Delta t/t_p}[(1+q_p e^{-s^2})^a - 1]\mathrm{d}s, \tag{7.7}$$

where $a = 1 - \beta_r/\beta_p$. In our experiment, the transmission at the dip can be approximated as $T_r^{dip} = 1 - T_{r,min} - 1/2[1 - T_r^{pl.}]$, which can then be used for the fitting of β_r.

7.4.2.2 Modeling the plateau of $T_r(\Delta t)$

Since the intense pump pulse excites carriers via direct two-photon transitions, it is able to induce an additional absorption for the probe. This pump-induced absorption is expected to remain until recombination of the photo-excited carriers occurs. To find out the concentration of excited carriers, we refer to Fig. 7.8. We define $\rho_p(x,y,z,t)$ as the electromagnetic energy density carried by the

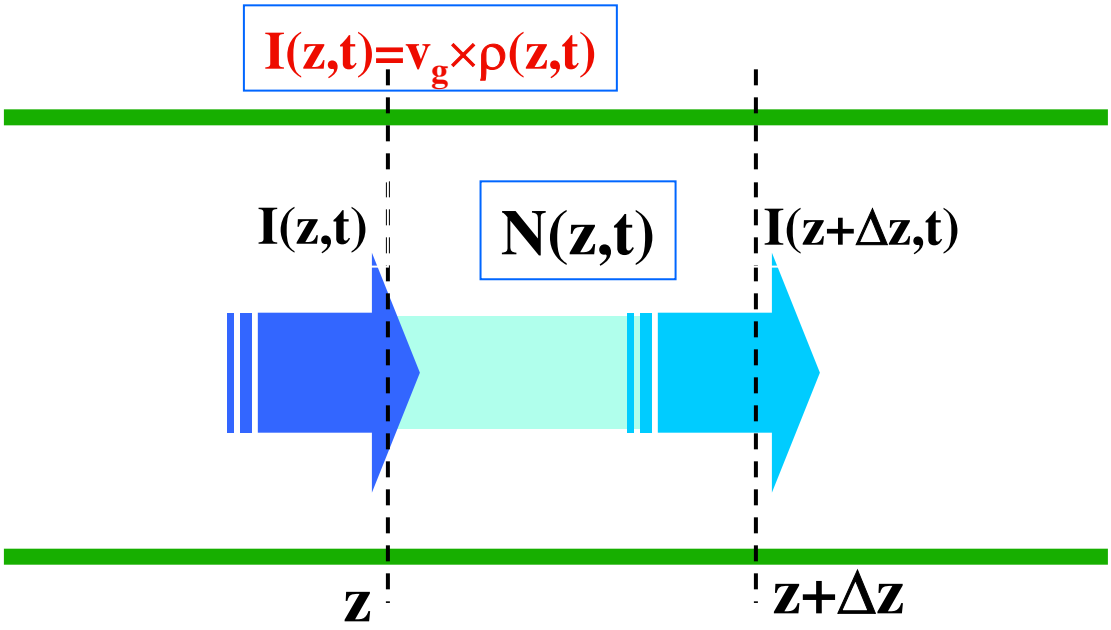

Figure 7.8: The pump pulse is passing through a short segment of nonlinear-absorptive medium.

pump pulse and

$$I_p(x, y, z, t) = v_p \times \rho_p(x, y, z, t).$$

Consider a short segment of length Δz in the medium, as shown in Fig. 7.8. The rate of change of the pulse energy in the length Δz is given by the energy flux into one end minus the energy flux out of the other end of the segment, plus the rate of pulse energy expended on the excitation of free carriers. Let $N(x, y, z, t)$ be the free carrier concentration and neglect the free-carrier recombination; we have

$$\frac{\partial}{\partial t}[\rho_p(z, t)\Delta z] = I_p(z, t) - I_p(z + \Delta z, t) - 2\hbar\omega_p \frac{\partial}{\partial t} N(z, t)\Delta z.$$

After some straightforward manipulations, we end up with

$$\frac{\partial}{\partial \tau} N(x, y, \zeta, \tau) = -\frac{1}{2\hbar\omega_p} \frac{\partial}{\partial \zeta} I_p(x, y, \zeta, \tau). \tag{7.8}$$

According to Eq. (7.8), the absorption coefficient experienced by the probe pulse due to the free carriers can be represented as

$$\alpha_r^f(x, y, \zeta, \tau) = -\frac{\sigma_r}{2\hbar\omega_p} \frac{\partial}{\partial \zeta} \int_{-\infty}^{\tau} I_p(x, y, \zeta, \tau')\mathrm{d}\tau', \tag{7.9}$$

where σ_r is the effective absorption cross-section of the photo-excited carriers at the wavelength λ_r. Combining the probe absorption due to the co-existence of the pump pulse and the excited carriers,

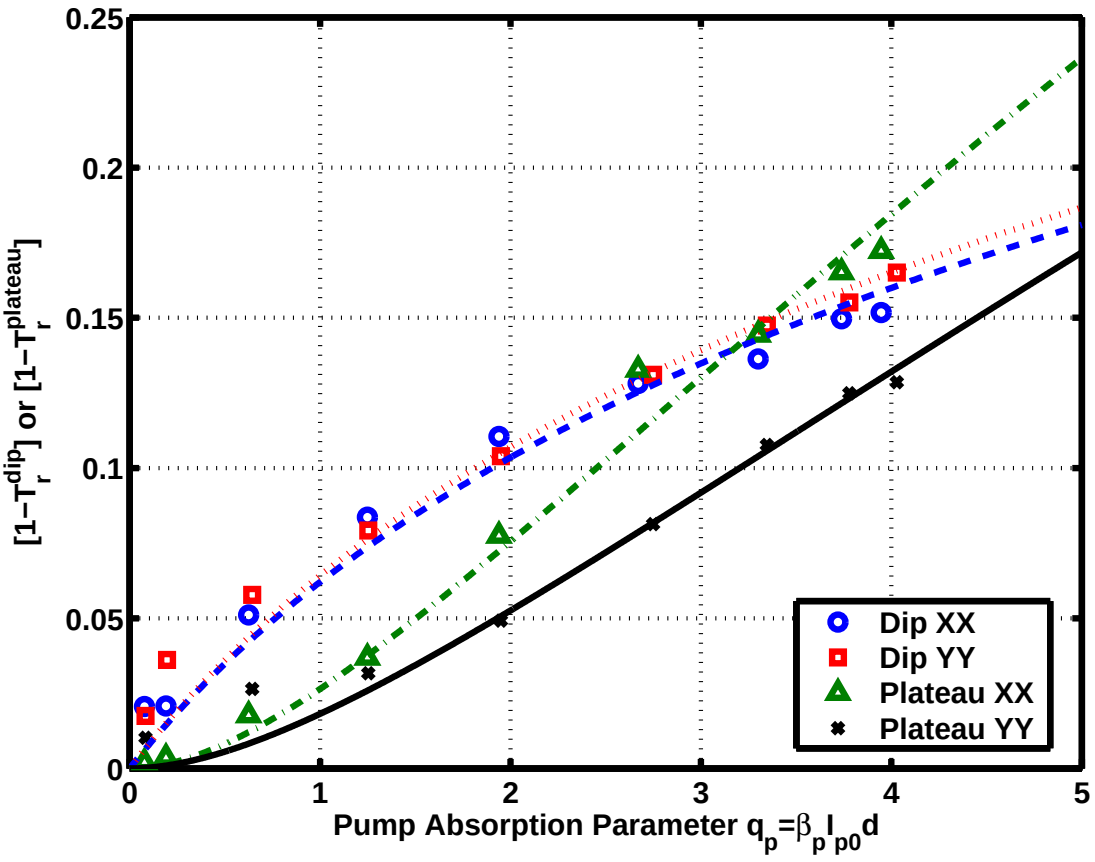

Figure 7.9: Dependence of the dip and plateau amplitudes on the product $q_p = \beta_p I_{p0} d$ for sample 3 and two different pump-probe polarization states. The points are experimental data, and the solid lines are theoretical fits.

we have

$$I_r(x, y, \zeta = d, \tau) = I_r(x, y, \zeta = 0, \tau) \exp\left[-\int_0^d (\beta_r I_p + \alpha_r^f) \mathrm{d}\zeta\right]. \tag{7.10}$$

To compute $T_r^{pl.}$, consider the case when the pump pulse has already passed through, i.e., the probe pulse does not overlap with the pump pulse. Mathematically, we set $I_p = 0$ in Eq. (7.10) and $\tau = \infty$ in Eq. (7.9) and the plateau value is

$$T_r^{pl.} = \int_0^\infty \exp\left[-f - bq_p\left(\frac{\sqrt{\pi}}{2} e^{-f} - \int_0^\infty \frac{\mathrm{d}s}{q_p + e^{f+s^2}}\right)\right] \mathrm{d}f, \tag{7.11}$$

where $b = \sigma_r t_p / \hbar\omega_p \beta_p d$.

7.4.3 Comparison between theory and experiments: the determination of parameters β_r and σ_r

Fig. 7.9 shows the experimental data for the dependence of the dip and plateau amplitudes on the pump absorption parameter q_p, obtained for two different polarization cases, together with the theoretical fit. The fit parameters are the ratio β_r/β_p (for the dip amplitude) and $b = \sigma_r t_p/\hbar\omega_p\beta_p d$ (for the plateau amplitude).

The ratio β_r/β_p deduced from the fitting procedure is ~ 0.23 for the XX case and ~ 0.24 for the YY case. Thus, with an accuracy of $(10 \sim 15)\%$, the value of β_r can be estimated as ~ 0.67 cm/GW. The values of b can be estimated as ~ 0.21 and ~ 0.14 for the XX and YY cases, respectively. This gives us the values of the excitation cross-section: $\sigma_{r,xx} \sim 1.60 \times 10^{-17}$ cm^2 and $\sigma_{r,yy} \sim 1.08 \times 10^{-17}$ cm^2.

7.5 Conclusion

Propagation of high-power femtosecond light pulses in lithium niobate crystals ($LiNbO_3$) is investigated experimentally and theoretically in collinear pump-and-probe transmission experiments. It is found that within a wide intensity range a strong decrease of the pump transmission coefficient at 388 nm fully complies with the model of two-photon absorption; the corresponding nonlinear absorption coefficient is $\beta_p \approx 2.85$ cm/GW. Furthermore, intense pump pulses induce a considerable absorption for a probe pulse at 776 nm. The dependence of the probe transmission coefficient on the time delay Δt between probe and pump pulses is characterized by a narrow dip (at $\Delta t \approx 0$) and a long (on the picosecond time scale) lasting plateau. The dip is due to direct two-photon transitions involving both pump and probe photons; the corresponding nonlinear absorption coefficient is $\beta_r \approx 0.67$ cm/GW. The plateau absorption is caused by the presence of free carriers excited by the pump pulse; the effective absorption cross-section at 776 nm is $\sigma_r \approx 1.60 \times 10^{-17}$ cm^2. The above nonlinear absorption parameters are not strongly polarization sensitive. No specific manifestations of the relaxation of hot carriers are found for a pulse duration of about 0.22 ps. From the obtained results it becomes clear that two-photon absorption will strongly affect holographic recording in $LiNbO_3$ with ultrashort intense light pulses.

Bibliography

[1] K. Miura, J. R. Qiu, H. Inouye, T. Mitsuyu, and K. Hirao. Photowritten optical waveguides in various glasses with ultrashort pulse laser. *Applied Physics Letters*, 71(23):3329–3331, December 1997.

[2] J. D. Mills, P. G. Kazansky, E. Bricchi, and J. J. Baumberg. Embedded anisotropic microreflectors by femtosecond-laser nanomachining. *Applied Physics Letters*, 81(2):196–198, July 2002.

[3] Y. Shimotsuma, P. G. Kazansky, J. R. Qiu, and K. Hirao. Self-organized nanogratings in glass irradiated by ultrashort light pulses. *Physical Review Letters*, 91(24):247405, December 2002.

[4] P. G. Kazansky, H. Inouye, T. Mitsuyu, K. Miura, J. Qiu, K. Hirao, and F. Starrost. Anomalous anisotropic light scattering in Ge-doped silica glass. *Physical Review Letters*, 82(10):2199–2202, March 1999.

[5] R. DeSalvo, A. A. Said, D. J. Hagan, E. W. VanStryland, and M. SheikBahae. Infrared to ultraviolet measurements of two-photon absorption and n(2) in wide bandgap solids. *IEEE Journal of Quantum Electronics*, 32(8):1324–1333, August 1996.

[6] A. Dragonmir, J. G. McInerney, and D. N. Nikogosyan. Femtosecond measurements of two-photon absorption coefficients at λ=264 nm in glasses, crystals, and liquids. *Applied Optics*, 41(21):4365–4376, July 2002.

[7] H. J. Eichler, P. Günter, and D. W. Pohl. *Laser-Induced Dynamic Gratings*. Springer-Verlag, New York, 1986.

[8] A. L. Smirl, G. C. Valley, K. M. Bohnert, and T. F. Boggess. Picosecond photorefractive and free-carrier transient energy-transfer in GaAs at 1 μm. *IEEE Journal of Quantum Electronics*, 24(23):289–303, February 1988.

[9] G. C. Valley, J. Dubard, and A. L. Smirl. Theory of high-gain transient energy-transfer in GaAs and Si. *IEEE Journal of Quantum Electronics*, 26(6):1058–1066, June 1990.

[10] M. Centini, C. Sibilia, M. Scalora, G. D'Aguanno, M. Bertolotti, M. J. Bloemer, C. M. Bowden, and I. Nefedov. Dispersive properties of finite, one-dimensional photonic band gap structures:

applications to nonlinear quadratic interactions. *Physical Review E*, 60(4):4891–4898, October 1999.

[11] H. J. Coufal, D. Psaltis, and G. T. Sincerbox. *Holographic Data Storage*. Springer-Verlag, New York, 2000.

[12] P. Boffi, D. Piccinin, and M. C. Ubaldi. *Infrared Holography for Optical Communications*. Springer-Verlag, New York, 2003.

[13] G. A. Rakuljic and V. Leyva. Volume holographic narrow-band optical filter. *Optics Letters*, 18:459–461, March 1993.

[14] S. Breer and K. Buse. Wavelength demultiplexing with volume phase holograms in photorefractive lithium niobate. *Applied Physics B*, 66:339–345, March 1998.

[15] J. P. Meyn and M. M. Fejer. Tunable ultraviolet radiation by second-harmonic generation in periodically poled lithium tantalate. *Optics Letters*, 22(16):1214–1216, August 1997.

Chapter 8

Femtosecond recording of spatial gratings and time-resolved readout in lithium niobate

8.1 Introduction

Ferroelectric lithium niobate is one of the most investigated man-made materials for its widespread and promising applications in integrated and nonlinear optics[1], e.g., parametric amplification, second harmonic generation[2] (SHG) and periodically-poled lithium niobate[3] (PPLN). Its superior photorefractive property[4], which is characterized by the change in refractive index resulting from the optically induced redistribution of electrons and/or holes and the linear electro-optic effect[5], has made lithium niobate ($LiNbO_3$) an extremely attractive candidate for many applications such as holographic data storage, optical information processing, phase conjugation, beam steering, telecommunication switching and WDM filters[6, 7, 8, 9], just to name a few.

The photorefractive effect is a peculiar form of the (second-order) optical nonlinearity in the sense that it cannot be described by a nonlinear susceptibility $\chi^{(n)}$ that is utilized extensively to characterize almost all optical nonlinearities; this peculiarity comes from the fact that the induced index change in photorefractive materials is not an instantaneous effect proportional to the product of participating light intensities but a delayed response depending on such diverse parameters as sample doping impurities, dopant concentration and oxidation/reduction states, grating period, photovoltaic effect, light intensity, etc.

The distinction between the photorefractive effect and the other inherent nonlinearities will need to be addressed when the holographic recording is performed with high-intensity laser pulses. Grating-recording experiments have been conducted extensively in lithium niobate in the past few decades at low-intensity ($\leq 10^3$ W/m^2), mainly associated with continuous-wave laser, and high-intensity (up to $\sim 10^{11}$ W/m^2) made possible by nanosecond pulses[10, 11]. Jermann and Otten[10]

made use of the two-center model to successfully explain the increased recording sensitivity and saturation value of the index modulation at elevated recording light intensity. At these intensity levels, the photorefractive effect is still the dominant nonlinear effect; however, it is conceivable that holographic recording with even more intense (picosecond or even shorter) pulses will inevitably enhance and reveal other nonlinear material responses.

Picosecond pulses with peak intensity 10^{12} to 10^{13} W/m^2 have been used to investigate the photorefractive and beam-coupling effects in various materials, e.g., GaAs[12, 13, 14], BSO ($Bi_{12}SiO_{20}$)[15], barium titanate ($BaTiO_3$)[16], potassium niobate ($KNbO_3$)[17], etc. These experiments are conducted with pump-probe techniques that include two intense, interfering pump pulses responsible for establishing index and/or absorption gratings and a weak, Bragg-matched probe pulse that gets diffracted by the grating. The measured responses consist of an initial instantaneous peak followed by a permanent ("left-over") photorefractive grating. The source of the initial peaks remains ambiguous owing to the temporal resolution limit in these experiments. Among various possible contributing mechanisms to the initial diffraction peak are degenerate four-wave mixing (due to instantaneous third-order nonlinearity) and free carrier gratings (due to modulated concentration of excited charge carriers).

In this chapter we will employ femtosecond pulses with peak intensity up to 3×10^{15} W/m^2 to pump and probe $LiNbO_3$ samples. Enhanced temporal resolution in the experiment and accumulated knowledge from the previous two chapters enable us to draw conclusions from the observed phenomena and help shed light on the involved nonlinear processes.

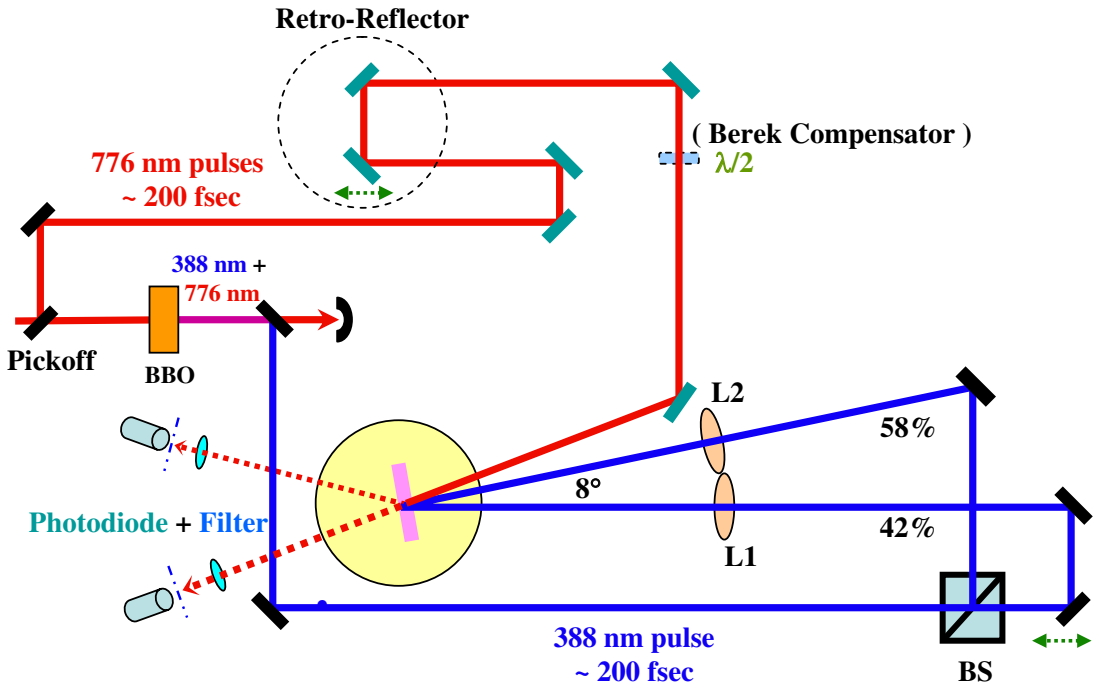

Figure 8.1: Schematic illustration of the holographic pump-and-probe setup in $LiNbO_3$. The pump pulses are polarized perpendicular to the surface of the optical table. The Berek compensator serves as a half-wave plate for the probe pulse; the retro-reflector is mounted on a translation stage (resolution 1 μm); BS: beam splitter; DS: probe delay stage; L: lens.

8.2 Experimental observation

8.2.1 Experimental setup

The experimental pump-and-probe setup is illustrated in Fig. 8.1. An axially symmetric pulse at $\lambda_r = 776$ nm is obtained from a Ti:Sapphire amplified laser system CPA-2010 from Clark-MXR, Inc. The temporal and spatial FWHM of the pulse intensity are measured to be 0.22 psec and 3.5 mm, respectively. Four percent of the pulse energy is tapped and serves as the probe pulse displaced by a variable delay stage. The rest of the pulse is passed through a 1-mm-thick BBO ($\beta - BaB_2O_4$) crystal to generate a pulse at $\lambda_p = 388$ nm, which is split into two identical pump pulses and then focused down to one-fifth of their original diameter inside the 1-mm-thick lithium niobate ($LiNbO_3$) sample. The angle between the pump pulses $2\theta_p$ outside the sample is 8°. The peak intensity of each of the pump pulses inside the sample is about 165 GW/cm^2; the maximum pump pulse fluence is ~ 40 mJ/cm^2. The probe pulse is incident at its Bragg angle, and the diffracted probe is detected by a photodiode, in front of which a polarizer is used to extract the desired polarization. The natural angular separation between the four pulses minimizes the signal-to-noise ratio in the measurements. The optimal overlap of the pulses is obtained by maximizing the detected diffracted pulse energy.

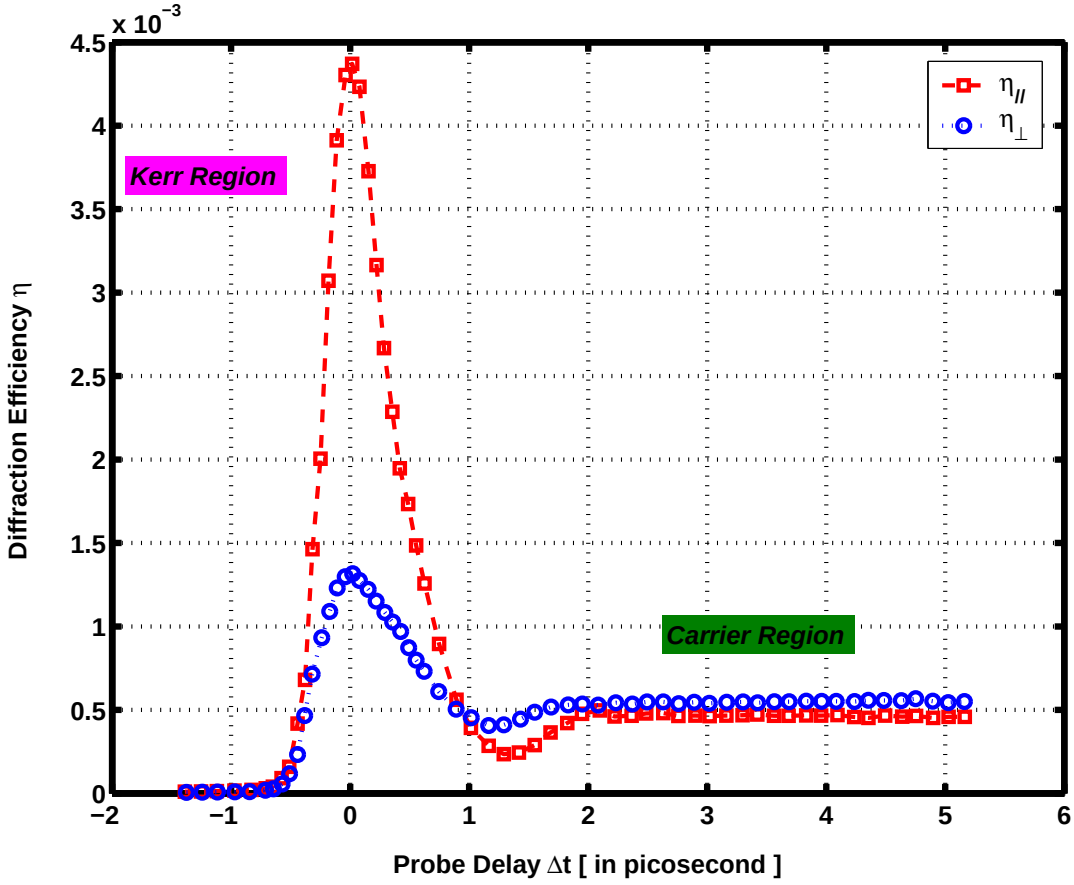

Figure 8.2: The measured diffraction efficiency η as a function of the probe delay Δt in an undoped $LiNbO_3$ sample.. The pump pulses are polarized along the c-axis and $\eta_{\|}(\eta_{\perp})$ is measured when the probe pulses are polarized parallel (perpendicular) to those of the pump pulses.

8.2.2 Polarization dependence

The polarization dependence of the measured diffraction efficiency η is shown in Fig. 8.2, where two configurations denoted by $\eta_{\|}$ (in squares) and $\eta_{\perp}$ (in circles) are plotted. The experiment is carried out with the c-axis of a undoped $LiNbO_3$ crystal orientated parallel to the polarization of the pump pulses. The data of $\eta_{\|}(\eta_{\perp})$ are acquired when the polarization of the probe pulses, adjusted with the help of the Berek compensator and a polarizer in front of the photo-detector, is parallel (perpendicular) to that of the pump pulses. The position of the origin $\Delta t = 0$ is determined by quadratically fitting the three data points corresponding to the highest measured diffraction efficiencies; the origin is then assigned the position where the fitted maximum occurs (since the material response is assumed to be instantaneous[5]). Every data point corresponds to the value of the measured diffraction efficiency averaged over 100 single-pulse experiments: after each pump-and-probe measurement, uniform illumination is applied to erase the remnant photorefractive grating.

Both curves in Fig. 8.2 show a very distinctive set of features when the probe delay Δt is gradually increased:

1. The diffraction efficiency increases rapidly toward a peak value (η_{peak}), which occurs when the probe pulses supposedly has the maximum overlap with the pump pulses. The value of $\eta_{peak,\|}$ is significantly larger than $\eta_{peak,\perp}$, about 3 times.

2. After it has peaked, the diffraction efficiency then decreases rapidly, albeit at a less steep rate than when it ascends.

3. When $\Delta t \geq 2$ picosecond, the value of η remains constant at a "plateau" value $\eta_{pl.}$ well into almost 1 nanosecond. The value of $\eta_{pl.,\|}$ is only slightly smaller than that of $\eta_{pl.,\perp}$.

4. The transition between the descending η and the constant η is a very interesting "valley" region between $\Delta t = 1$ and 2 picosecond; i.e., η dips under $\eta_{pl.}$ and then climbs back to the $\eta_{pl.}$ level.

A detectable permanent photorefractive grating is present after the illumination of a few pump pulses without erasure; this grating can be easily erased with a uniform light source. Uniform illumination after each pump-and-probe attempt ensures a clean slate for the next measurement.

Based on the experiments done in and knowledge accumulated from the previous two chapters, we attribute the diffracted probe pulse around η_{peak} to the instantaneous mixed grating as a result of the Kerr effect and two-photon absorption involving both the pump and probe photons. On the other hand, the semi-permanent component $\eta_{pl.}$ is associated with the carriers excited by the intense pump pulses. The concentration of the carriers is modulated after the interfering pump pulses and therefore constitute another mixed grating by which the much delayed probe pulse gets diffracted.

The "valley" feature of η has to be a joint product of the two mixed gratings. A little thought points to the "negative" index of the carrier grating. The "valley" can only be present when the two index gratings due to the Kerr effect and excited carriers cancel each other; after the Kerr index grating disappears, η slightly increases to the $\eta_{pl.}$ level. At the bottom of the η valley, the two index gratings cancel each other completely, and the diffracted energy is dedicated to the two absorption gratings, which are additive.

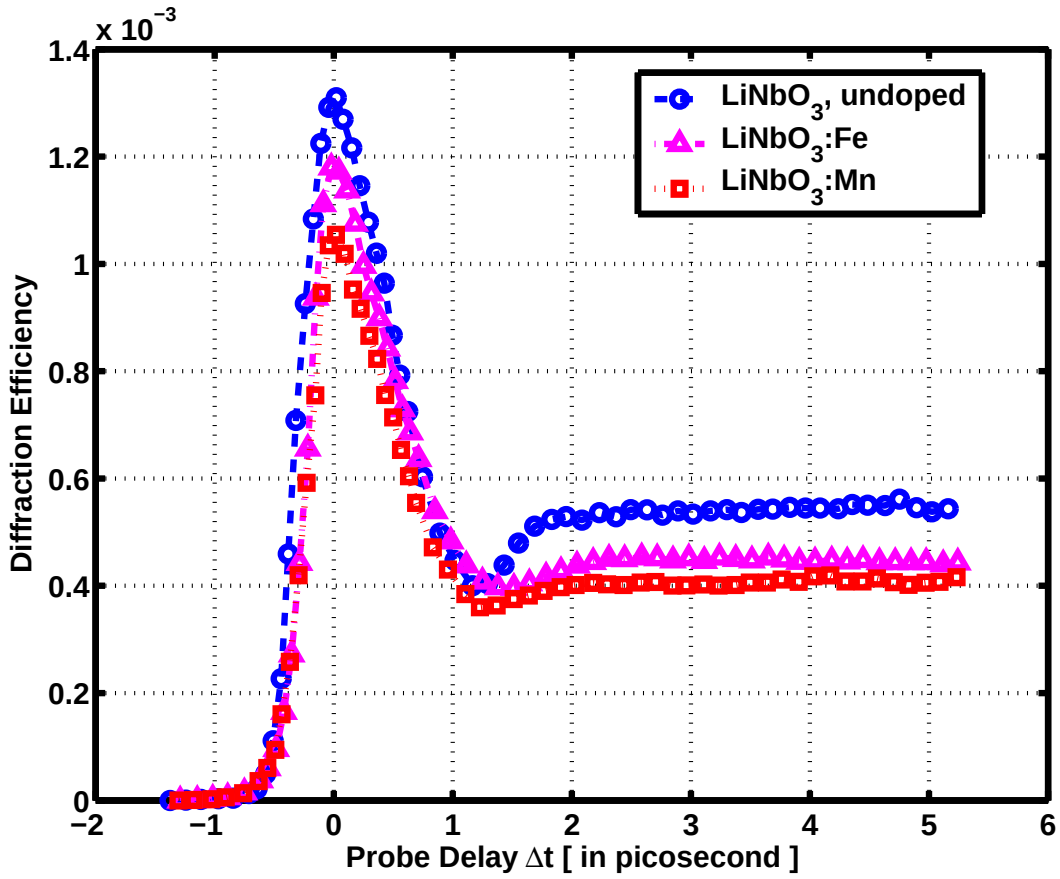

Figure 8.3: The measured diffraction efficiency η as a function of the probe delay Δt in undoped (circles), iron-doped (triangles) and manganese-doped (squares) $LiNbO_3$ samples. The pump pulses are polarized along the c-axis, and all measurements are carried out in the $\eta_\perp$) configuration.

8.2.3 Dependence on dopants

In Fig. 8.3, the experimental data of $\eta(\Delta t)$ for an undoped and two impurity-doped $LiNbO_3$ crystals are plotted together for comparison. The doped impurities do not strongly influence the behavior in the pump-and-probe experiment, which corroborates that the probe pulse is diffracted because of the intrinsic attributes present in the $LiNbO_3$ matrix rather than mechanisms brought about by dopants or impurities.

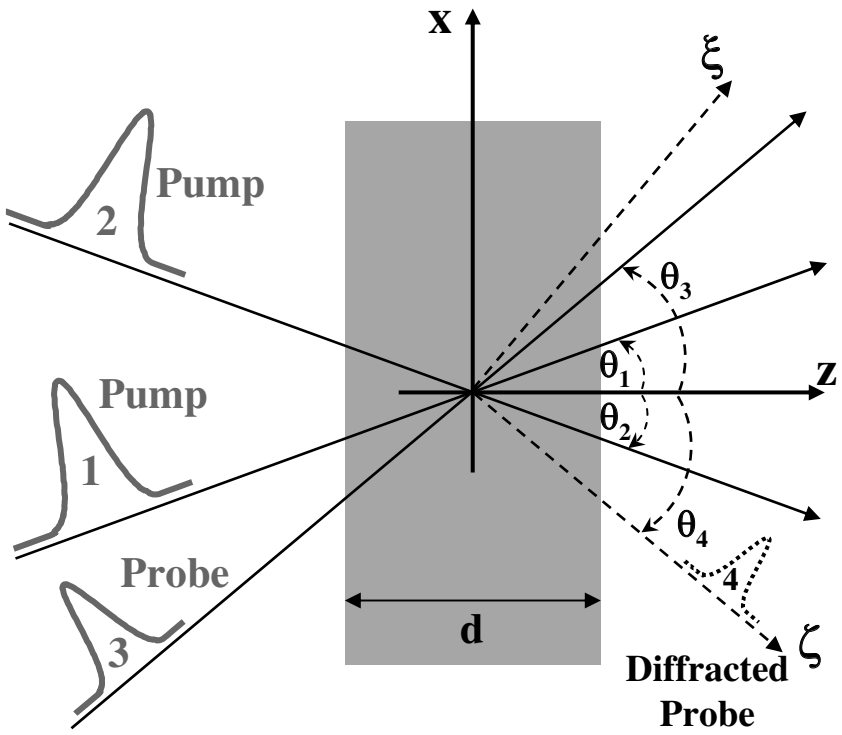

Figure 8.4: Configuration of the femtosecond holographic experiment in lithium niobate; 1 and 2 are the pump (recording) pulses, while 3 and 4 are the probe and diffracted pulses.

8.3 Theoretical justification and comparison with experimental data

In Fig. 8.4, the interference between the two intense pump pulses results in a modulated intensity pattern:

$$I(x,y,z,t) = I_1 + I_2 + 2\sqrt{I_1 I_2}\cos Kx.$$

The intensities of these pulses inside lithium niobate can therefore be described by the following nonlinear coupled equations:

$$\left(\mathbf{s_1}\cdot\nabla + \frac{1}{v_p}\frac{\partial}{\partial t}\right) I_1 = -\beta_p I_1\left(I_1 + I_2 + 2\sqrt{I_1 I_2}\cos Kx\right), \tag{8.1a}$$

$$\left(\mathbf{s_2}\cdot\nabla + \frac{1}{v_p}\frac{\partial}{\partial t}\right) I_2 = -\beta_p I_2\left(I_1 + I_2 + 2\sqrt{I_1 I_2}\cos Kx\right), \tag{8.1b}$$

where β_p is the material nonlinear absorption coefficient at 388 nm. As seen by the probe pulse 3, the modulated intensity pattern $I(x,y,z,t)$ gives rise to a mixed grating, which comprises the following components:

1. An index modulation

$$\Delta n(x,y,z,t)\cos Kx = 2n_2\sqrt{I_1 I_2}\cos Kx$$

owing to the optical Kerr effect; here $K = 2k_1 \sin\theta_1$, and n_2 is the appropriate Kerr coefficient.

2. An absorption grating

$$\alpha + \Delta\alpha(x,y,z,t)\cos Kx = \beta_r\left(I_1 + I_2 + 2\sqrt{I_1 I_2}\cos Kx\right)$$

owing to the two-photon transition involving pump and probe photons; here β_r is the corresponding nonlinear absorption coefficient, and α and $\Delta\alpha$ are absorption constants applicable to the pulse intensity.

The probe pulse gets diffracted by this mixed grating and coupled into the diffracted pulse 4; the amplitudes of these two pulses obey the following coupled mode equations when the Bragg condition is satisfied:

$$\left(\mathbf{s_3}\cdot\nabla + \frac{1}{v_r}\frac{\partial}{\partial t}\right)A_3 = -\frac{\alpha}{2}A_3 - j\kappa A_4, \tag{8.2a}$$

$$\left(\mathbf{s_4}\cdot\nabla + \frac{1}{v_r}\frac{\partial}{\partial t}\right)A_4 = -\frac{\alpha}{2}A_4 - j\kappa A_3, \tag{8.2b}$$

where v_r is the group velocity of the probe pulse and

$$\kappa = \frac{\pi\Delta n}{\lambda_r} - j\frac{\Delta\alpha}{4} \tag{8.3}$$

is the coupling constant as a result of the mixed grating.

8.3.1 Decoupling of pump pulses when $q_p = 2\beta_p I_{p0} d \leq 1$

To simplify the computations, we consider the case when the initial peak pump intensities I_{p0} satisfy $2\beta_p I_{p0} d \leq 1$; in this case, the coupling effects between the pump pulses as described by Eqs. (8.1a) and (8.1b) become unimportant, and we can solve analytically for the pump pulses subject to the condition that they possess Gaussian profiles before entering the nonlinear medium:

$$I_i(x,y,z,t) = \frac{I_{p0}}{2\beta_p I_{p0}\left(z+\frac{d}{2}\right)\sec\theta_i + \exp\left[\frac{\left(t-\frac{z\cos\theta_i + x\sin\theta_i}{v_p}\right)^2}{\tau_p^2} + \frac{(x\cos\theta_i - z\sin\theta_i)^2 + y^2}{D_p^2}\right]}, \tag{8.4}$$

where $i = 1, 2$ and τ_p and D_p are the parameters characterizing the pulses' temporal and spatial widths.

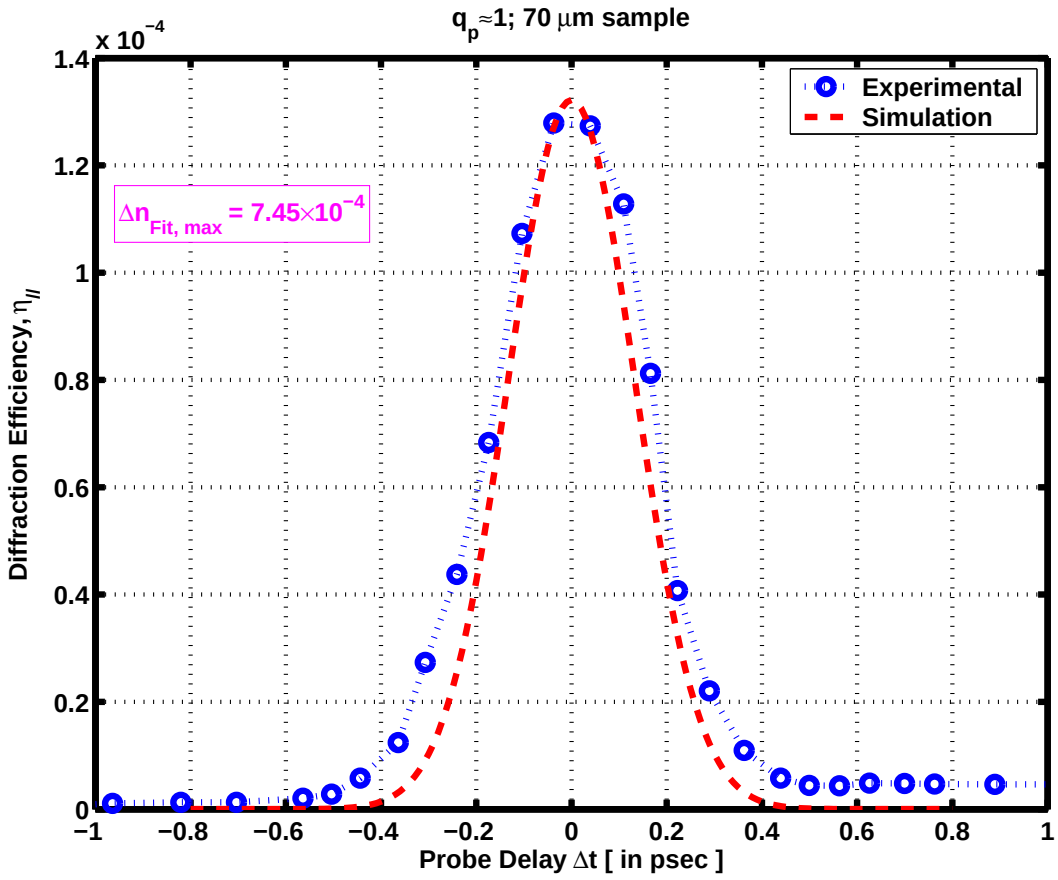

Figure 8.5: Pump-and-probe data acquired for $q_p \approx 1$ in a $LiNbO_3 : Fe$ sample with thickness 70 μm. The circles denote the experimental data, and the dashed curve is the theoretical diffraction efficiency plotted according to Eq. (8.6) for $n_2 = 1.79 \times 10^{-5}$ cm^2/GW.

8.3.2 Curve-fitting and the extracted Kerr coefficient of $LiNbO_3$

When the condition $q_p \leq 1$ is satisfied, the pump pulses undergo negligible mutual coupling and the free carrier grating component contributing to the plateau diffraction efficiency observed in Figs. 8.2 and 8.3 can be ignored compared to the peak diffraction efficiency. Under the assumption of undepleted probe pulse, we can make use of Eq. (8.2b) alone to solve for the amplitude of the diffracted pulse. After the following change of variables

$$\begin{aligned} \zeta &= z\cos\theta_4 + x\sin\theta_4, \\ \xi &= x\cos\theta_4 - z\sin\theta_4, \\ \tau &= t - \frac{z\cos\theta_4 + x\sin\theta_4}{v_r}, \end{aligned}$$

Eq. (8.2b) turns into

$$\frac{\partial}{\partial\zeta}A_4(\xi,y,\zeta,\tau) = -j\kappa(\xi,y,\zeta,\tau)A_3(\xi,y,\zeta,\tau),$$

where the coupling constant κ only consists of the instantaneous components (namely, Kerr effect and nonlinear absorption of the probe photons at the presence of pump photons).

The boundary condition $A_4\left(\zeta = -\frac{d}{2}\sec\theta_4 + \xi\tan\theta_4\right) = 0$ leads to the solution at the exit boundary $z = d/2$:

$$A_4\left(\xi,y,\zeta = \frac{d}{2}\sec\theta_4 + \xi\tan\theta_4,\tau\right) = -\left[\frac{\beta_r}{2} + j\frac{2\pi n_2}{\lambda_r}\right]\int\limits_{-\frac{d}{2}\sec\theta_4+\xi\tan\theta_4}^{\frac{d}{2}\sec\theta_4+\xi\tan\theta_4}\sqrt{I_1 I_2}A_3\mathrm{d}\zeta, \tag{8.5}$$

where the pump pulse profiles from Eq. (8.4) are used.

The amplitude of the probe pulse temporally delayed by Δt can be represented as

$$A_3(\xi,y,\zeta,\tau) = \sqrt{I_{30}}\exp\left\{-\frac{[\tau-\Delta t-(\zeta\cos\alpha_3-\zeta+\xi\sin\alpha_3)/v_r]^2}{2\tau_r^2} - \frac{(\xi\cos\alpha_3-\zeta\sin\alpha_3)^2+y^2}{2D_r^2}\right\},$$

where $\alpha_3 = \theta_3 - \theta_4$ and τ_r and D_r characterize the probe pulse's temporal and spatial widths. Now we can compute the diffraction efficiency, which is defined as the energy ratio between the diffracted pulse and transmitted pulse:

$$\eta(\Delta t) = \frac{\iiint_{-\infty}^{\infty}|A_4(\zeta = \frac{d}{2}\sec\theta_4 + \xi\tan\theta_4)|^2\mathrm{d}\xi\mathrm{d}y\mathrm{d}\tau}{\pi\sqrt{\pi}\tau_p D_p^2 I_{30}}. \tag{8.6}$$

The diffraction efficiency as expressed by Eq. (8.6) is derived for the case $q_p \leq 1$. To achieve $q_p \leq 1$ experimentally, we replace the thick (1-mm) sample with a thin (70-μm) $LiNbO_3 : Fe$ sample (sample 4 as in the previous chapter, with $c_{Fe} \approx 5.6\times10^{19}$ cm^{-3} and a linear absorption coefficient $\alpha_0 \approx 15$ cm^{-1} at 388 nm) and attenuate the pump pulse with a proper neutral density filter, bringing the value of the nonlinear absorption parameter q_p down to ~ 1.

The data obtained from pumping and probing the thin sample are shown as circles in Fig. 8.5; the polarizations of both the pump and probe pulses are parallel to the c-axis of the $LiNbO_3$ crystal. As evident from the figure, we have negligible plateau diffraction efficiency from the excited free carriers; the peak diffraction efficiency can be attributed to the mixed grating characterized by the two material constants β_r and n_2. The value of β_r in this configuration has been extracted from the collinear pump-and-probe experiment to be ~ 0.67 cm/GW. With only n_2 as an unknown for Eq. (8.6), it is straightforward to find its value from Fig. 8.5.

The peak diffraction efficiency can be interpolated from the experimental data by quadratically fitting the data points corresponding to the three maximum $\eta(\Delta t)$ values, producing $\eta_{peak} \approx 1.34\times$

10^{-4}. The dashed curve in Fig. 8.5 is plotted by setting

$$\sqrt{\left(\frac{\pi n_2}{\lambda_r}\right)^2 + \left(\frac{\beta_r}{4}\right)^2} I_{p0} \approx 15 \text{ cm}^{-1},$$

which results in a peak diffraction efficiency $\eta(\Delta t = 0) = \eta_{peak}$. Substituting $\beta_r = 0.67$ cm/GW, we end up with $n_{2,\parallel} \approx 1.79 \times 10^{-5}$ cm^2/GW for $LiNbO_3$.

The index grating arising from the Kerr effect accounts for almost 95% of the peak diffraction efficiency $\eta(\Delta t = 0)$, which agrees well with the polarization dependence shown in Fig. 8.2: the dramatic polarization dependence of $\eta(\Delta t)$ is an obvious manifestation of the dominant role the Kerr grating plays in the mixed grating since in both cases the absorption gratings have approximately equal strengths. As a result, the other Kerr coefficient of interest $n_{2,\perp}$ can be approximated as $\approx 1.12 \times 10^{-5}$ cm^2/GW.

8.3.3 Mixed grating due to the excited carriers

In addition to the instantaneous mixed grating, a permanent mixed grating attributed to the excited carriers also exists. To calculate $\eta_{pl.}$, we consider the case when the probe pulse is much delayed and has little overlap with the pump pulses. In Fig. 8.5, a probe delay Δt of 0.6 psec will suffice. As in the previous section, we take advantage of the condition $q_p \leq 1$; neglecting the DC term α, Eq. (8.2b) becomes

$$\left(\mathbf{s_4} \cdot \nabla + \frac{1}{v_r}\frac{\partial}{\partial t}\right) A_4 = -\left[j\frac{\pi}{\lambda_r}\frac{\varrho_r}{\hbar\omega_p} + \frac{\sigma_r}{4\hbar\omega_p}\right] \frac{\partial}{\partial z}\left(\int_{-d/2}^{d/2}\int_{-\infty}^{\infty} \sqrt{I_1 I_2}\mathrm{d}\tau\mathrm{d}z\right) A_3, \tag{8.7}$$

where σ_r is the effective absorption cross section of the excited carriers and the parameter ϱ_r (having the unit of volume) characterizes the index change due to the excited carriers at the probe wavelength λ_r. A negative index change results in a negative ϱ_r.

To have an estimation of the value of $\eta_{pl.}$, we adopt the approximation: $\theta_1 = \theta_2 = \theta_3 = \theta_4 = 0$, which is reasonable near the paraxial region. The plateau diffraction efficiency is then calculated from Eq. (8.7):

$$\eta_{pl.} \approx \frac{4\sqrt{2}}{25}\left(\frac{\tau_p I_{p0}}{\hbar\omega_p}\right)^2 \left(\frac{\pi^2\varrho_r^2}{\lambda_r^2} + \frac{\sigma_r^2}{16}\right)\mathcal{J}, \tag{8.8}$$

where the definite integral

$$\mathcal{J} = \int_0^\infty e^{-\frac{s}{25}}\left[\frac{\sqrt{\pi}}{2}e^{-s} - \int_0^\infty \frac{\mathrm{d}\tau}{q_p + e^{s+\tau^2}}\right]^2 \mathrm{d}s,$$

and it can be numerically evaluated to be $\sim 3.23842 \times 10^{-2}$ for $q_p = 0.9$, which corresponds to the data shown in Fig. 8.5. The diffraction efficiency in this case is $\eta_{pl.} = 4.8 \times 10^{-6}$; we know

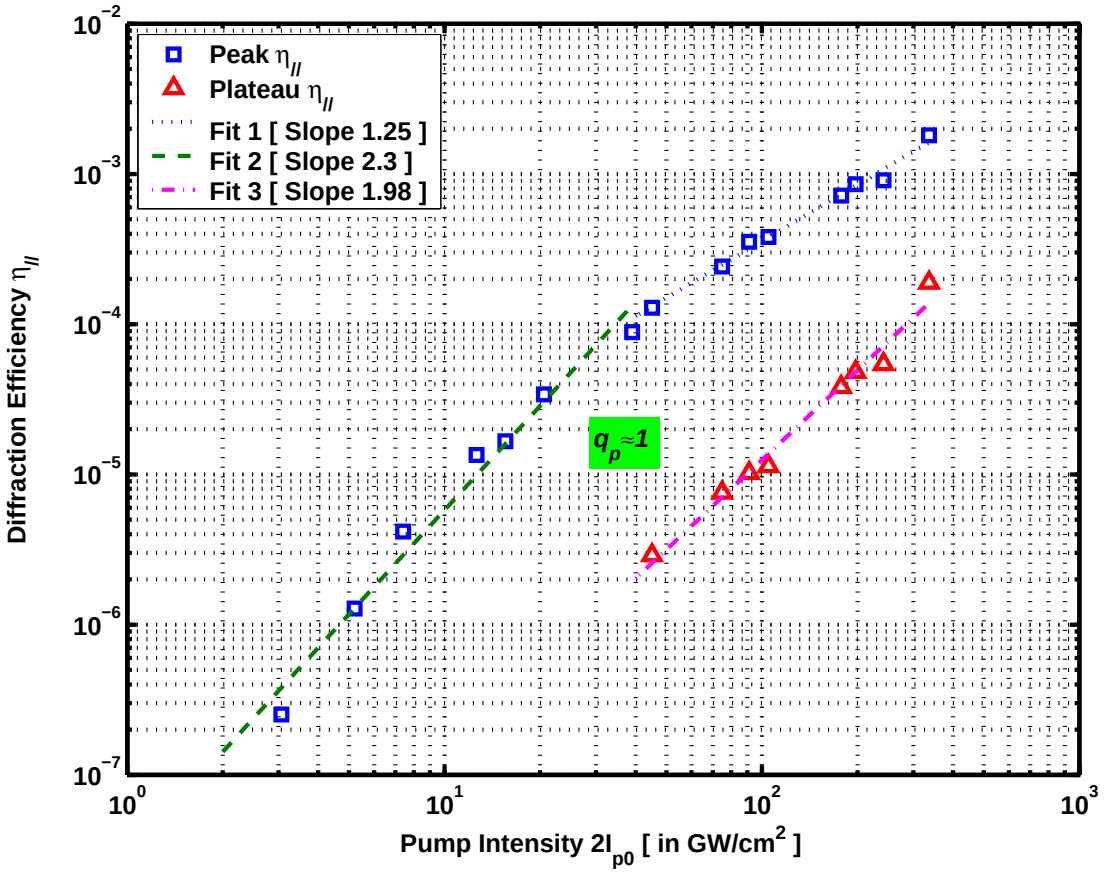

Figure 8.6: The summary of measured values of η_{peak} (in squares) and $\eta_{pl.}$ (in triangles) for different pump intensities in the 70-μm $LiNbO_3$ sample. The pump pulses are polarized along the c-axis, and all measurements are carried out in the $\eta_{\|}$) configuration.

$\sigma_{r,\|} = 1.08 \times 10^{-17}$ cm^2 from the previous chapter and therefore we obtain $\varrho_{r,\|} \approx -8.6 \times 10^{-23}$ cm^3 ($\pm 7\%$, which is the standard deviation normalized to the mean of 40 data points). In this configuration, the contributions to $\eta_{pl.,\|}$ from the index and absorption gratings are $\sim 62\%$ and $\sim 38\%$, respectively.

Following the same procedure, we can also calculate $\varrho_{r,\perp}$; with the knowledge of $\sigma_{r,\perp} = 1.6 \times 10^{-17}$ cm^2 from the previous chapter, we end up with $\varrho_{r,\perp} \approx -9.9 \times 10^{-23}$ cm^3 $\pm 6.8\%$. In this configuration, the contributions to $\eta_{pl.,\perp}$ from the index and absorption gratings are approximately equal.

8.3.4 Intensity dependence of η_{peak} and $\eta_{pl.}$

The dependence of the peak and plateau values of $\eta_{\|}$ on the intensity of the pump pulses are plotted in Fig. 8.6 in logarithmic scales; the attenuation of the pump pulses is achieved with proper neutral-density filters. The data of η_{peak} and $\eta_{pl.}$ are then extracted from the pump-and-probe trace obtained for each pump intensity in the 70-μm $LiNbO_3$ sample.

The dependence of $\eta_{pl.}(I_{p0})$ is fitted with the function $\eta_{pl.}(I_{p0}) = aI_{p0}^{b}$. The extracted optimal exponent b is ~ 2 for the cases $q_p > 10$, which can be justified as follows: when $q_p > 10$, most of the pump energy is absorbed, and the absorbed pulse energy is proportional to the concentration of the excited carriers, which is responsible for the diffraction efficiency at the plateau region. Since the coupling constant κ of the mixed grating is proportional to the carrier concentration, it is natural that the value of $\eta_{pl.}$ depends quadratically upon I_{p0}.

The dependence of $\eta_{peak}(I_{p0})$ is also fitted with the function $\eta_{peak}(I_{p0}) = aI_{p0}^{b}$. However, the distribution of the data points (in squares) suggests a "turning point" of the intensity dependence; the turning point lies somewhere around $\beta_p I_{p0} d = 1$. We therefore fit the data of η_{peak} piecewise: $q_p > 1$ and $q_p < 1$. In the low-intensity region, the fitted exponent b is ~ 2.3, which can be accounted for by a similar reasoning for the $\eta_{pl.}$ dependence. In the high-intensity region, the dependence is almost linear ($b \approx 1.25$), which can be attributed to the inevitable strong absorption experienced by the pump pulses in the sample: less and less portion of the pump-pulse energy is used to establish the mixed grating responsible for η_{peak}.

8.4 Conclusion

Femtosecond time-resolved pump-and-probe experiments are conducted in lithium niobate ($LiNbO_3$) samples with ultrashort pulses. Spatial gratings are established by two interfering intense pump pulses at 388 nm and read out by a Bragg-matched, temporally delayed probe pulse at 776 nm. We claim the first such experiment with sub-picosecond temporal resolution for $LiNbO_3$. Two mixed gratings, one instantaneous and the other permanent, are observed. With the knowledge of the relevant two-photon (quadratic) absorption coefficients of $LiNbO_3$ at both wavelengths, we fit for the Kerr coefficient of $LiNbO_3$ to be $\approx 1.8 \times 10^{-5}$ cm^2/GW.

Bibliography

[1] P. Baldi, M. P. De Micheli, K. El Hadi, S. Nouh, A. C. Cino, P. Aschieri, and D. B. Ostrowsky. Proton exchanged waveguides in $LiNbO_3$ and $LiTaO_3$ for integrated lasers and nonlinear frequency. *Optical Engineering*, 37(4):1193–1202, April 1998.

[2] A. Di Lallo, C. Conti, A. Cino, and G. Assanto. Efficient frequency doubling in reverse proton exchanged lithium niobate waveguides. *IEEE Photonics Technology Letters*, 13(4):323–325, April 2001.

[3] C. Restoin, C. Darraud-Taupiac, J. L. Decossas, J. C. Vareille, J. Hauden, and A. Martinez. Ferroelectric domain inversion by electron beam on $LiNbO_3$ and $Ti : LiNbO_3$. *Journal of Applied Physics*, 88(11):6665–6668, December 2000.

[4] P. Yeh. *Introduction to Photorefractive Nonlinear Optics*. Wiley Interscience, 1993.

[5] R. W. Boyd. *Nonlinear Optics*. Academic Press, New York, 2nd edition, 2003.

[6] P. Günter and J. P. Huignard. *Photorefractive Materials and Their Applications*. Springer-Verlag, Heidelberg, 1989.

[7] L. Eldada. Optical communication components. *Review of Scientific Instruments*, 75(3):575–593, March 2004.

[8] G. A. Rakuljic and V. Leyva. Volume holographic narrow-band optical filter. *Optics Letters*, 18:459–461, March 1993.

[9] S. Breer and K. Buse. Wavelength demultiplexing with volume phase holograms in photorefractive lithium niobate. *Applied Physics B*, 66:339–345, March 1998.

[10] F. Jermann and J. Otten. Light-induced charge transport in $LiNbO_3 : Fe$ at high light intensities. *Journal of Optical Society America B*, 10(11):2085–2092, November 1993.

[11] C. T. Chen, D. M. Kim, and D. von der Linde. Efficient hologram recording in $LiNbO_3 : Fe$ using optical pulses. *Applied Physics Letters*, 34(5):321–324, March 1979.

[12] G. C. Valley, A. L. Smirl, M. B. Klein, K. Bohnert, and T. F. Boggess. Picosecond photorefractive beam coupling in GaAs. *Optics Letters*, 11(10):647–649, October 1986.

[13] A. L. Smirl, G. C. Valley, K. M. Bohnert, and T. F. Boggess. Picosecond photorefractive and free-carrier transient energy transfer in GaAs at 1 μm. *IEEE Journal of Quantum Electronics*, 24(2):289–303, February 1988.

[14] G. C. Valley and A. L. Smirl. Theory of transient energy transfer in Gallium Arsenide. *IEEE Journal of Quantum Electronics*, 24(2):304–310, February 1988.

[15] J. M. C. Jonathan, G. Roosen, and P. Roussignol. Time-resolved buildup of a photorefractive grating induced in BSO by picosecond light pulses. *Optics Letters*, 13(3):224–226, March 1988.

[16] A. L. Smirl, K. M. Bohnert, G. C. Valley, R. A. Mullen, and T. F. Boggess. Formation, decay and erasure of photorefractive gratings written in barium titanate by picosecond pulses. *Journal of Optical Society America B*, 66(4):606–615, April 1989.

[17] I. Biaggio, M. Zgonik, and P. Günter. Photorefractive effects induced by picosecond light pulses in reduced $KNbO_3$. *Journal of Optical Society America B*, 9(8):1480–1487, August 1992.